PACIFIC EARTHQUAKE ENGINEERING RESEARCH CENTER

Centrifuge Modeling of Settlement and Lateral Spreading with Comparisons to Numerical Analyses

Sivapalan Gajan
and
Bruce L. Kutter
University of California, Davis

PEER 2002/10
JANUARY 2003

Centrifuge Modeling of Settlement and Lateral Spreading with Comparisons to Numerical Analyses

Sivapalan Gajan
Graduate Student Researcher

and

Bruce L. Kutter
Professor
Department of Civil and Environmental Engineering
University of California, Davis

PEER Report 2002/10
Pacific Earthquake Engineering Research Center
College of Engineering
University of California, Berkeley

January 2003

ABSTRACT

This report presents the results of six large-scale centrifuge model tests that were performed to study the effects of relative density and thickness of the sand layer on the amount of settlement and lateral spreading of liquefied soils. The models included a "river" channel with clay flood banks underlain by layers of loose and dense sand of variable thickness, and a bridge abutment surcharge on one of the banks. Each model was subjected to three or four significant ground motion events, and the measurements of acceleration, pore water pressure, settlement, and lateral movements are presented. Data from approximately 70 sensors and all shaking events are available via the Internet in well-documented data reports. A Deformation Index (DI), which combines the influences of depth, density, and layer thickness, was found to correlate reasonably well with liquefaction-induced settlements and lateral deformations. It was found that a thick, medium-dense sand layer may present more severe liquefaction consequences than thin, loose layers. Finite element simulations, using SUMDES and OpenSEES, are compared with the experimental results, and the capability of these programs to simulate the results of centrifuge test results are discussed. The increase of soil permeability during liquefaction seems to be an important problem that is not well modeled in analyses, but analytical procedures seem promising overall.

Keywords: Earthquake, liquefaction, sand, clay, OpenSEES, SUMDES

ACKNOWLEDGMENTS

This work was supported in part by the Pacific Earthquake Engineering Research Center through the Earthquake Engineering Research Centers Program of the National Science Foundation under award number EEC 9701568.

The authors would like to acknowledge the suggestions and assistance of Ross Boulanger, Boris Jeremić, Dan Wilson, and technicians Tom Kohnke, Tom Coker, and Chad Justice. The authors would also like to thank several members of the G2 group of PEER researchers (especially Steven Kramer, Raymond Seed, Nicholas Sitar, and Ahmed Elgamal) for helpful suggestions and stimulating discussions of these results. The authors would like to acknowledge Ariyaputhirar Balakrishnan and Kiran Manda, who worked on this project and successfully carried out most of the experiments and the analyses. Valuable comments and suggestions provided by Zhaohui Yang (UCSD) during OpenSEES finite element analysis are gratefully acknowledged. The development of the centrifuge and shaker facilities was supported by the National Science Foundation (NSF), the California Department of Transportation (Caltrans), the Obayashi Corporation, and the University of California, Davis.

CONTENTS

LIST OF FIGURES

LIST OF TABLES

1 Introduction

Earthquake field case histories in the last decade in Kobe, Taiwan, and Turkey demonstrate the devastating effects of soil liquefaction and the associated settlements and lateral spreading, but the detailed documentation of field case histories of soil liquefaction is limited. Centrifuge tests are therefore a useful source of well-documented data to study soil liquefaction problems [Schofield, 1981; Arulanandan and Scott, 1993 and 1994; Dobry et al., 1995; and Kutter, 1995].

Tokimatsu and Seed [1987] produced a chart that allows the liquefaction-induced volumetric strains of saturated sands to be estimated by considering the SPT $(N_1)_{60}$ values and an equivalent CSR of M = 7.5 earthquake. Ishihara and Yoshimine [1992] produced another approach to estimate the volumetric strains caused by liquefaction using a factor of safety against liquefaction and either the maximum cyclic shear strain, relative density, SPT resistance, or CPT resistance.

Bartlett and Youd [1992, 1995] introduced an empirical relationship to estimate the lateral spreading displacements at liquefied sites. These equations were developed from multilinear regression (MLR) of a case history data set. Modified MLR equations were later proposed by Youd et al. [1999] to estimate the lateral displacements for both free-face conditions and ground slope conditions. These equations consider the effect of thickness of the sand layer as the cumulative thickness of saturated granular layers with corrected SPT blow count, $(N_1)_{60}$, less than 15, but do not consider the combined effect of thickness and relative density.

This report presents the results of six large-scale highly instrumented centrifuge model tests along with the results obtained from the finite element analyses. The primary purpose of this test series is to systematically study the effects of relative density and thickness of the liquefying sand layer on the amount of settlement and lateral spreading of liquefied soils. Two tests were conducted to obtain information on the effects of ground motion and slope of the flood plain. Centrifuge experimental results were transformed from model units to prototype units by using the scaling laws applicable to centrifuge modeling. Scaling laws for centrifuge modeling were described in detail by Schofield [1981] and Kutter [1995].

In this report, several experimental results are presented for acceleration, pore water pressure, settlement, and lateral movement. Shear stress-permanent shear displacement loops, calculated from the accelerometer and LVDT readings, are included. Effects of thickness and density of sand layer are combined into a single parameter, Deformation Index, DI, and the dependence of liquefaction-induced settlement and lateral movement on DI are explained by using the experimental results. Permanent volumetric strains are related with the relative density of the sand and the applied base acceleration. Each of these experiments is described in detail in well-documented data reports that include model configurations, applied base motions, and all the sensor recordings. These data reports are available for download at **http://cgm.engr.ucdavis.edu.**

Finite element analyses were carried out using the finite element codes SUMDES (Sites Under Multi Directional Earthquake Shaking) [Li et al., 1992] and multiyield models (OpenSEES) [Yang, 2000] to study the applicability of these numerical procedures to predict the damage caused by liquefaction at a site. Computed results from the above finite element simulation for acceleration, pore water pressure, settlement, and lateral movement are presented and compared with the experimental results.

2 Model Preparation and Testing

2.1 MODEL DETAILS

The models represented a hypothetical bridge site consisting of a river and its flood banks. Nevada Sand and San Francisco Bay Mud were used to construct the models. Models were subjected to different scaled versions of the earthquake acceleration time histories from the 1995 Kobe (Port Island) and 1989 Loma Prieta (Santa Cruz) records. All the models were tested at 30 g on the large centrifuge at UC Davis. Unless otherwise indicated, the model configurations and results are presented using prototype scale units.

Figures 2.1.1 and Table 2.1.1 define the model configurations. The models consisted of a dense sand layer at the bottom, overlain by a loose or a medium-dense sand layer and a sloping clay layer on the top. All models contain a bridge abutment on the north side of the river channel. The channel runs across the model in the east-west direction.

As detailed in Table 1, dense sand (Dr = 80%), medium-dense sand (Dr = 50%), and loose sand (Dr = 30%) were used with thickness varying from 0 to 15.0 m. The whole model was tilted so that the slope of the sand surfaces is 3.0% to 3.3% toward the north. The net slope of the clay at the north flood plain was maintained at about 0%. Except in model U50_4.5S, the clay slope in the south flood plain was 9.0% to 9.3%. The thickness of the clay layer was about 1.2 m near the river channel in all models. The height of the water table above the top of the sand layer was maintained at about 1.2 m in all the models except U30_4.5M. In U30_4.5M, the water table fluctuated from – 0.3 m to 1.3 m. Figure 2.1.2 shows the dimensions of the model in test U30_4.5M in detail. It should be noted that except for the soil layer thickness and slopes, all other dimensions, i.e., dimensions of the bridge abutment and the river channel, were the same in all tests.

Models were constructed in two types of flexible shear beam containers FSB1 (1.72 m long x 0.69 m wide x 0.70 m deep) and FSB2 (1.65 m long x 0.78 m wide x 0.59

m deep). These model containers consist of a stack of rectangular aluminum tubes and rubber (see Fig 2.1.1). The rubber, being flexible in shear, allows the container to deform dynamically with the soil layer. Models C80, U50 and U50_4.5 were constructed in FSB1, whereas models U50_4.5S, U30_4.5 and U30_4.5M were constructed in FSB2. The dynamic performance of flexible shear beam containers is documented by Wilson et al. [1997].

The preparation procedures were similar for all models. Sand was pluviated at required densities using air pluviation. Nevada Sand (uniformly graded fine clean sand with D_{50} = 0.17 mm, C_u = 1.6, e_{max} = 0.881 and e_{min} = 0.536) was used for all sand layers in all models. The soil properties of Nevada Sand are given by Arulmoli et al. [1991] and Chen [1995]. The remolded San Francisco Bay Mud (LL = 90, PL = 38) was placed on top of the sand layer and consolidated under about 80 kPa consolidation pressure at 1 g. After consolidation, the clay surface was carved to make the required slopes, and the river channel was constructed. Then the bridge abutment, which is made up of red stiff clay, was placed on the northern flood plain. To study the effect of the slope of clay, the model U50_4.5S was prepared with a different clay slope than U50_4.5. To study the effect of ground motion characteristics, model U30_4.5M was prepared with the same configuration as U30_4.5 (except for an inadvertent water table change of about 1.0 m). These two pairs of model tests were also intended to study the repeatability of centrifuge tests. More details of these models and all experimental data are documented in data reports available for download at **http://cgm.engr.ucdavis.edu.**

2.2 TESTING PROCEDURE

About 70 sensors were placed in each model: LVDTs, accelerometers and pore water pressure transducers. Figure 2.2.1 shows sensor locations for U30_4.5M. An attempt was made to locate sensors in similar locations in each test. Thus the sensor location numbers in Figure 2.2.1 are, within reasonable accuracy, applicable to all tests reported herein. It should be noted that the sensors were placed in similar locations relative to the model container, while the soil geometry varied. For example, sensor P3 was placed in dense sand (Dr = 80%) in model U30_4.5M (Fig. 2.2.1), whereas it was placed in medium-dense sand (Dr = 50%) in model U50., since U50 consisted of a 9.0 m medium-dense sand layer on top compared to a 4.5 m loose sand layer on top in model U30_4.5M. Precise sensor locations for all models can be found in the data reports.

After preparation, the models were placed in the large geotechnical centrifuge at UC Davis and spun at 30 g centrifugal acceleration. Detailed specifications and facilities of this centrifuge are described by Kutter et al. [1994]. Table 2.2.1 shows the date, time, and sequence of shaking events along with the peak base accelerations in each model test. The Kobe and Santa Cruz motions were used with different amplification factors in order to produce different peak accelerations at the base. As shown in Table 2.2.1, all the models except U30_4.5M were subjected to the following sequence: a small step wave, a small Kobe ($a_{base,\ max} \cong 0.12$ g) wave motion, a large Kobe ($a_{base,\ max} \cong 0.80$ g) wave motion, an intermediate Kobe ($a_{base,\ max} \cong 0.28$ g) wave motion, and small step wave events. U30_4.5M events included two large Santa Cruz events ($a_{base,\ max} \cong 1.0$ g) and an intermediate Santa Cruz event ($a_{base,\ max} \cong 0.21$ g) in place of the large Kobe and intermediate Kobe events. The small step waves produced a couple of small high-frequency pulses of motion to confirm that the sensors were functioning properly; the small step events did not cause significant deformations. Figures 2.2.2 and 2.2.3, respectively, show the applied base motion time histories of the Kobe and Santa Cruz motions along with the small step waves.

Spectral accelerations are plotted against period for all five models that were subjected to the Kobe motions in Figure 2.2.4. For the small and intermediate Kobe events, the spectral accelerations show considerable variations in period, from 0.15 to 0.5 sec. Since settlements and lateral movements were dominantly controlled by the large events, spectral displacements were computed and compared for all the models. Figure 2.2.5 shows the acceleration and displacement response spectra of all six large events together used in the tests. As can be seen from the figure, the spectral accelerations of all five large Kobe events look very similar in all periods except periods from 0.09 to 0.12 sec. The large Santa Cruz motion (U30_4.5M) exceeds the Kobe motion for periods of less than 0.15 sec and is smaller for periods greater than 0.15 sec. Spectral displacement are very similar for all Kobe events indicating the repeatability of the shaking equipment. Kobe motions show a peak displacement at a period of 2.0 sec whereas the Santa Cruz motion shows peaks at 1.4 sec and 3.0 sec periods.

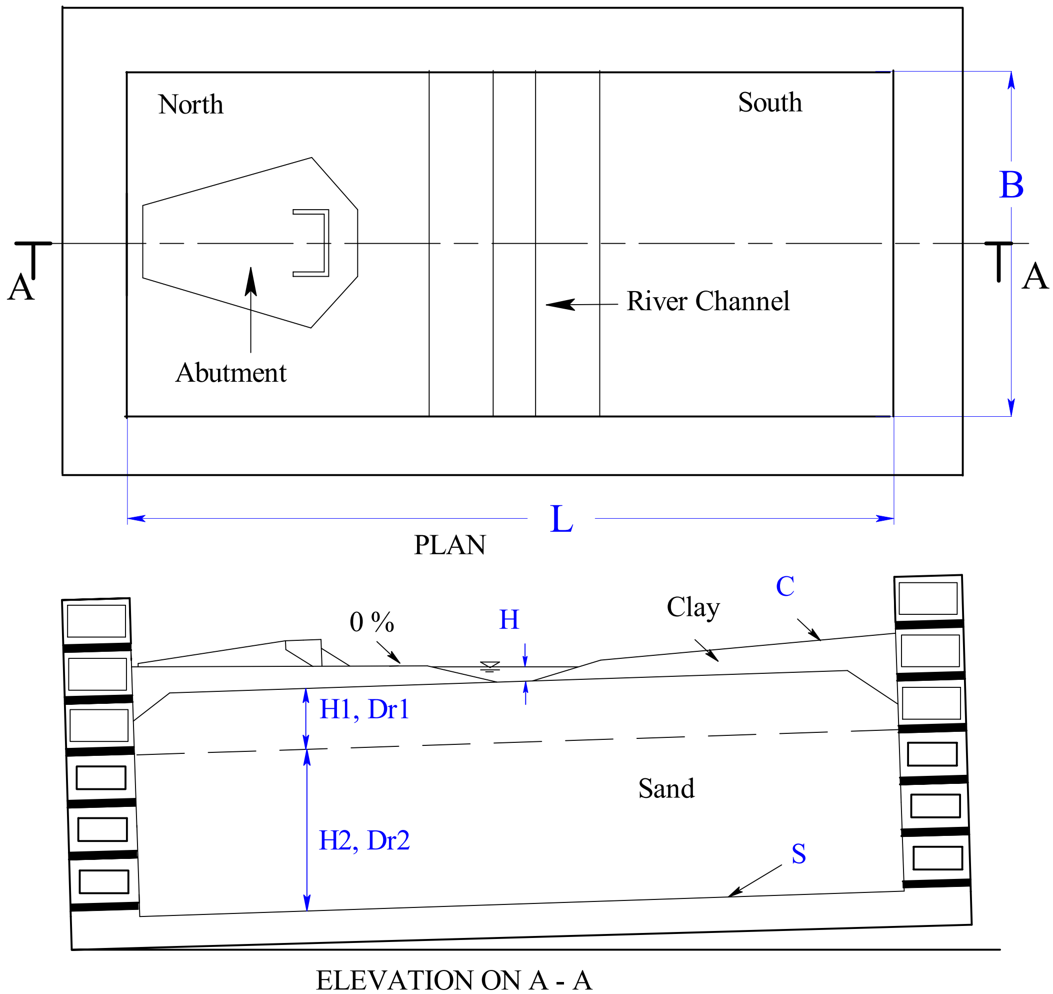

Fig. 2.1.1 General model configuration details

Table 2.1.1. Model details

Model code	Model details	Slope of clay (C)	Slope of sand (S)	Height of W.T. (H)	L and B
C80	H1 = 0m Dr2 = 80%, H2 = 15	9.3%	3.3%	1.2m	L = 1.72 m B = 0.68 m
U50	Dr1 = 50%, H1 = 9m Dr2 = 80%, H2 = 6m	9.0%	3.0%	1.2m	L = 1.72 m B = 0.68 m
U50_4.5	Dr1 = 50%, H1 = 4.5m Dr2 = 80%, H2 = 10.5m	9.3%	3.3%	1.2m	L = 1.72 m B = 0.68 m
U50_4.5S	Dr1 = 50%, H1 = 4.5m Dr2 = 80%, H2 = 7.5m	3.0%	3.0%	1.2m	L = 1.65 m B = 0.78 m
U30_4.5	Dr1 = 30%, H1 = 4.5m Dr2 = 80%, H2 = 7.5m	9.3%	3.3%	1.2m	L = 1.65 m B = 0.78 m
U30_4.5M	Dr1 = 30%, H1 = 4.5m Dr2 = 80%, H2 = 7.5m	9.3%	3.3%	-0.3~1.3m (Variable)	L = 1.65 m B = 0.78 m

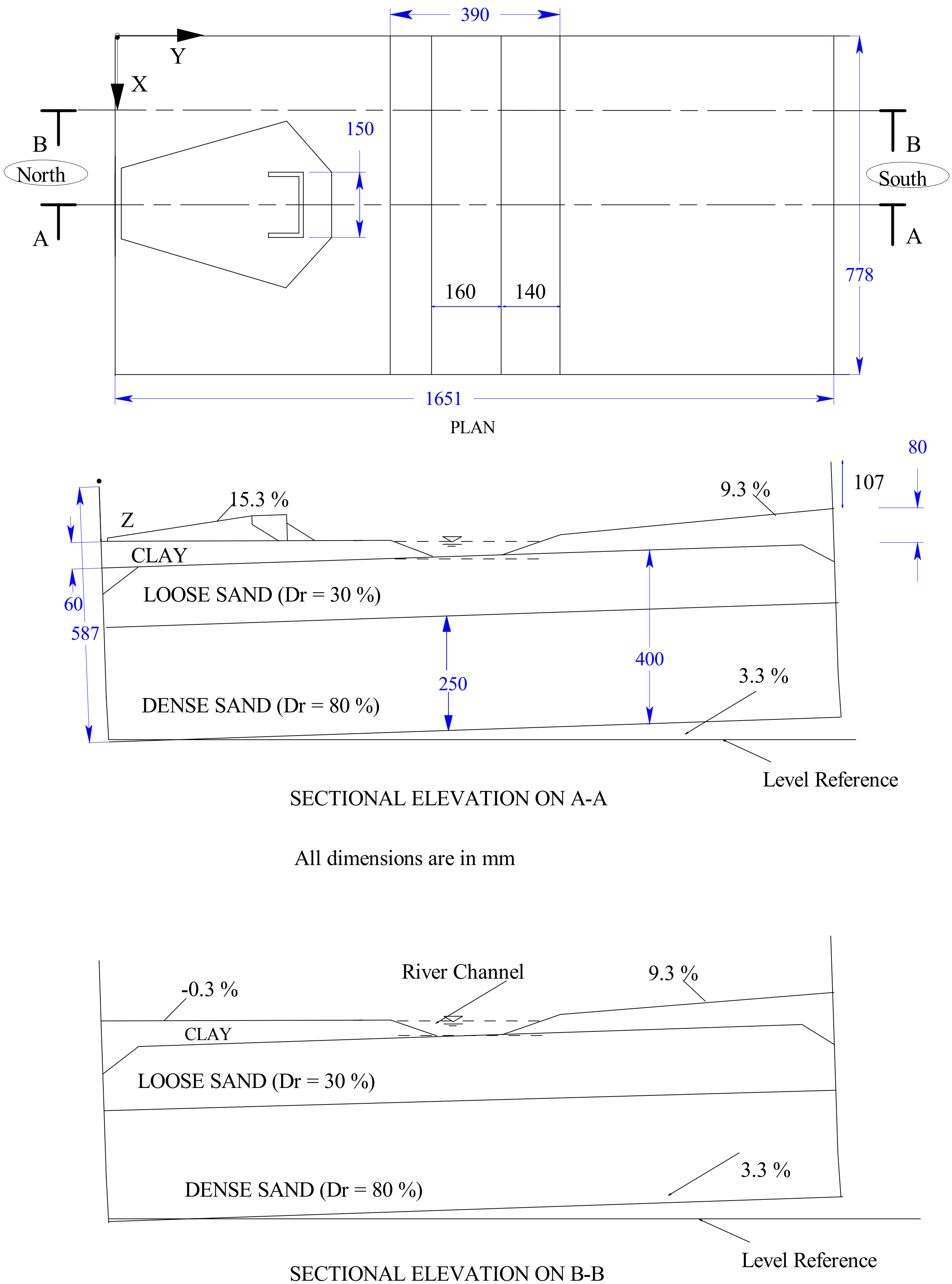

Fig. 2.1.2 Model dimensions for U30_4.5M

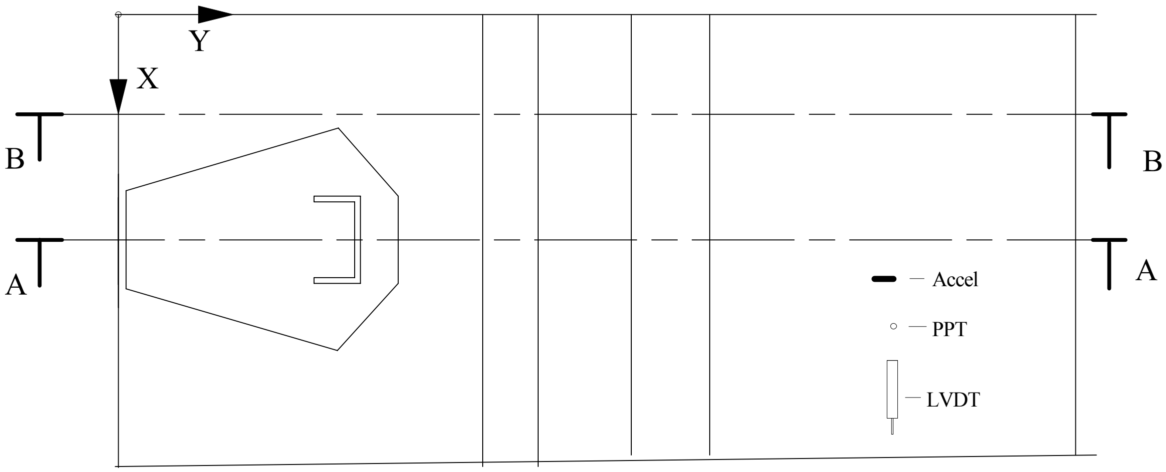

PLAN

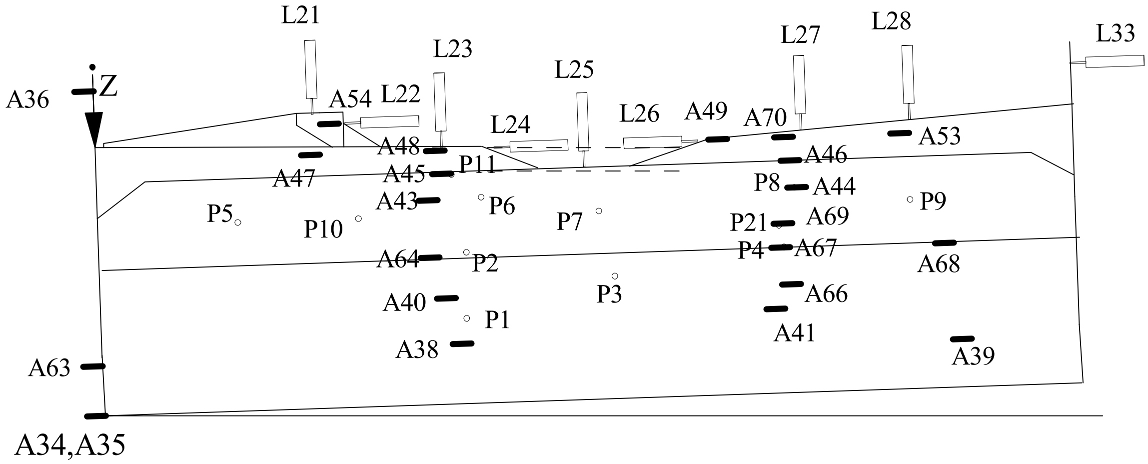

SECTIONAL ELEVATION ON A-A

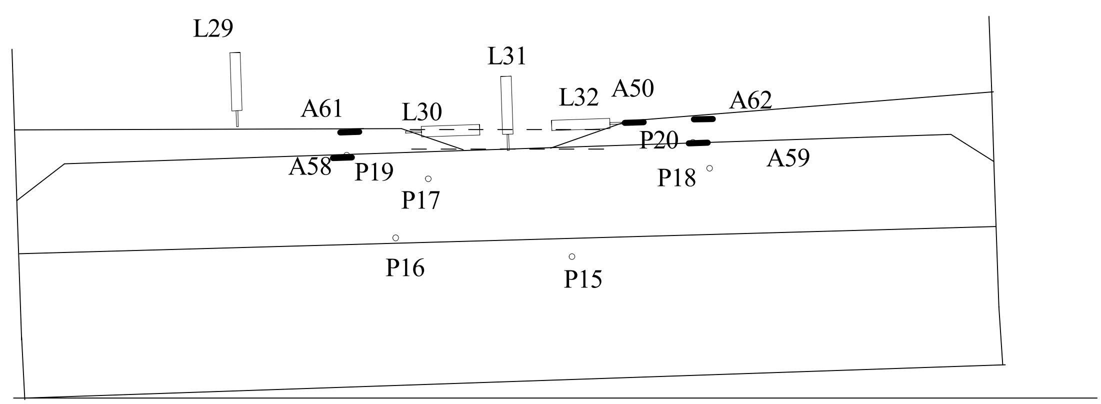

SECTIONAL ELEVATION ON B-B

Fig. 2.2.1 Instrument locations in model U30_4.5M

Table 2.2.1 Sequence of shaking events

Date and time	Event identification	Event name	Peak base acc. (g)
March 21, 1997			
14:34	U50_02	Small Step	0.15
15:05	U50_03	Small Kobe	0.13
15:43	U50_04	Large Kobe	0.73
16:17	U50_05	Intermediate Kobe	0.29
16:40	U50_06	Small Step	0.13
June 15, 1998			
14:58	C80_01	Small Step	0.09
15:36	C80_02	Small Kobe	0.12
16:16	C80_03	Large Kobe	0.73
17:00	C80_04	Intermediate Kobe	0.27
17:28	C80_05	Small Step	0.09
March 19, 1999			
17:55	U50_4.5_01	Small Step	0.04
18:17	U50_4.5_02	Small Kobe	0.12
18:46	U50_4.5_03	Large Kobe	0.80
19:32	U50_4.5_04	Intermediate Kobe	0.32
19:45	U50_4.5_05	Small Step	0.02
Sept. 24,1999			
17:45	U30_4.5_01	Small Step	0.06
18:48	U30_4.5_02	Small Kobe	0.11
19:16	U30_4.5_03	Large Kobe	0.83
19:32	U30_4.5_04	Intermediate Kobe	0.27
20:05	U30_4.5_05	Small Step	0.05
March 2, 2000			
14:50	U50_4.5S_01	Small Step	0.03
15:20	U50_4.5S_01	Small Kobe	0.11
15:50	U50_4.5S_01	Large Kobe	0.83
16:29	U50_4.5S_01	Intermediate Kobe	0.30
16:55	U50_4.5S_01	Small Step	0.03
Jan. 24, 2001			
18:51	U30_4.5M_01	Small Step	0.04
19:18	U30_4.5M_02	Small Kobe	0.11
20:14	U30_4.5M_03	Large Santa Cruz (1)	1.10
20:55	U30_4.5M_04	Intermediate Santa Cruz	0.21
Jan. 25, 2001			
16:20	U30_4.5M_05	Large Santa Cruz (2)	0.93
16:45	U30_4.5M_06	Small Step	0.03

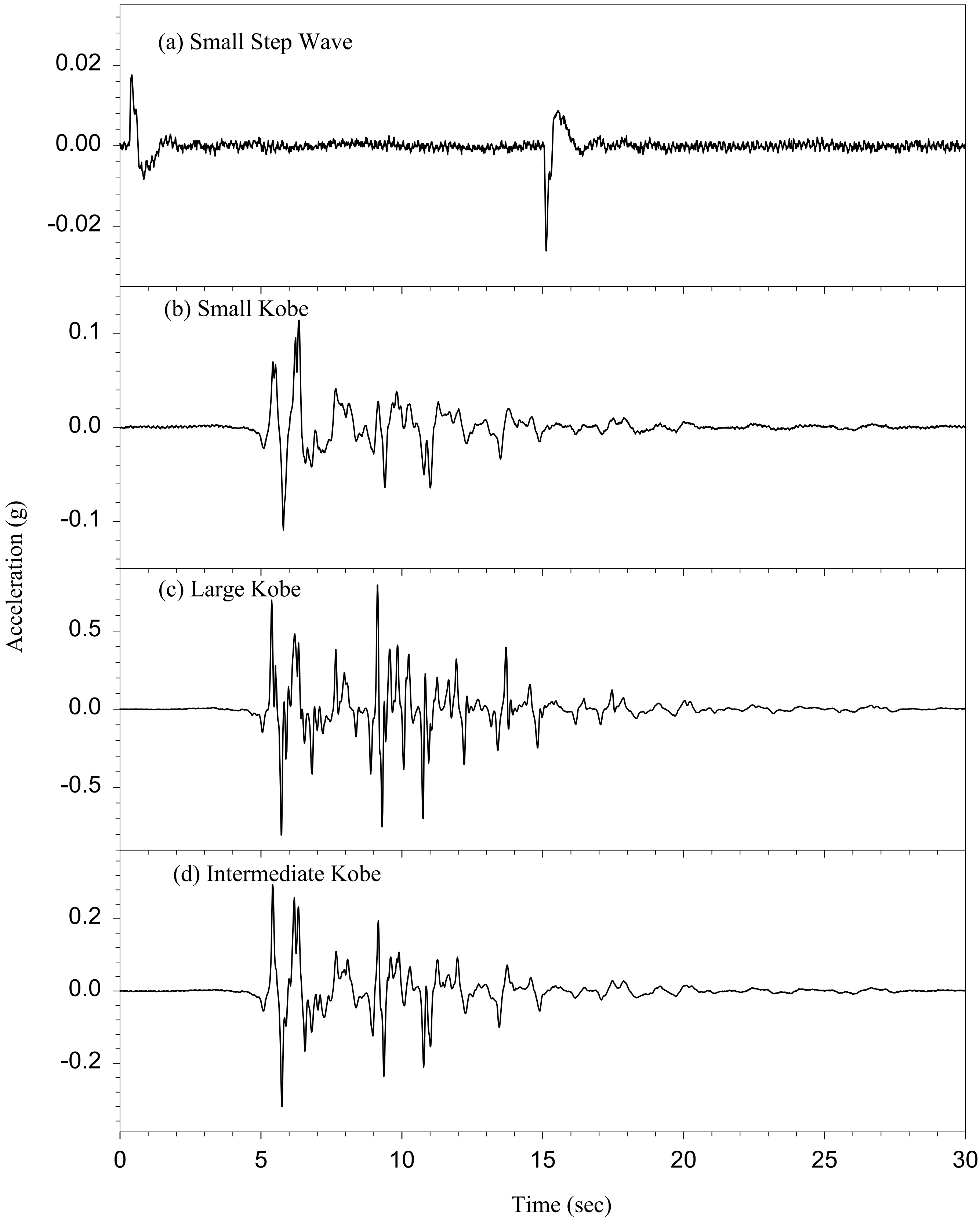

Fig. 2.2.2 Average base acceleration time histories in U50_4.5

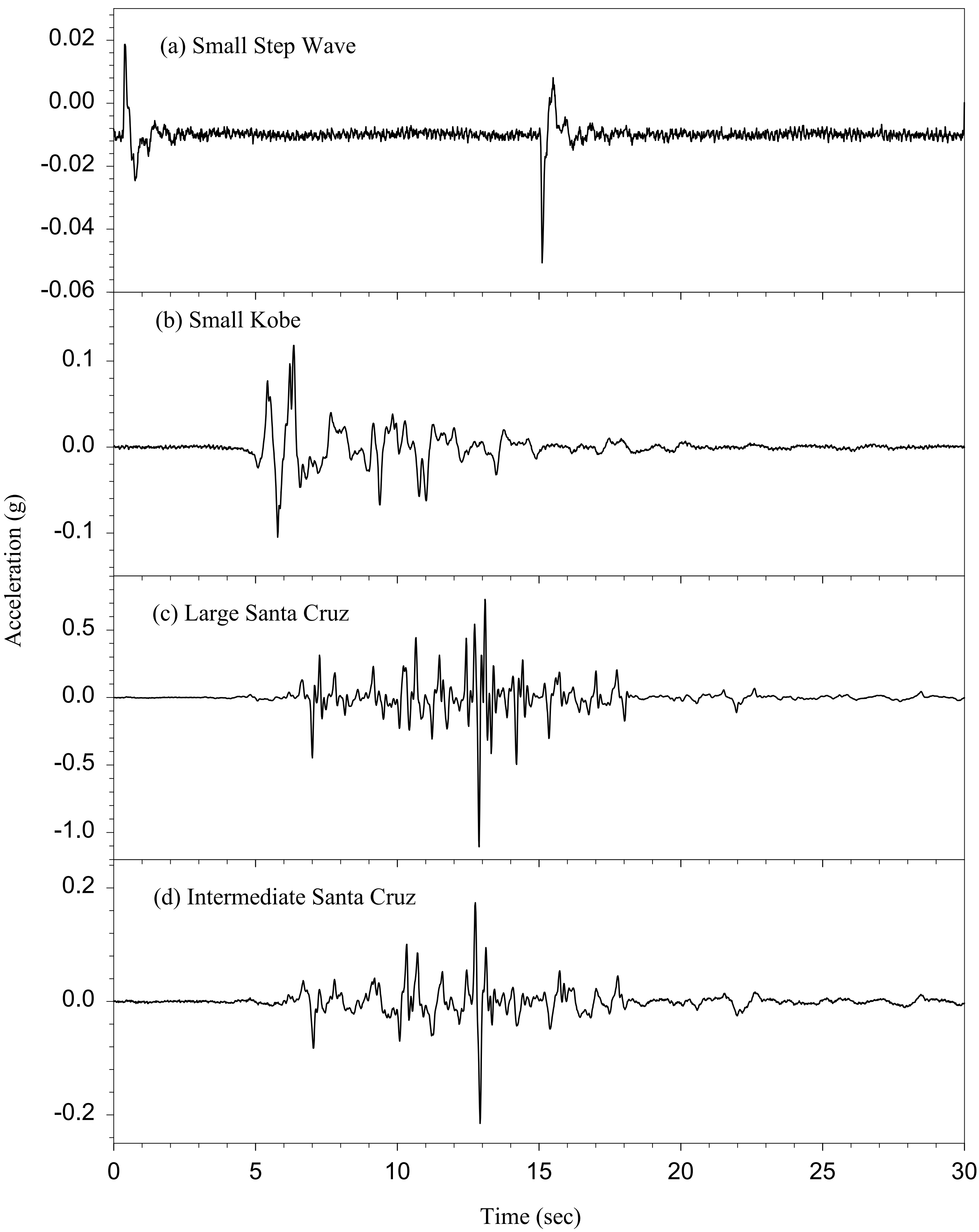

Fig. 2.2.3 Average base acceleration time histories in U30_4.5M

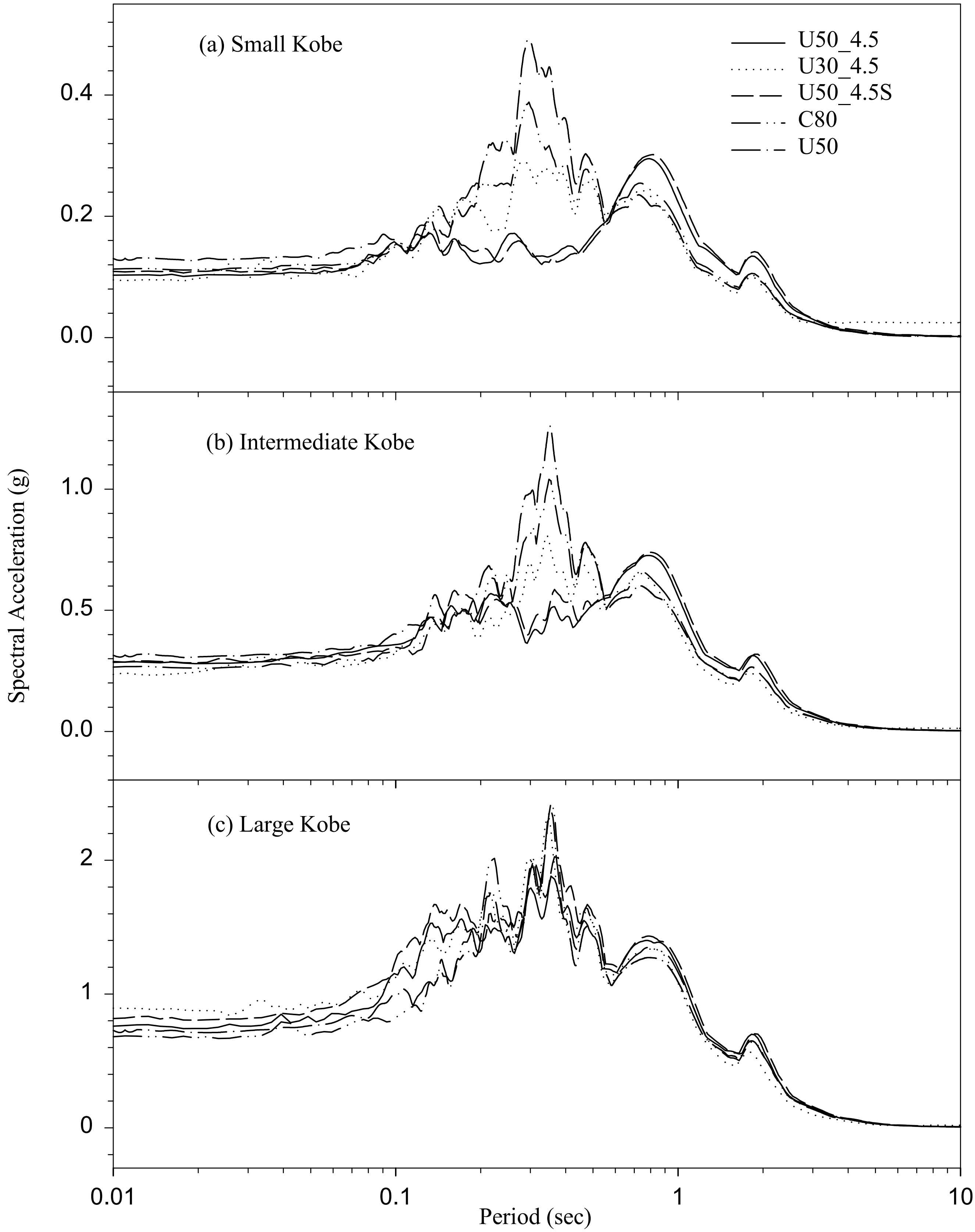

Fig. 2.2.4 Average base acceleration response spectra during (a) small Kobe, (b) intermediate Kobe, and (c) large Kobe events

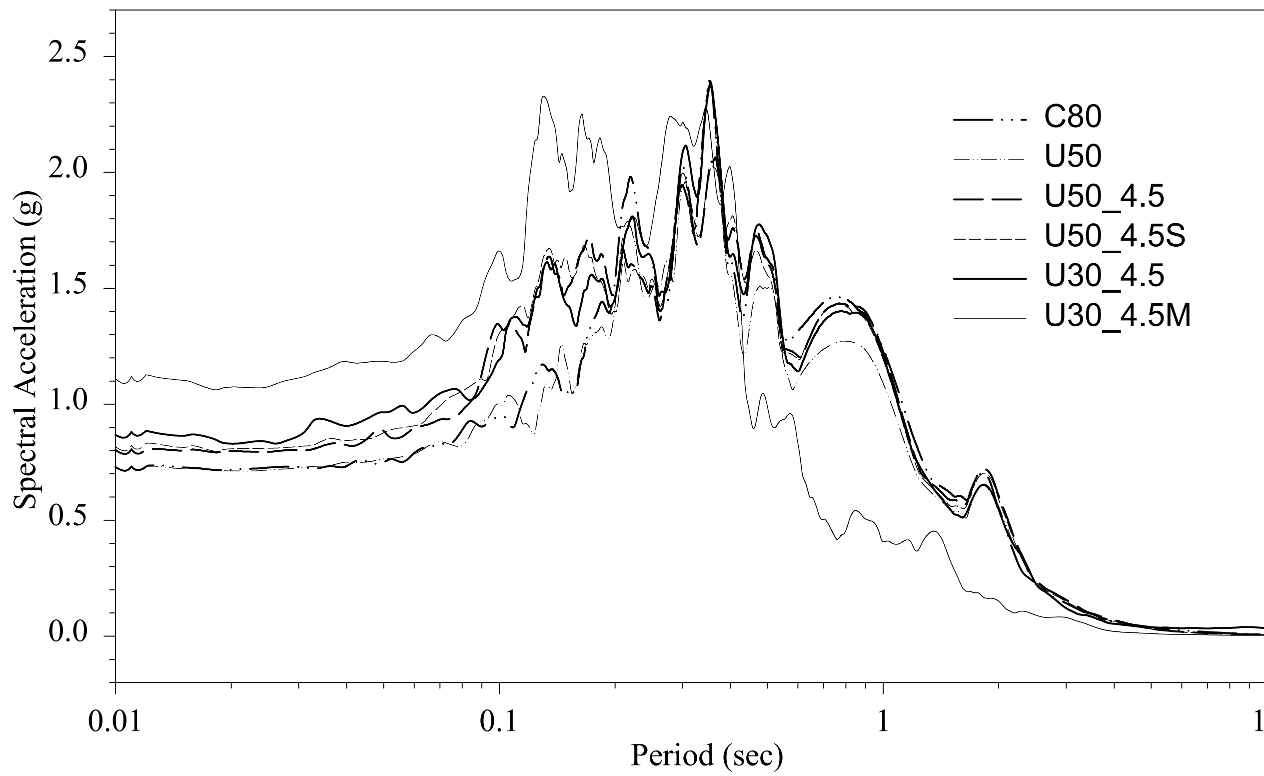

(a)

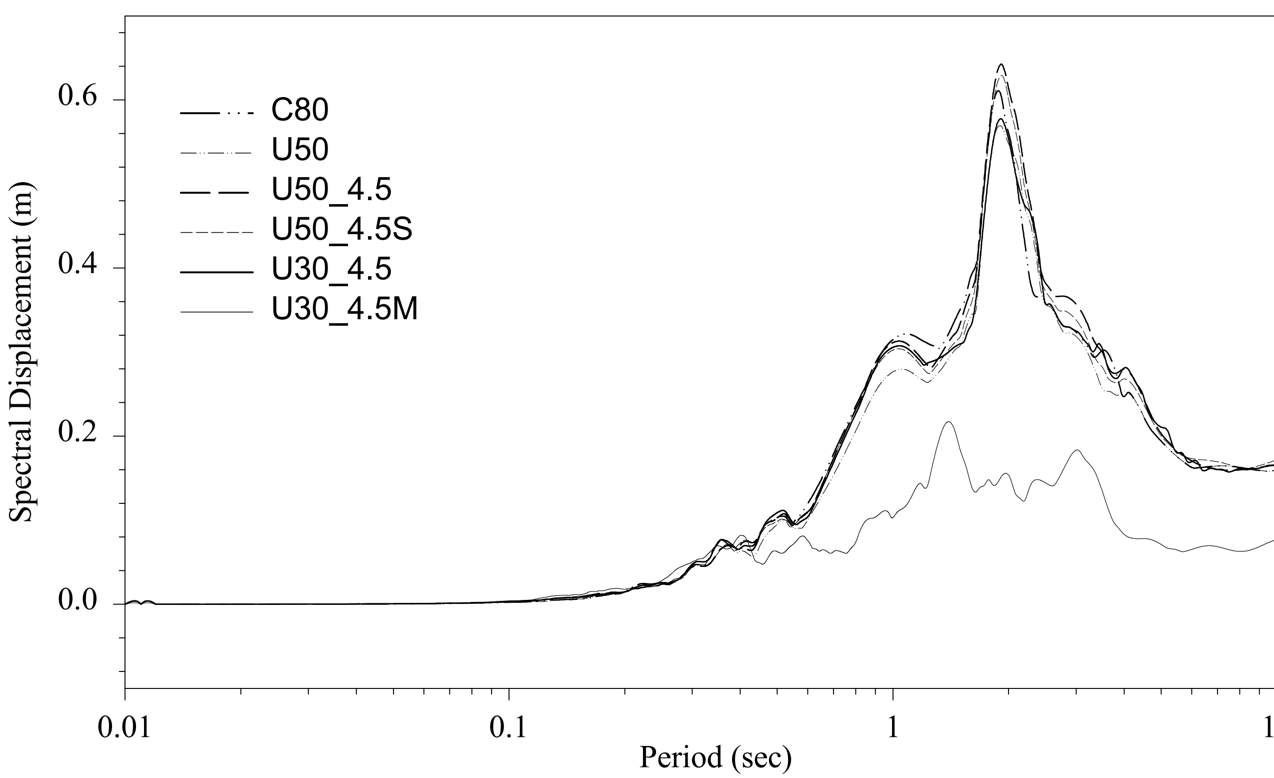

(b)

Fig. 2.2.5 (a) Spectral accelerations and (b) spectral displacements of large events

3 Experimental Results

Figure 3.0.1 shows the excess pore water pressures at a depth of 3.6 m in medium-density sand at the south central portion (P21), the lateral movement of the south riverbank relative to base (L26-L33), and the settlement of the abutment (L21), along with the applied base acceleration time histories for the sequence of significant events in test U50_4.5. Sufficient time for pore water pressure dissipation was allowed between events; Figure 3.0.1 illustrates the strong motion time window for each significant event spliced together. This shows how the magnitude and duration of the base motion influence the generation of excess pore water pressures, lateral movements, and settlements. The pore pressure records indicate zero effective stress for the large and intermediate events, but that dissipation occurs much sooner for the intermediate Kobe event.

Very little settlement and lateral deformation occurred after shaking ceased. About 80% of the total settlement and about 90% of the total lateral movement occurred due to the large Kobe event. This event also caused the sand to densify, which certainly affected the behavior during the subsequent intermediate Kobe event. This is the common trend observed in all the models. Figures 3.0.2 and 3.0.3 show similar plots for tests U50 and U30_4.5M, respectively.

3.1 ACCELERATIONS

The negative spikes in pore pressure associated with the dilative behavior of sand were observed only in large and intermediate events. Figures 3.1.1 and 3.1.2 show the negative spikes in pore pressures and the associated acceleration spikes (from the nearby accelerometers) for model tests U50, U50_4.5, U30_4.5 and U30_4.5M. Kutter and Wilson [1999] termed the phenomenon of temporary solidification of liquefied soil due to negative pore pressure spikes "deliquefaction" and showed that the negative pore pressure spikes are associated with acceleration spikes that may travel as shock waves. The relationship between dilatancy, negative pore pressure spikes and acceleration spikes has also been described by Fiegel and Kutter [1994], Dobry et al. [1995], Elgamal et al. [1996], Taboada and Dobry [1998], and Balakrishnan and Kutter [1999].

Records of accelerometers A46 and A44 along with the applied base acceleration time histories for large events are shown in Figure 3.1.3. As shown in Figure 2.2.1, accelerometer A46 was located at the interface of sand and clay and A44 was placed in the upper portion of the top sand layer in the south array. It should be noted that for model U50_4.5, accelerometers A46 and A44 were not functioning properly and therefore the accelerations from A59 and A57, which were placed at the same elevation as A46 and A44, respectively, but were located about 5 m west of the N-S centerline, are shown for test U50_4.5. In test U50_4.5S (Fig. 3.1.3.d), the accelerometer records show step offsets at t ~ 6.5 and t ~ 11.5 sec. The steps are due to an electronic response to a high-frequency spike of acceleration. The steps do not represent steps of soil acceleration. Model U30_4.5M was subjected to the large Santa Cruz motion where as all other models were subjected to the large Kobe motion. The absence of deliquefaction acceleration spikes in U30_4.5M suggests that the spikes may be associated with the large displacement ground motions and large strains mobilized. The coincidence of approximately 2.0 s spacing of acceleration spikes in Figures 3.1.3.a–e and 2.0 s peaks in the Kobe motion displacement spectrum (Fig. 2.2.5.b) reinforces the correlation between displacement peaks and acceleration peaks.

The results of C80, U50_4.5, and U30_4.5 in Figure 3.1.3 clearly show the effects of the density of the upper sand layer on the accelerations of sand. These models contain 4.5 m thick top sand layers of relative densities of 80%, 50%, and 30%, respectively. The number and magnitude of acceleration spikes increase as the sand density increases. The effect of the thickness of the top medium-density sand layer (Dr = 50%) on the acceleration of sand can be observed by comparing the results of C80, U50_4.5 and U50. They contain 50% relative density sand layer of thickness 0, 4.5, and 9.0 m, respectively. The number and the magnitude of acceleration spikes increase as the thickness of the top medium-density sand layer decreases. In general, as the degree of improvement (combined effect of density and thickness) increases, the soil stiffness increases and more spikes are transmitted to the top of the sand layer. Balakrishnan and Kutter [1999] observed a similar trend.

Though the models U30_4.5 and U30_4.5M have the same configuration except for the depth of the water table, they show significant differences in the magnitudes of accelerations at the top of the loose sand layer (Dr = 30%). Pore water pressure recordings show that both of these models liquefied. Acceleration spikes were transmitted to the top of the loose sand layer despite liquefaction in U30_4.5, while it was not the case in U30_4.5M. The top of the sand of U30_4.5M seems to be isolated from the base soil because of liquefaction and hence no significant accelerations spikes were transmitted to the top of the loose sand layer. The Santa Cruz motion has higher frequency content and smaller displacements and the Kobe motions have a peak displacement component at a period of 2.0 sec (Fig. 2.2.5.b). The small displacements of the Santa Cruz motion and the small mobilized strains of soil were, apparently, too small to trigger the deliquefaction.

It can be seen from Figure 3.1.3 that the models C80, U50_4.5, and U50_4.5S show acceleration spikes in both directions. In contrast, the other three models show predominantly negative acceleration spikes at the top of the loose sand layer. Note that positive acceleration is toward the north direction (downslope). The spikes are associated with dilatancy, which tends to occur at large shear strains. For sloping ground, the strains accumulate in the north direction; hence dilation is more prevalent for southward acceleration spikes (these occur at maximum northward displacement).

Figures 3.1.4 and 3.1.5 show the acceleration time histories and the corresponding dynamic displacements at different depths in tests U30_4.5 and U30_4.5M, respectively. The dynamic displacements, calculated by high-pass filtering (f_c = 0.15 Hz) and double integration of the accelerations, show a general trend of amplification and phase delay with elevation. This compares well with the findings of Balakrishnan and Kutter [1999]. Also, the dynamic displacements are consistently smaller in U30_4.5M than in U30_4.5. This can also be explained by the nature of the different base motions.

Figure 3.1.6 shows the accelerations in a south array of model U30_4.5M for the large Santa Cruz event. In Figure 3.1.6, the vertical spacing between traces is proportional to the physical spacing between the sensors; an elevation scale is indicated on the right side of the figure. Figure 3.1.6 clearly shows the time shift of acceleration spikes and provides data to enable estimation of shear wave velocities in the soil. The velocity of the large spike between A41 and A67 in the dense sand is about 50 m/sec, while in the loose sand, between A67 and A69, the velocity is about 12 m/sec. Above A69, the large spike dies in liquefied sand. Computed velocities at selected points are labeled in Figure 3.1.6. Low-wave velocities indicate that the sand loses its stiffness due to liquefaction. From Figure3.1.6, it is apparent that the wave velocity depends on the pore pressure, amplitude of oscillation, and time in a nonlinear fashion. Also note that the large spike traveling at 12 m/sec at about 13.5 sec is considered to be a shear shock wave, which may travel at a different speed than shear waves [Kutter and Wilson, 1999].

3.2 PORE WATER PRESSURES

Pore pressure transducers P11, P6, P2, and P1 were placed in a vertical array in the central northern portion of all the models (Fig. 2.2.1). Figure 3.2.1 compares the pore pressure ratios obtained during large Kobe events for different densities of the top 4.5 m of sand. In general, pore pressure ratios increase and the dissipation rates decrease as the density of the soil layer decreases. Since the dilative behavior of sand increases as density increases, model C80 shows more and broader negative spikes in pore water pressure than the other two models. In Figure 3.2.2, the models consist of a Dr = 80% layer overlain with a Dr = 50% layer of thickness H1 = 0, 4.5, and 9.0 m. It can be seen that the pore pressure ratios increase as the thickness of the Dr = 50 % layer increases. For larger H1, the pore pressure ratios remain high longer and dissipate slower than the other two models.

Figure 3.2.3 shows the effect of ground motion and the ground water table on pore pressure ratios. The models appeared to reach 100% pore pressure ratio, but the pore pressures developed a bit faster for the Kobe motion than for the Santa Cruz motion, indicating that the Kobe motion is more damaging. The long-term pore pressure ratios are greater for the Santa Cruz motion (U40_4.5M) than the Kobe motion (U30_4.5). This is because the ground water table in U30_4.5M was started about 1.0 m lower than the water table in U30_4.5. The difference in residual pore pressure ratio in Figure 3.2.3 is due to the change of water table depth during this event in test U30_4.5M.

3.3 DEFORMATIONS

Figures 3.3.1 and 3.3.2 show the deformed shapes of colored soil layers and columns in the middle section (section A–A) and the east section (section B–B), respectively, of the models before and after testing. The locations of the colored sand layers and columns were obtained by dissecting the models. Owing to the abutment overburden, settlements in the northern side are larger than in the southern side. Lateral movements are larger in the southern side than the northern side because of the overall slope from south to north. Unexpectedly, the lateral movements of the clay layer in the southern flood plain are almost the same in all the models except U50_4.5S, the model with a clay slope different than the others. No noticeable deformations occurred in the bottom 6.0 m of the dense sand layer (Dr = 80 %) in any of the models (about 30 mm prototype, 1 mm model would have been noticeable).

The deformed shapes of the models C80, U50_4.5, and U50 show the effect of the thickness of the top sand layer on the deformations of sand. Settlements and lateral movements are larger in U50, which contains 9 m of 50% relative density sand, and smaller in C80, which does not contain a 50% relative density top sand layer. Similarly, models C80, U50_4.5 and U30_4.5 show the influence of the relative density of the top 4.5 m sand layer on the deformations of sand. Comparison of models U50_4.5 and U50_4.5S shows the effect of the clay layer slope on the amount of lateral movement of clay. It is interesting to note that the lateral movement of the clay did not seem to depend on the density or depth of the underlying sand; the lateral movement was always about 1.5 to 1.8 m if the clay surface slope was 9%. This unexpected result was also observed by Balakrishnan and Kutter [1999]. Owing to the relatively low permeability of the clay, high pore water pressures always developed at the interface of the sand and clay in all tests, including the test with 80% relative density sand. The similarity in lateral clay displacements in a variety of tests may be due to several factors: (1) the clay displacement was controlled by the high interface pore pressures, (2) the width of the river channel tended to prevent lateral displacements from exceeding about 2 m, and/or (3) the looser sand layers tended to isolate the clay from the strong ground motions. In U50_4.5S, the net clay layer slope was reduced to 3.0% (about 9.0% in other tests), and the lateral spreading was reduced by a factor of two to three. Yang and Elgamal investigated the influence of permeability on the amount of lateral movement immediately below a low permeable layer in sloping grounds [Yang and Elgamal, 2002]. Their numerical simulations showed that the formation of a thin water layer below the low permeable layer reduces the available shear strength, which in turn results in significant lateral deformation.

The effect of ground motions on deformation mechanisms can be seen from the deformed shapes of U30_4.5 and U30_4.5M (Figs. 3.3.1 and 3.3.2). These two models have the same model configurations except that U30_4.5M had a lower initial ground water table. U30_4.5 was subjected to one large Kobe event, whereas U30_4.5M was subjected to two large Santa Cruz events. The average settlements are larger in U30_4.5M than in U30_4.5, nevertheless the measured lateral movements of the sand are smaller in U30_4.5M than in U30_4.5. In terms of lateral movements of the sand, the 0.8 g Kobe event appears to be more damaging than the 1.1 g Santa Cruz event. However, the two Santa Cruz events appear to have caused more settlement of the abutment than the Kobe event.

Figure 3.3.3.a shows the variation of cumulative settlement (all five or six events) of sand beneath the abutment as a function of depth for a station directly beneath the abutment on the north floodplain. This data was obtained by measuring the final elevation of the clay sand interface and black sand layers initially placed at depths of 4.5 m and 9.0 m below the sand surface. Settlements of U50_4.5 and U50_4.5S are very similar; this indicates that changing the slope of the clay surface in the southern floodplain did not make much difference in the settlement beneath the abutment. The models U30_4.5 and U30_4.5M also show the similar trend despite their different applied base motions. It should be noted that U30_4.5M was subjected to two large Santa Cruz events, whereas U30_4.5 was subjected to one large Kobe event. Owing to seismic history and densification, the second large Santa Cruz motion caused about half the settlement that the first large Santa Cruz event caused. Except for C80 and U50, the other four models clearly show the change in slope in settlement plots at 4.5 m depth, which occurs because of the change in density of sand at that depth. Final settlements at the top of the sand layer decrease from about 0.93 m to 0.45 m to 0.32 m as the relative density of the top 4.5 m

thick sand layer increases from 30% to 50% to 80%. Similarly, by comparing the settlements of U50 and U50_4.5, one can see the effect of thickness of the top 50% relative density sand. The settlements are almost doubled when the thickness of the 50% relative density sand is doubled.

Lateral displacements of sand at the south central portion of the models are plotted against the depth in sand from the top of the sand surface in Figure 3.3.3.b. As observed in settlement plots (Fig. 3.3.2.a), the pairs (U50_4.5 and U50_4.5S) and (U30_4.5 and U30_4.5M) show very similar results for lateral movements. The lateral movements of U30_4.5M are smaller than those of U30_4.5 although U30_4.5M was subjected to two large Santa Cruz events. The change in slope of lateral movements at 4.5 m depth in the U30_4.5 pair models is larger than that in the U50_4.5 pair models because the relative density of sand changes from 80% to 30% in the first pair, whereas it changes from 80% to 50% in the latter pair. The model U50 gives larger lateral movements compared to U50_4.5 or U50_4.5S because of the effect of thickness of the top 50% relative density sand.

3.4 COMBINED EFFECT OF THICKNESS, DENSITY, AND DEPTH

The observations above suggest that settlements and lateral movements of a point tend to increase as the thickness of the underlying layer increases and to decrease with relative density of the underlying sand. An attempt was made to combine the effects of thickness, density and depth in one "Deformation Index," (DI), to compare the results of all tests in one plot:

$$\mathrm{DI}\ (z) = \int_{z}^{\mathrm{rigidbase}} (1-\mathrm{Dr})^2\, dz \quad \text{or in summation form, } \mathrm{DI}\ (z) = \sum_{z}^{\mathrm{rigidbase}} \mathrm{H_i}\,(1-\mathrm{Dr_i})^2 \qquad \text{(Eq. 3.1)}$$

where z is the depth of the point considered, measured from the top of the sand layers, and H and Dr are the thickness and the density of the sand, respectively, below the point of interest. The exponent of 2 was obtained by trial and error and by qualitative consideration that the total possible strain is approximately proportional to (1 – Dr) (Eq.

3.2), and the likelihood of liquefaction increases with (1 – Dr). For example, at the midpoint of the Dr = 30% layer in U30_4.5,

$$DI\ (2.25\ m) = 2.25\ m\ (1.0\text{-}0.3)^2 + 7.5\ m\ (1.0\text{-}0.8)^2 = 1.40\ m$$

The relation between the DI and the average settlement of sand is shown in Figure 3.4.1.a. The average settlements were taken from the final surface elevation measurements after all shaking events had been completed and then distributed to each individual event according to the percentage of settlements observed in each event from the vertical LVDT readings (L23 and L27). The values of the peak base acceleration of each individual event applied to each model are also shown near the data points. Peak base acceleration contours were estimated to assist in evaluation of the correlation. It should be noted that for intermediate events, the relative density of the sand layer was corrected to account for the change in density during previous large events as described by Manda [2000]. Figure 3.4.1.b shows the variation of lateral movement of sand in the south central portion with the DI after all shaking events. These lateral movements were obtained by measuring the final position of the black sand columns after tests and hence this is the total movement that occurred during all shaking events in each model. The data plotted show a clear trend of increase in lateral movement as the DI increases. The DI was calculated at various depths and plotted against the corresponding lateral movements at that depth to produce the lines in Figure 3.4.1.

Average volumetric strains and estimated contours of volumetric strain are presented in a graph of peak base acceleration versus relative density before shaking, D_{r0} in Figure 3.4.2.a. The value of D_{r0} for each event included changes due to settlements in previous events. The average volumetric strains were obtained by first finding the average cumulative settlement along the entire cross section shown in Figures 3.3.1 and 3.3.2 from all events. The total volumetric strain was partitioned to different events in proportion to the reading of LVDTs L23 and L27. Figure 3.4.2.a is analogous to the volumetric strain plots from Tokimatsu and Seed [1987] (Fig. 3.4.2.b), except that they plotted stress ratio (which is related to base acceleration) against the corrected standard penetration value (which is related to Dr).

One may expect that it is unlikely for the relative density after shaking, D_{rf}, to exceed 100%. The maximum volumetric strain, ε_{v100}, which corresponds to a final relative density of 100%, is determined from the definitions:

$$Dr_0 = \frac{e_{max} - e_0}{e_{max} - e_{min}} \quad \text{and} \quad \varepsilon_{v100} = \frac{e_0 - e_{min}}{1 + e_0} \quad \text{to be}$$

$$\varepsilon_{v100} = \left(\frac{1 - Dr_0}{Dr_0} \right) \frac{e_{max} - e_0}{1 + e_0} \qquad \text{(Eq. 3.2)}$$

The vertical contours of Figure 3.4.2.a satisfy Eq. 3.2 and hence correspond to a bound on volumetric strains corresponding to a final relative density of 100%. Figure 3.4.2.b presents the plot of Tokimatsu and Seed [1987]. Figures 3.4.2.a and 3.4.2.b were approximately compared by using the Tokimatsu and Seed relationship between $(N_1)_{60}$ and Dr, and by assuming that $\frac{\tau_{av}}{\sigma_0'} = 0.65 \frac{a_{max}}{g} \frac{\sigma_0}{\sigma_0'} \gamma_d$ is roughly equal to $\frac{a_{base\_max}}{g}$ (where, τ_{av} = average cyclic shear stress induced by the earthquake; σ_0 and σ_0' = total and effective overburden pressure at the depth considered; γ_d = stress reduction factor, which varies from a value of 1.0 at the ground surface and to a value of 0.9 at a depth of about 9.0 m; and a_{base_max} = maximum base acceleration measured in the centrifuge experiment). The volumetric strains marked inside the square boxes in Figure 3.4.2.a correspond to the points shown in Figure 3.4.2.b.

3.5 SHEAR STRESS-DISPLACEMENT LOOPS

Figure 3.5.1 shows the process of obtaining the permanent shear displacements by combining acceleration and displacement data. The displacement of the clay layer relative to the base, measured by adding the signals from the displacement transducer (LVDT) that measures displacement relative to the top ring of the model container and that which measures the displacement of the top ring relative to the base, is noted as $d_d(t)$. The relative displacement $d_a(t)$, was calculated by doubly integrating and high pass filtering the difference between the acceleration of the clay and the acceleration of the base. The two displacement time histories, $d_d(t)$ and $d_a(t)$, are shown in Figure 3.5.1 (c). The FFT transforms of the two displacements ($D_d(f)$ and $D_a(f)$) are shown in Figure 3.5.1 (d). A fifth-order, high-pass, non-casual Butterworth filter H(f), with a cutoff frequency of 0.3 Hz (prototype) was applied to the relative displacement obtained from the accelerometer data $D_a(f)$. Then, a mirror image, low-pass filter (1 – H(f)) was applied to the relative displacement from the displacement transducers to produce D(f), the accurate displacement record over the entire frequency range of interest. Figure 3.5.1 (e) shows the resulting combined displacement time history along with the filtered components from the displacement and acceleration transducers [Kutter and Balakrishnan, 1998].

Shear stresses were calculated using the accelerometer recordings using a procedure similar to that proposed by Elgamal et al. [1995]. The vertical array of accelerometers located at the central southern section was used to calculate the shear stresses. Permanent shear displacement of the southern flood plain clay was obtained by using the procedure described above (using L26). Permanent shear displacements at the interface and in the sand layer were not directly measured in the experiment and therefore were estimated by distributing the total displacements measured by the black sand columns proportional to the LVDT (L26) readings in each event.

Shear stress-shear displacement loops at the interface and in the sand layer are compared for tests C80 and U50 during large Kobe events in Figure 3.5.2. It should be noted that instead of plotting shear stress versus shear strain, shear stress versus shear displacements are plotted here because the shear strains were likely to be non-uniform near the clay sand interface. Initial effective overburden stress at the point considered and the thickness of the soil column between the accelerometers considered are also shown in the plot. The observed peak mobilized shear stresses were due to the largest spikes in the accelerations. The peak mobilized stress ratios for C80 at the interface and in the sand layer are 2.14 and 2.33, respectively, whereas for U50, they are 1.73 and 1.37. This difference in the peak mobilized stress ratio between C80 and U50 indicates the effect of density of the sand layer. Furthermore, larger shear resistance and smaller shear displacements in densified model (C80) than in U50 also show the effect of densification of sand. It should be noted that the effect of density on the peak mobilized stress ratio at the interface is less than that in the sand layer. This might be because of the impeded drainage at the interface due to the overlying clay boundary.

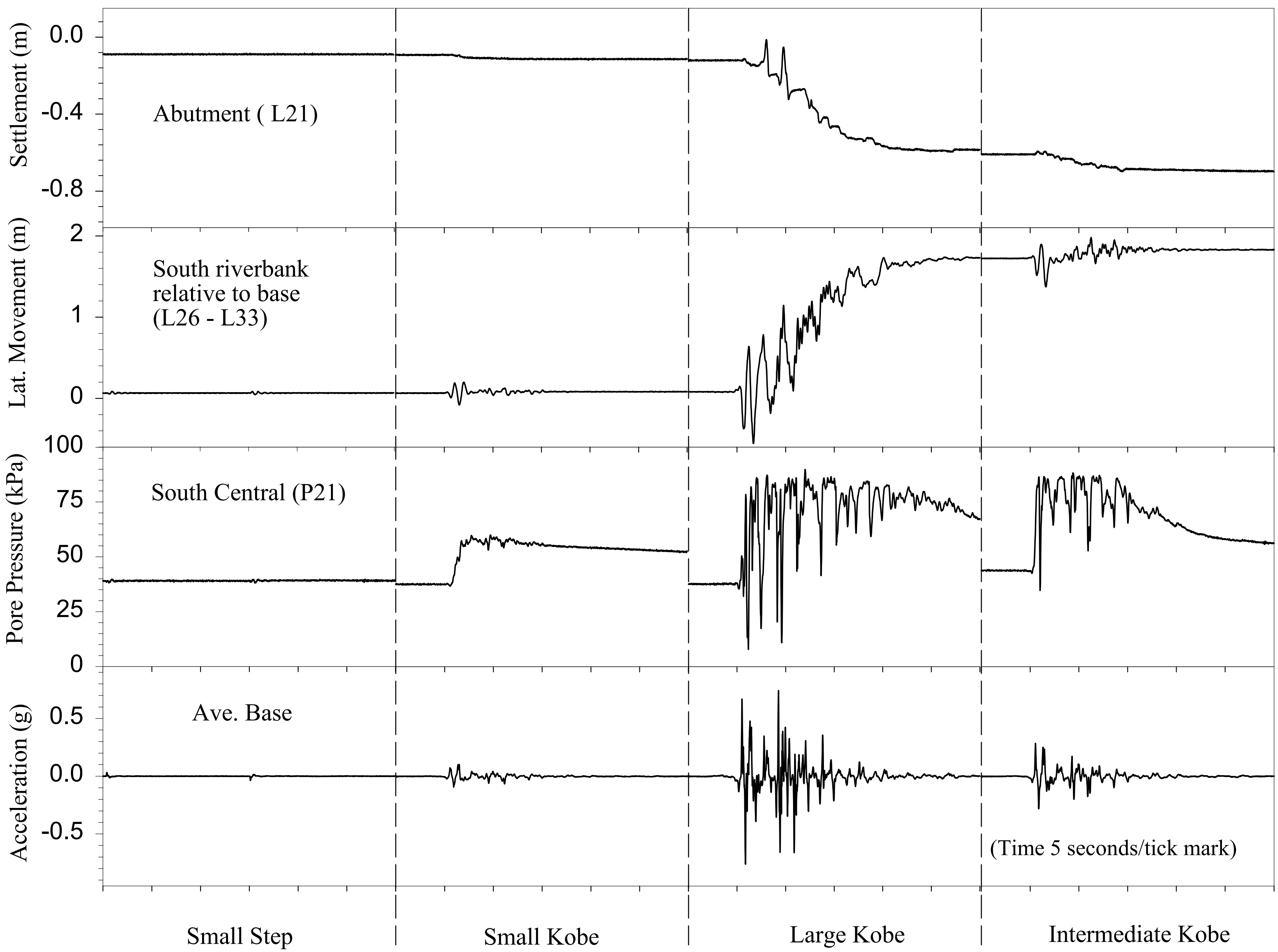

Fig. 3.0.1 Acceleration, pore water pressure, settlement, and lateral movement time histories for different events in U50_4.5

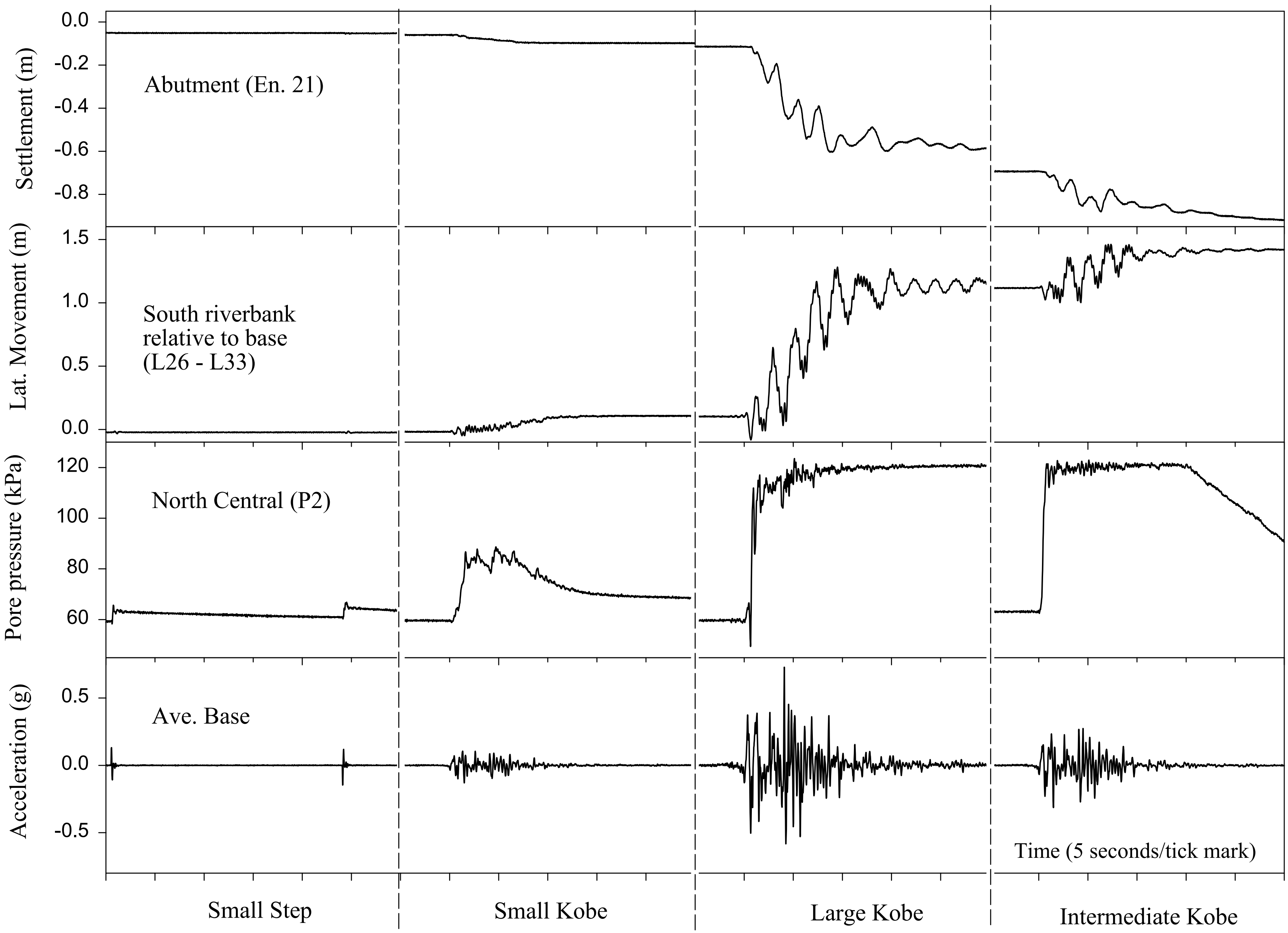

Fig. 3.0.2 Acceleration, pore water pressure, settlement, and lateral movement time histories for different events in U50

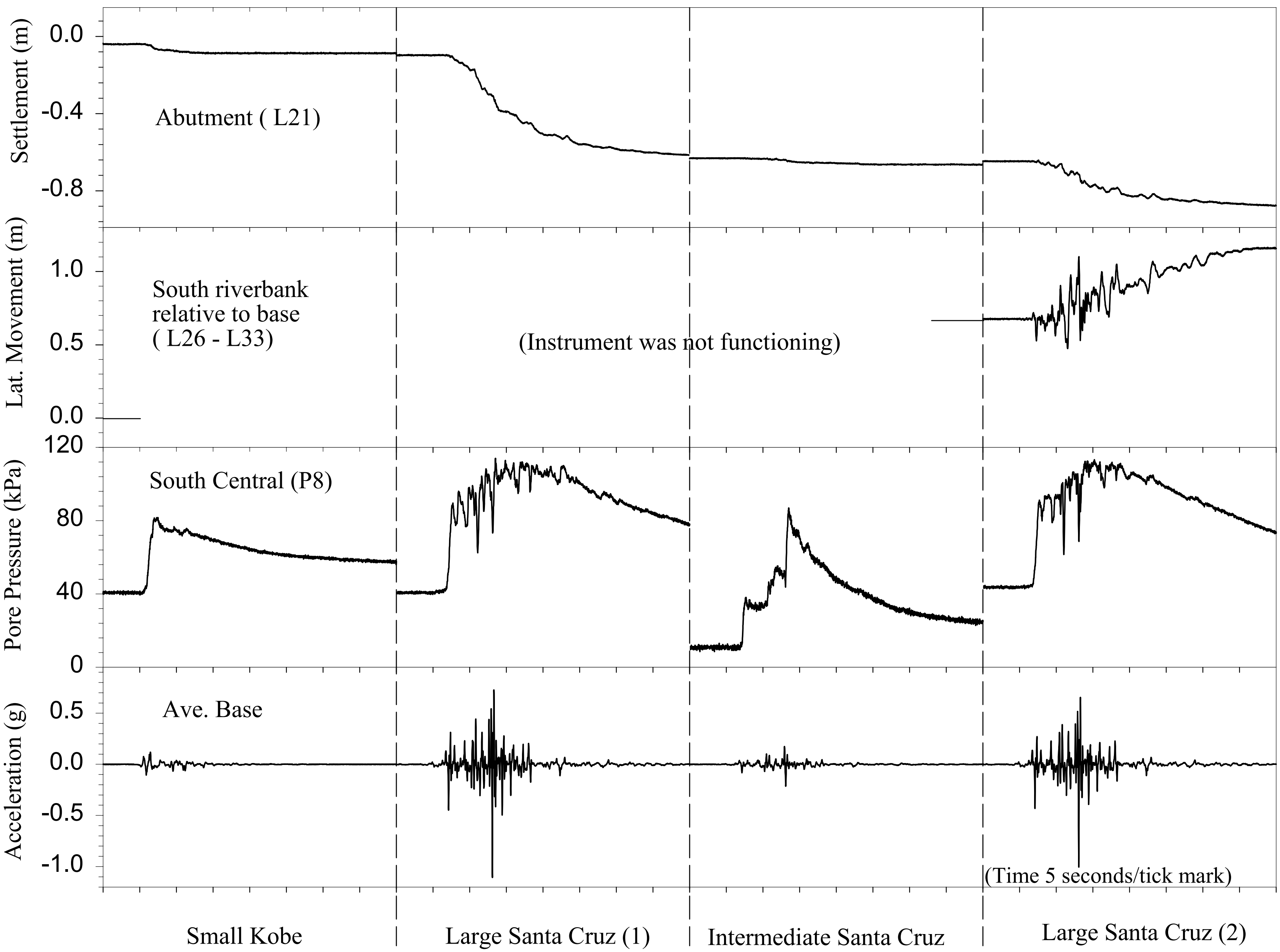

Fig. 3.0.3 Acceleration, pore water pressure, settlement, and lateral movement time histories for different events in U30_4.5M

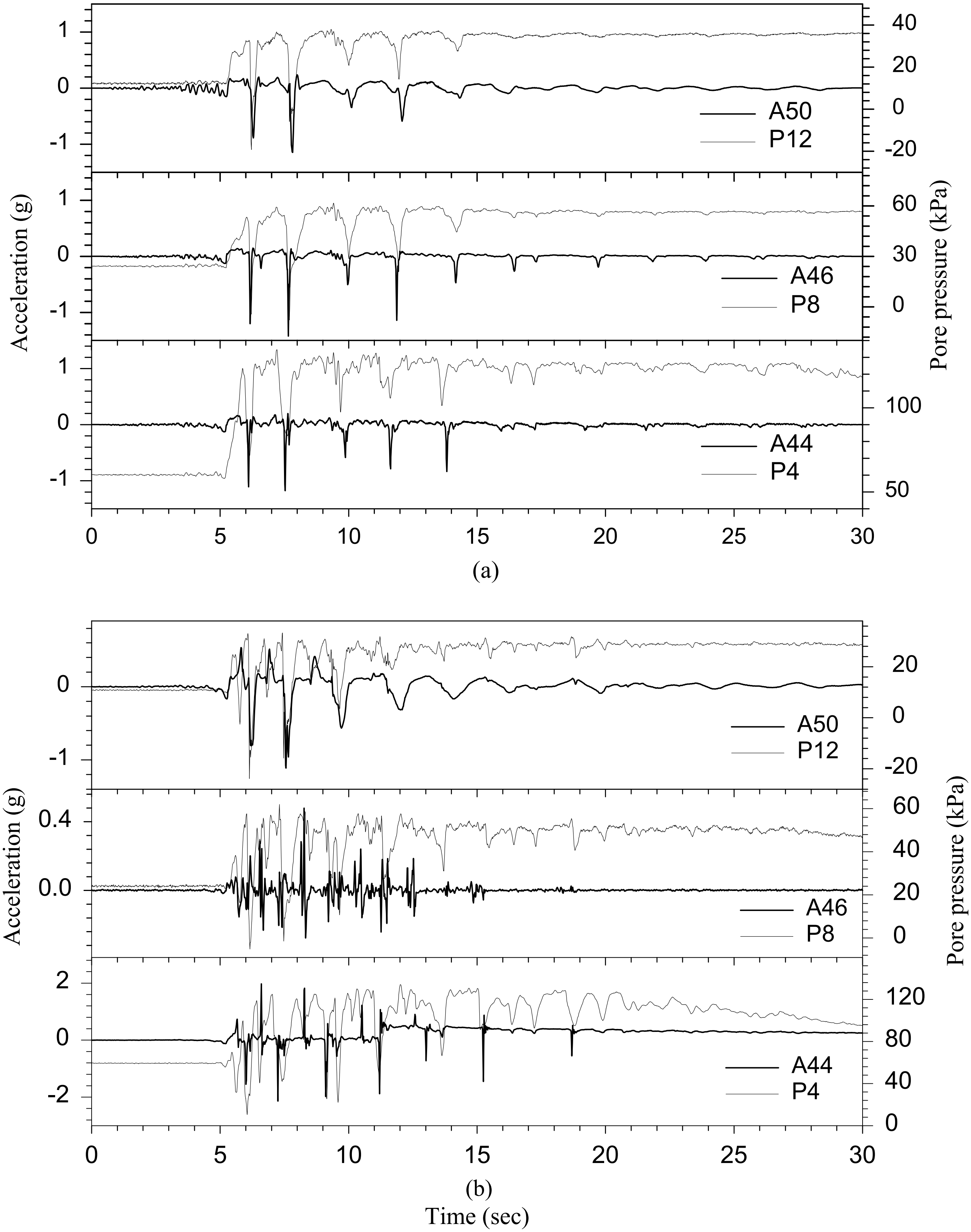

Fig. 3.1.1 Measured accelerations and pore pressures during large Kobe event in (a) U50 and (b) U50_4.5

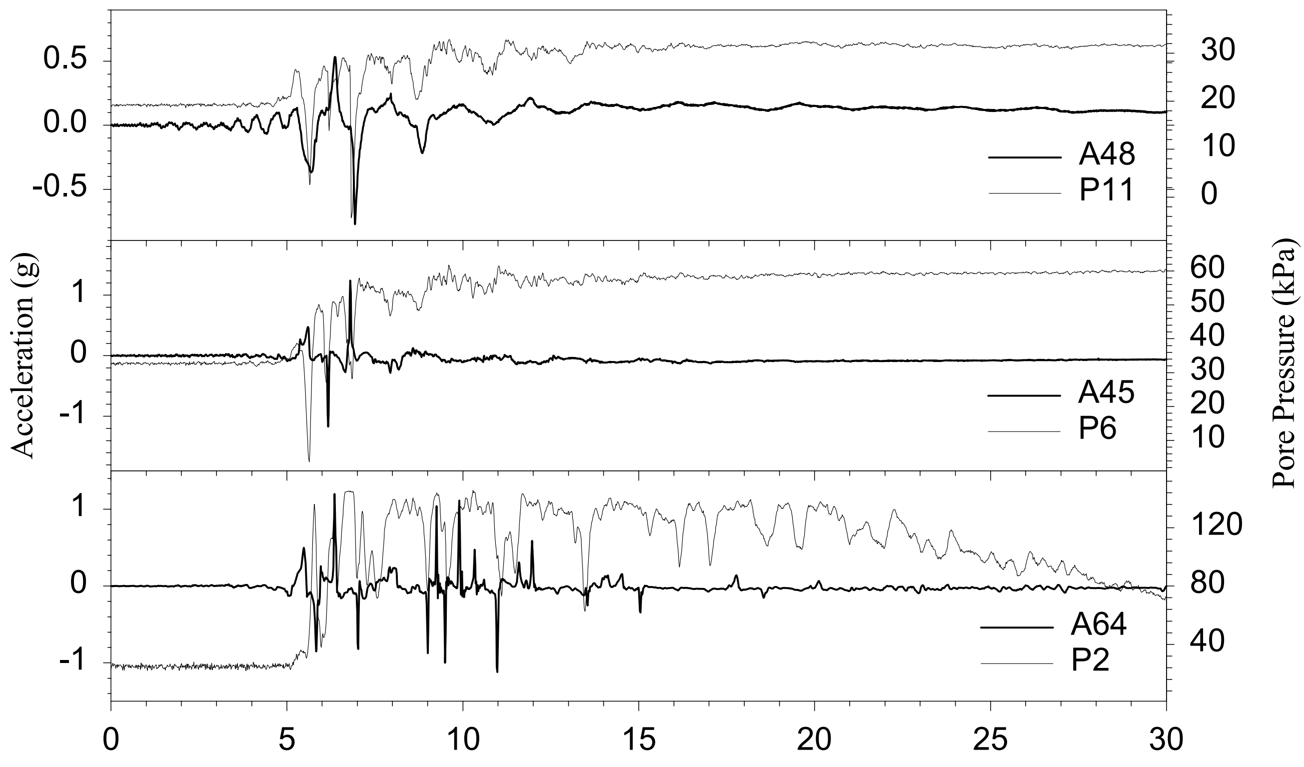

(a)

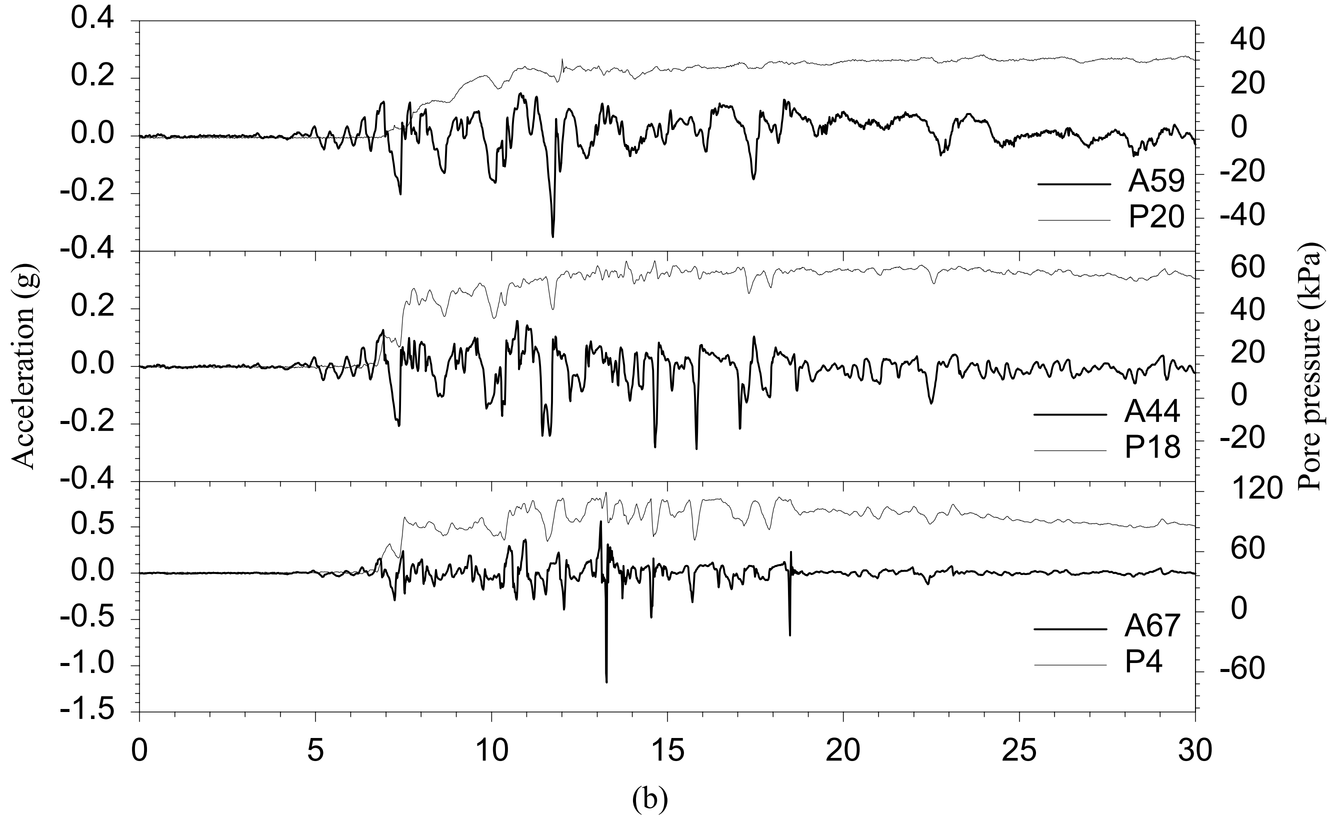

(b)

Time (sec)

Fig. 3.1.2 Measured accelerations and pore pressures during large Kobe event in (a) U30_4.5 and (b) U30_4.5M

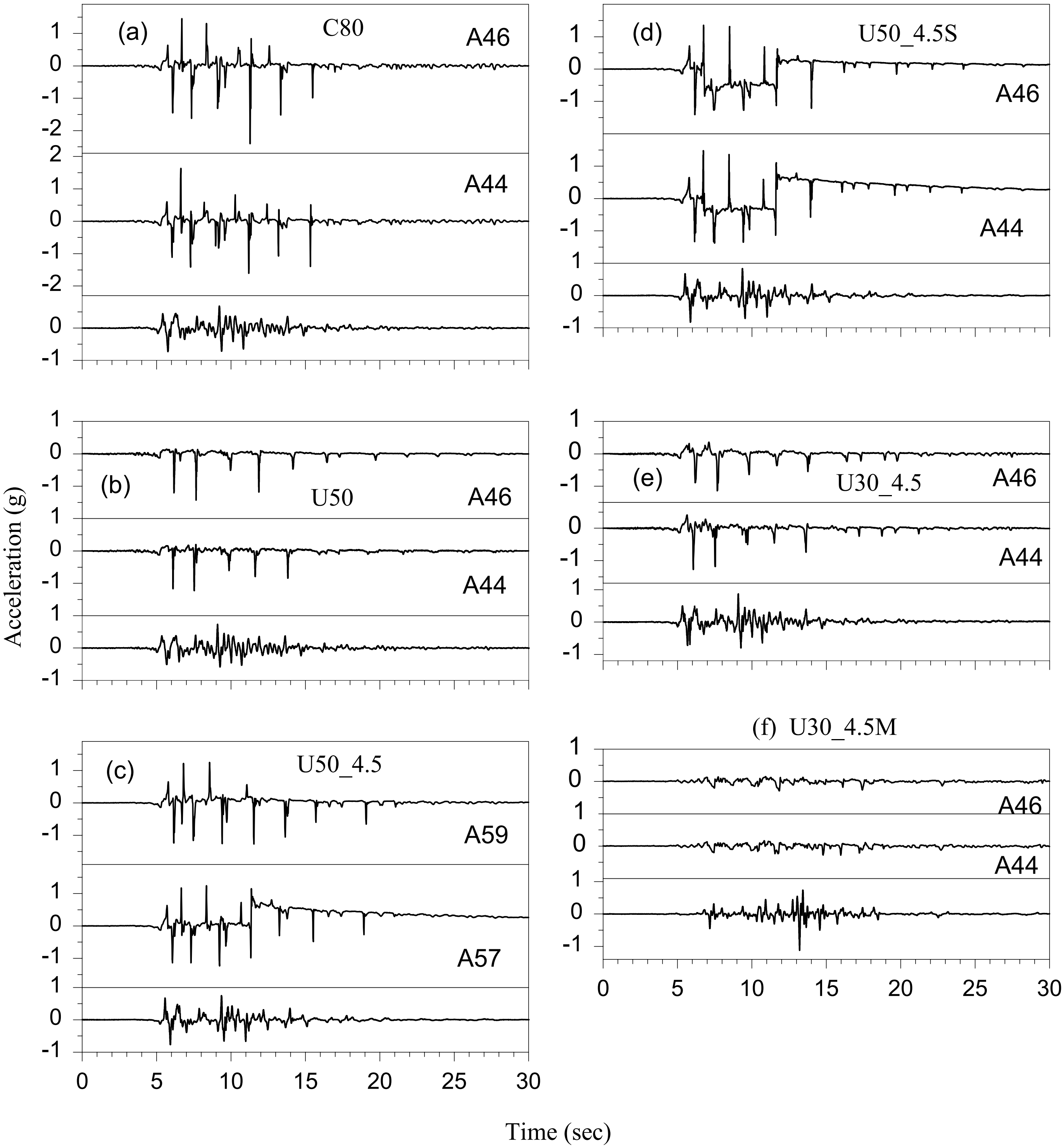

Fig. 3.1.3 Acceleration time histories at the southern portion of the top sand layer along with base acceleration during large events in (a) C80, (b) U50, (c) U50_4.5, (d) U50_4.5S, (e) U30_4.5, (f) U30_4.5M

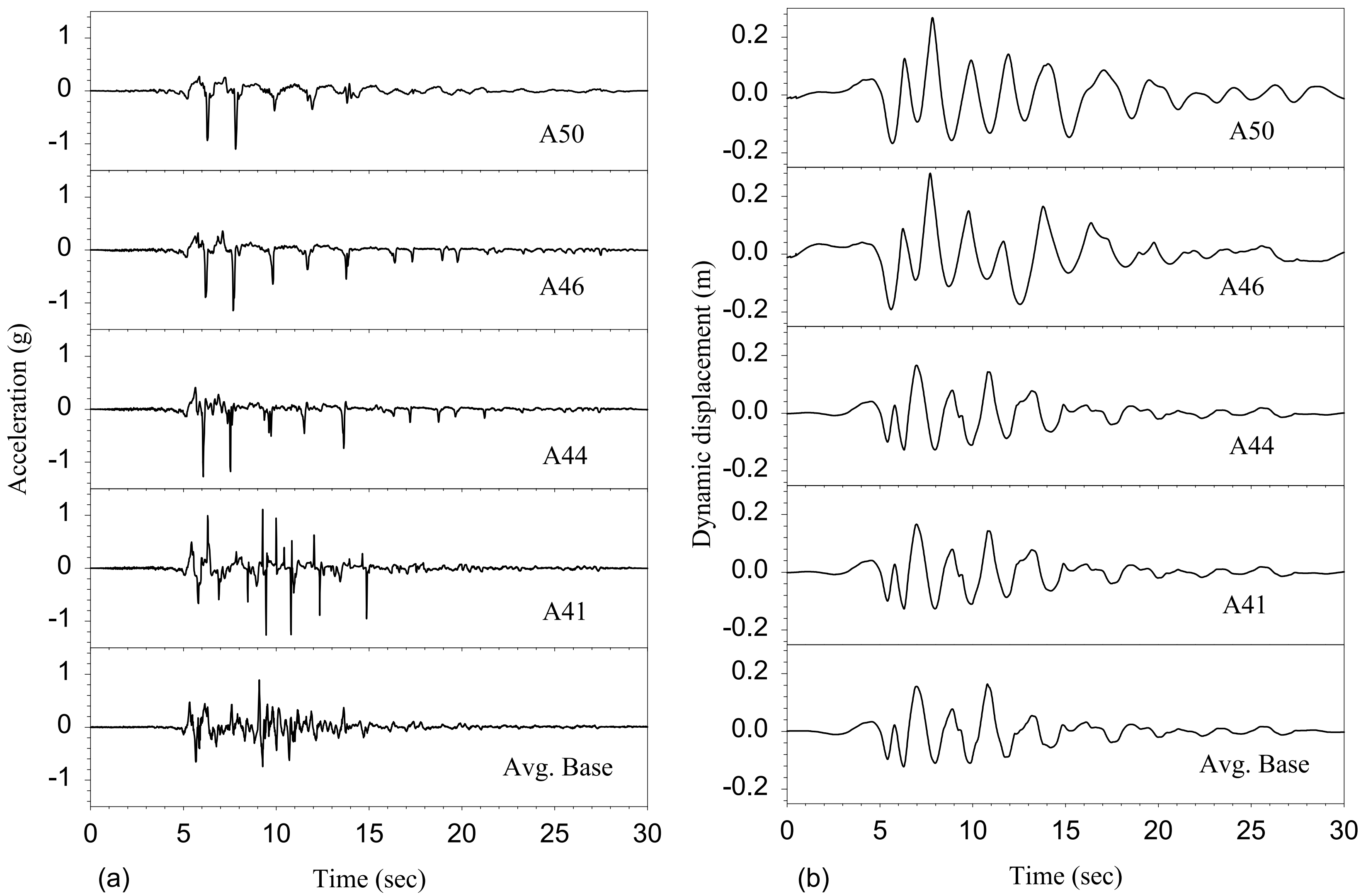

Fig. 3.1.4 (a) Measured accelerations and (b) calculated dynamic displacements from accelerations (high-pass filtered with f_c = 0.15 Hz) at different depths during the large Kobe event in U30_4.5

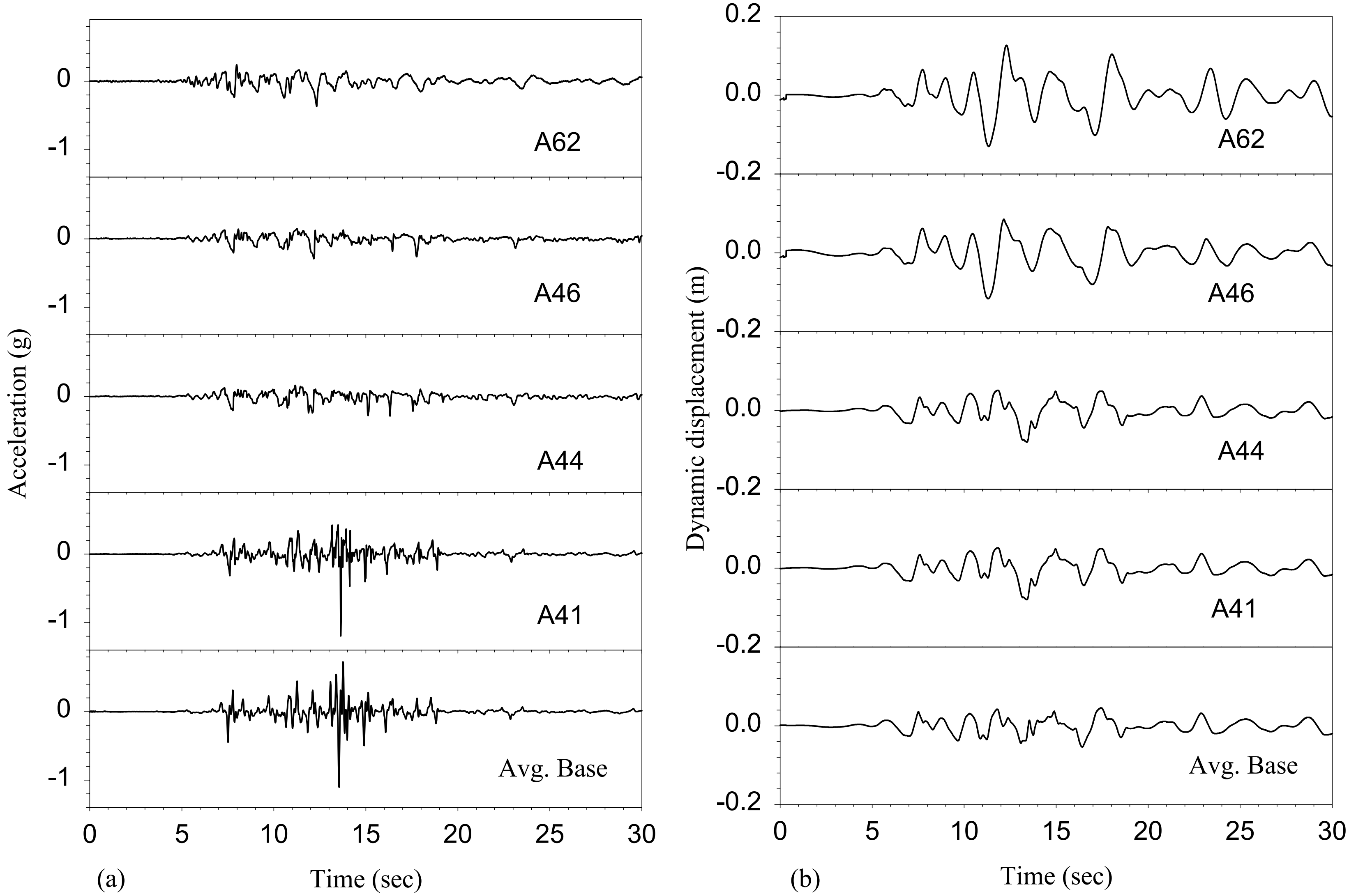

Fig. 3.1.5 (a) Measured accelerations and (b) calculated dynamic displacements from accelerations (high-pass filtered with f_c = 0.15 Hz) at different depths during the large Santa Cruz event in U30_4.5M

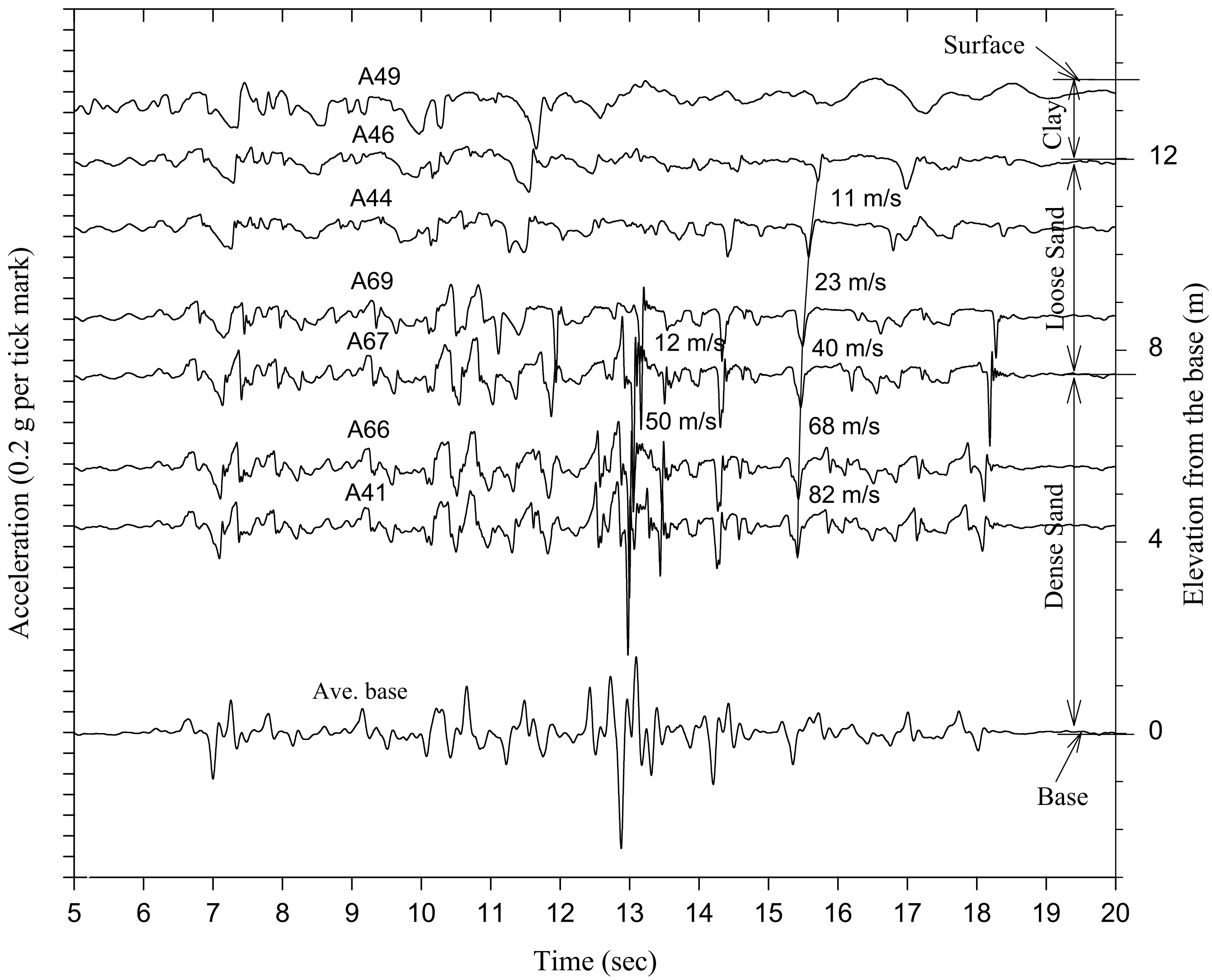

Fig. 3.1.6 Accelerations from the south-central array of test U30_4.5M for large Santa Cruz event (marked with computed shear wave velocities)

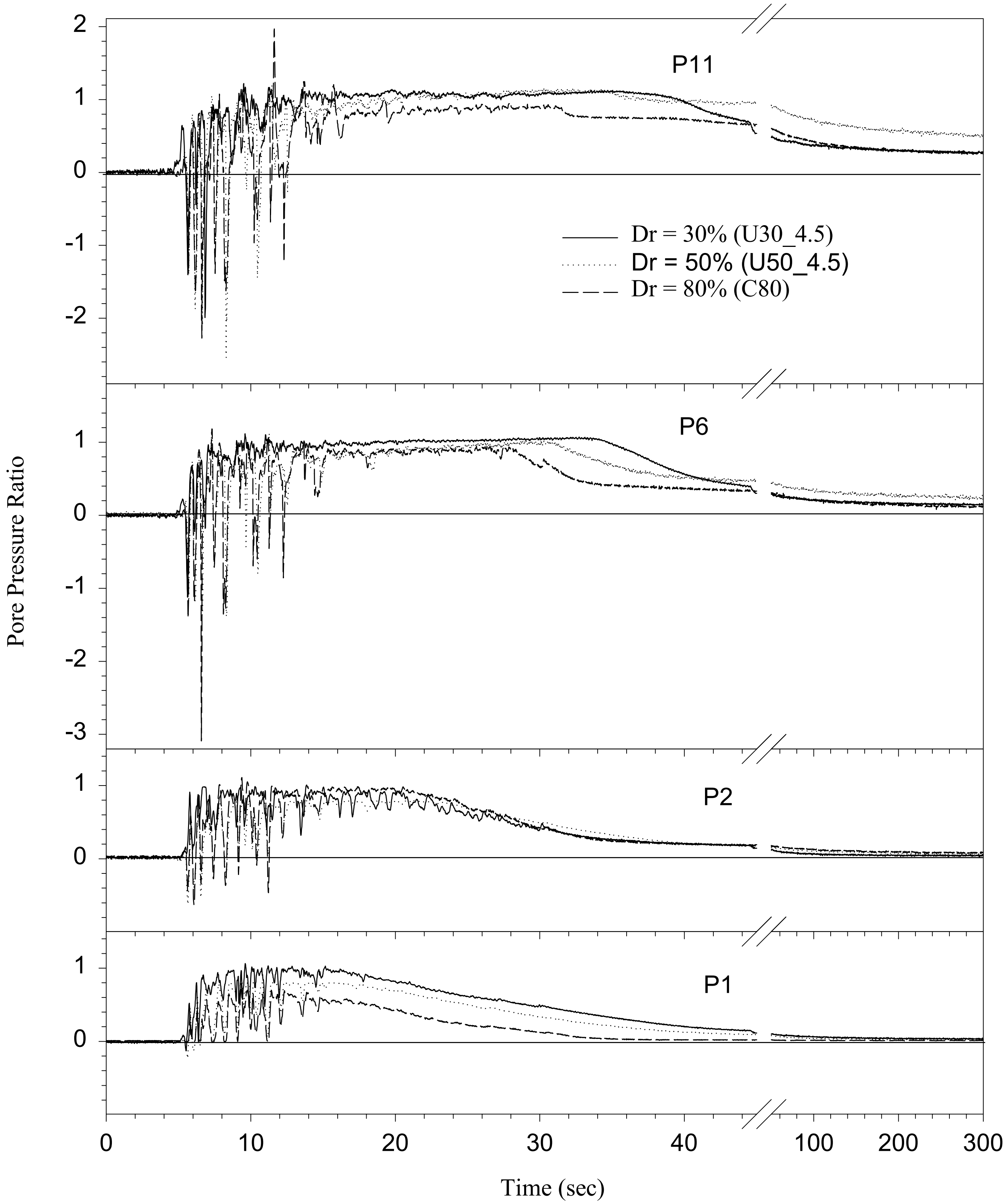

Fig. 3.2.1 Comparison of pore pressure ratios from the north-central portion of U30_4.5, U50_4.5, and C80 for the large Kobe event. (Effect of density)

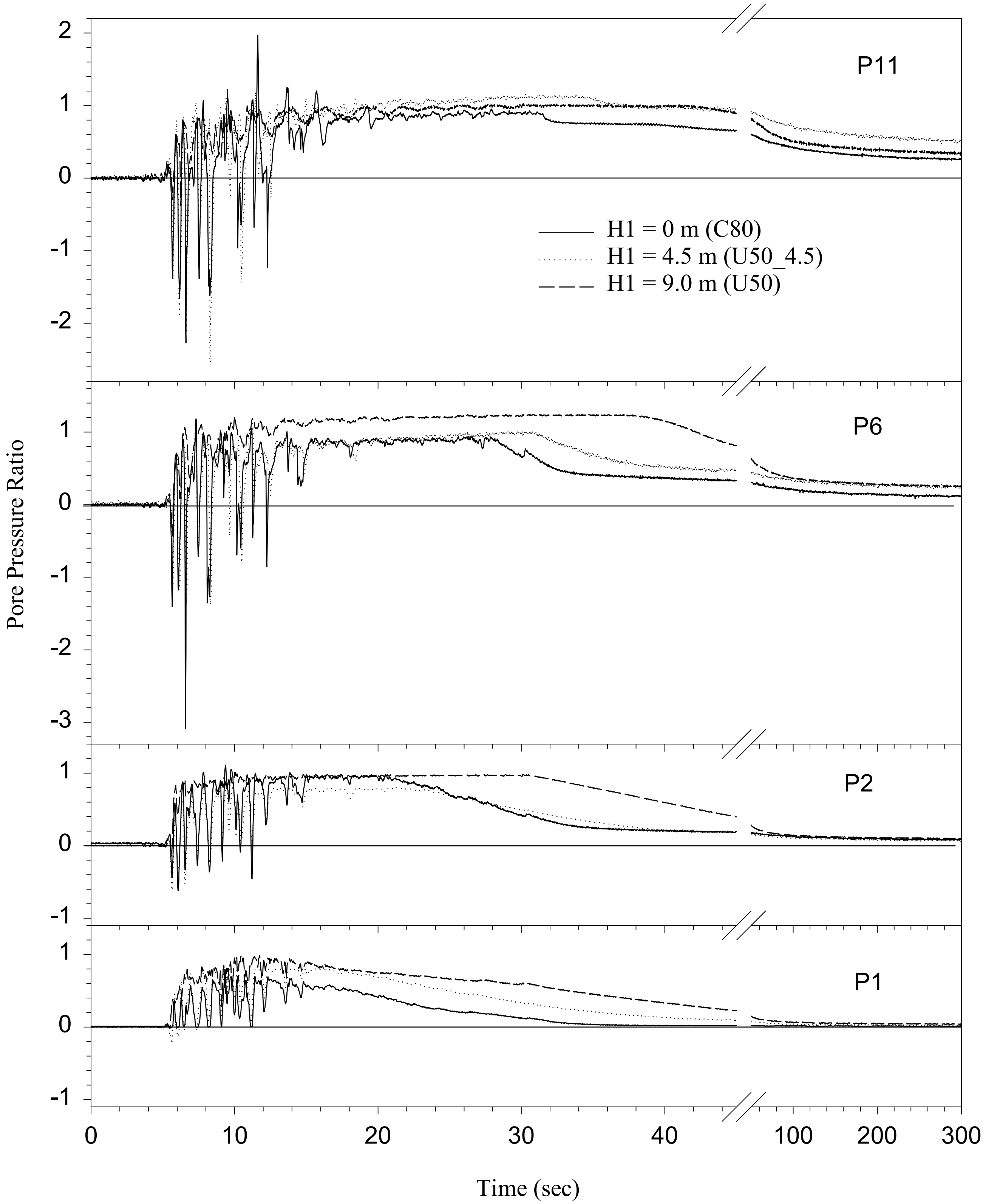

Fig. 3.2.2 Comparison of pore pressure ratios from the north-central portion of C80, U50_4.5, and U50 for the large Kobe event. (Effect of thickness)

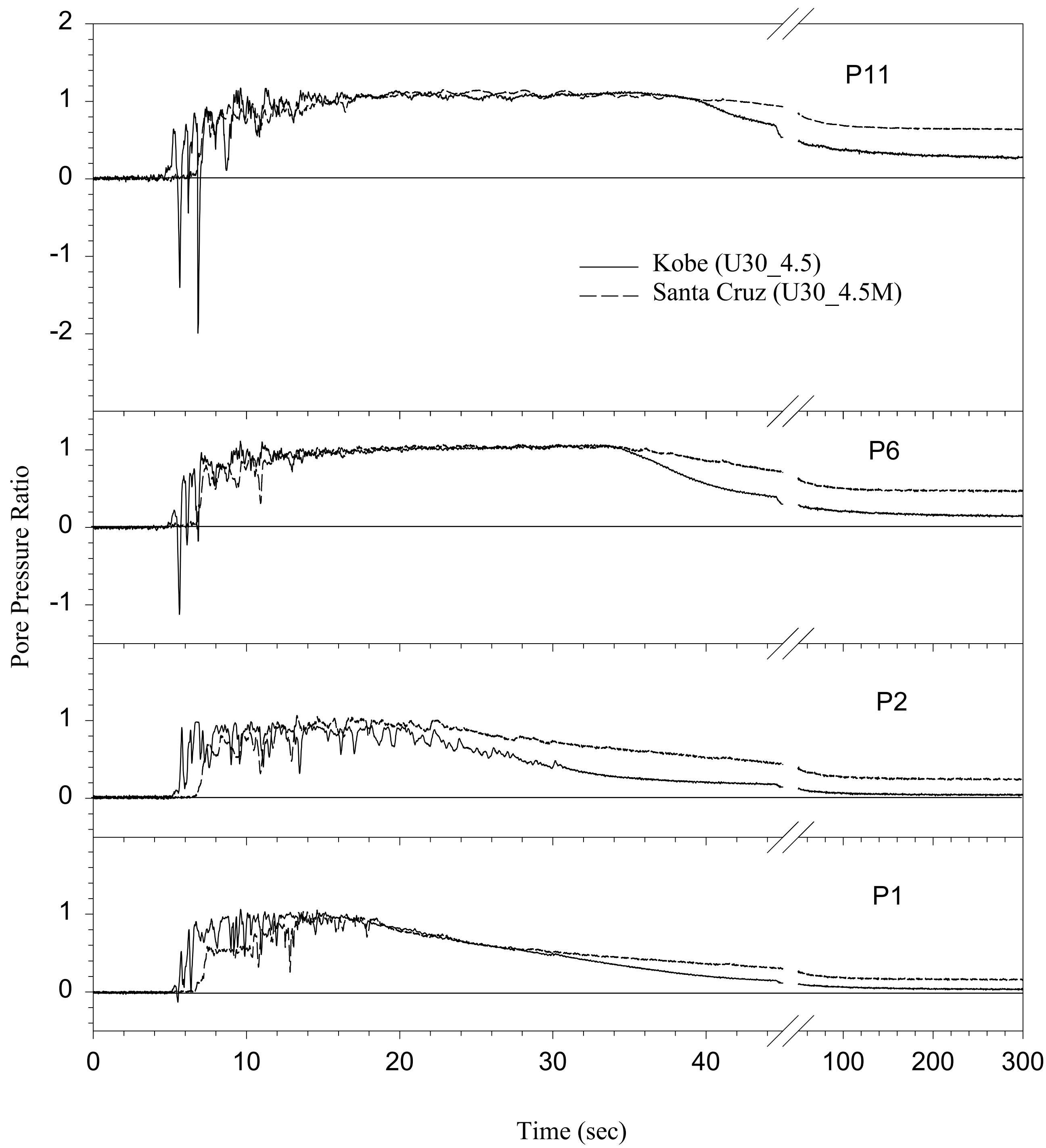

Fig. 3.2.3 Comparison of pore pressure ratios from the north-central portion of U30_4.5 and U30_4.5M for the large events. (Effect of ground motion and ground water table)

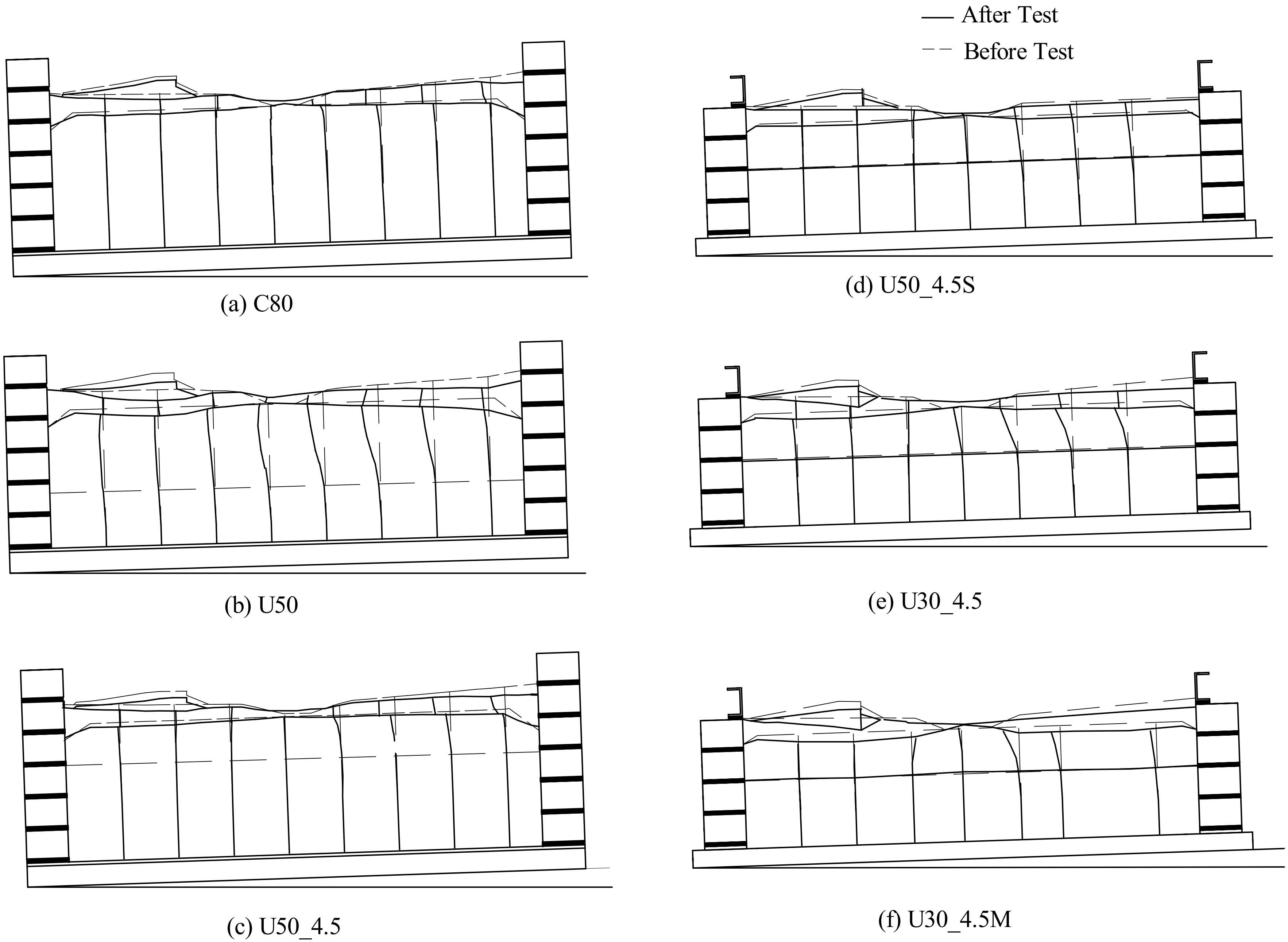

Fig. 3.3.1 Deformed shapes of the models at the middle section (Section A - A)

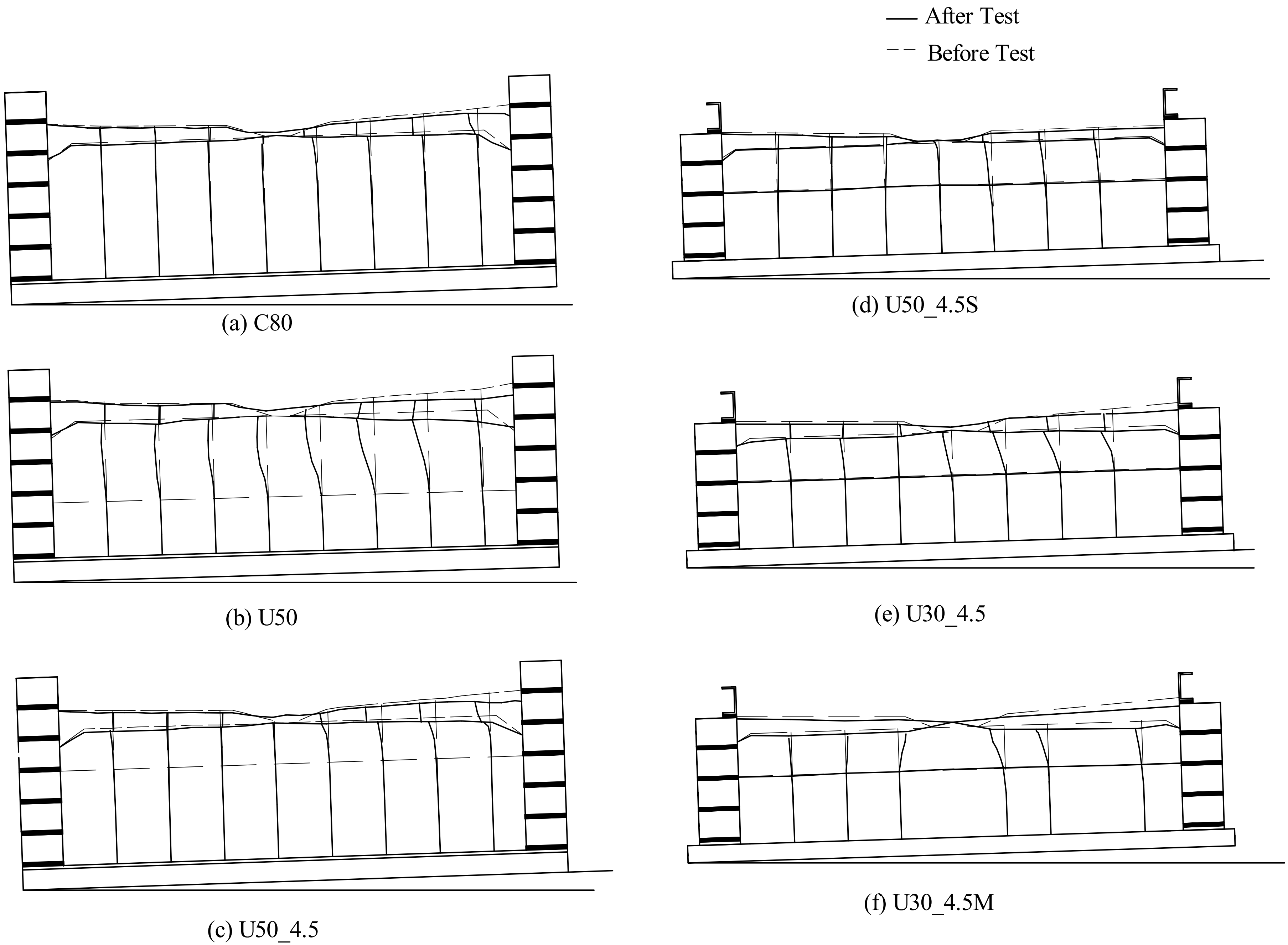

Fig. 3.3.2 Deformed shapes of the models at the east section (Section B - B)

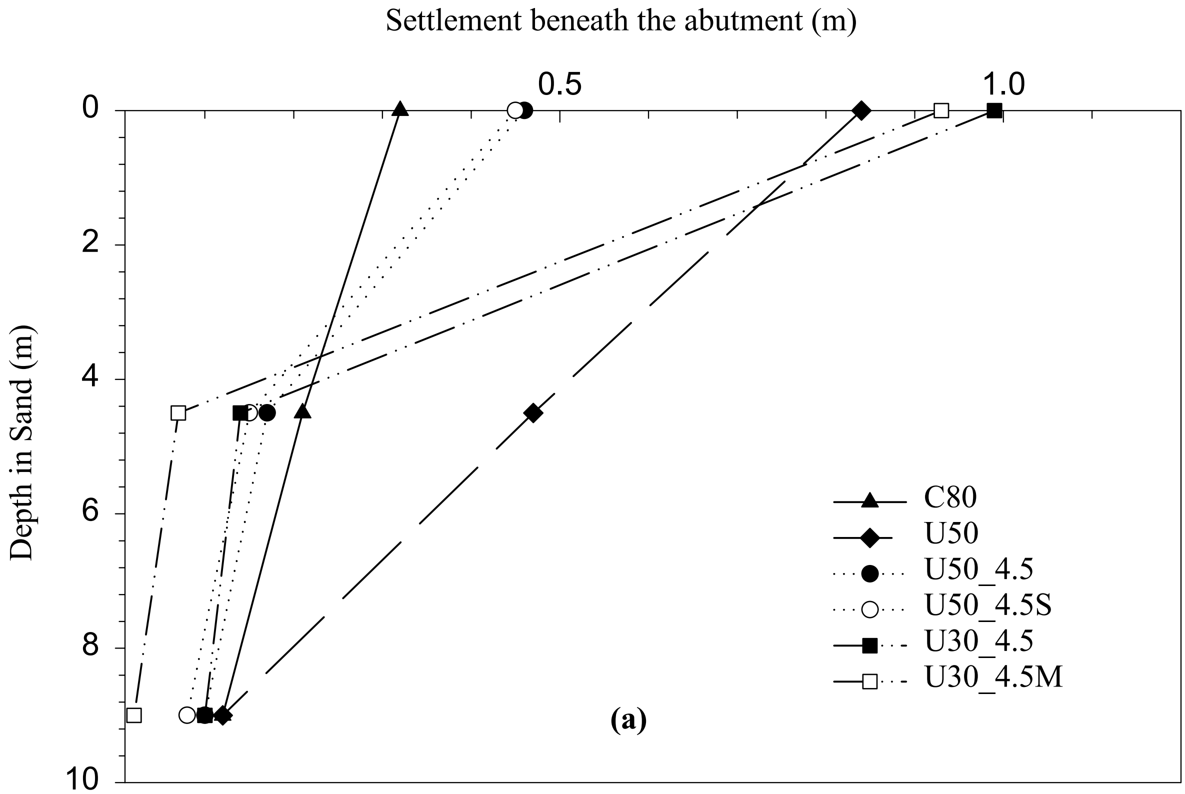

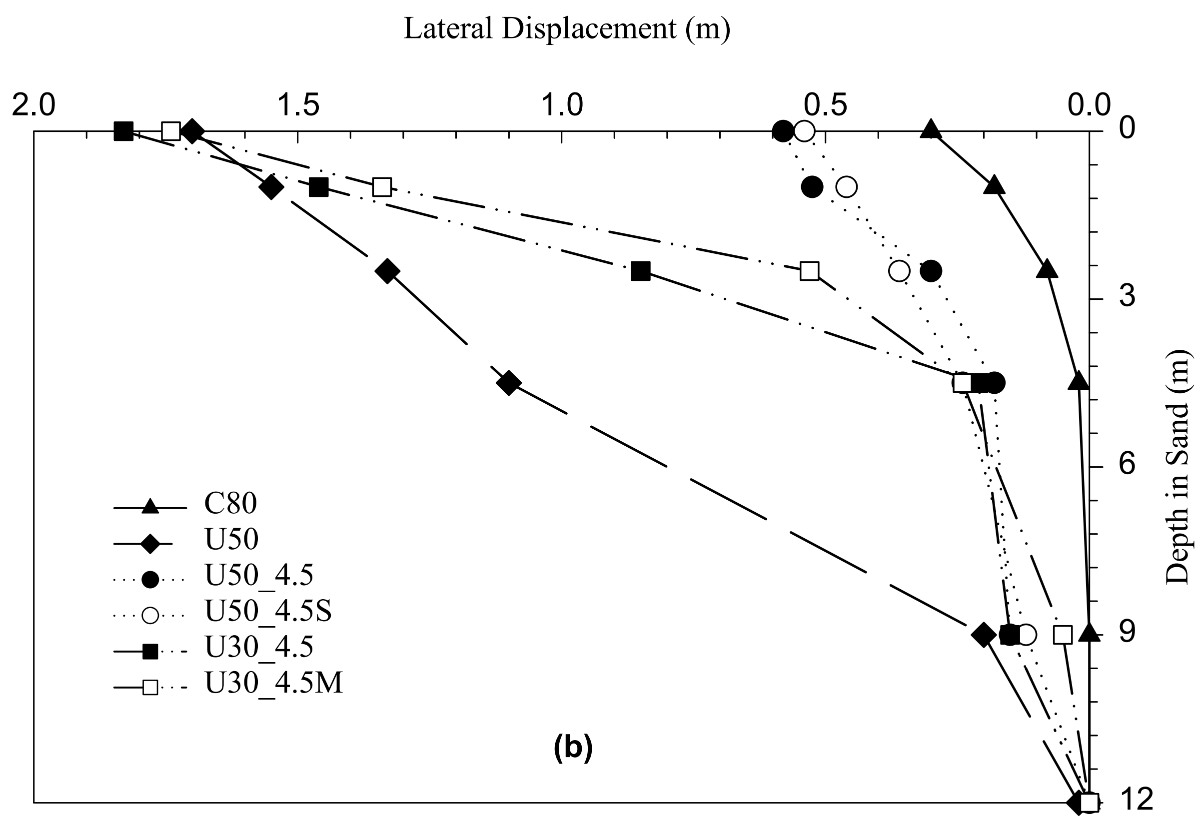

Fig. 3.3.3 Cumulative (a) settlement in the sand layer under abutment and (b) lateral movement of sand at south-central portion in all five or six shaking events

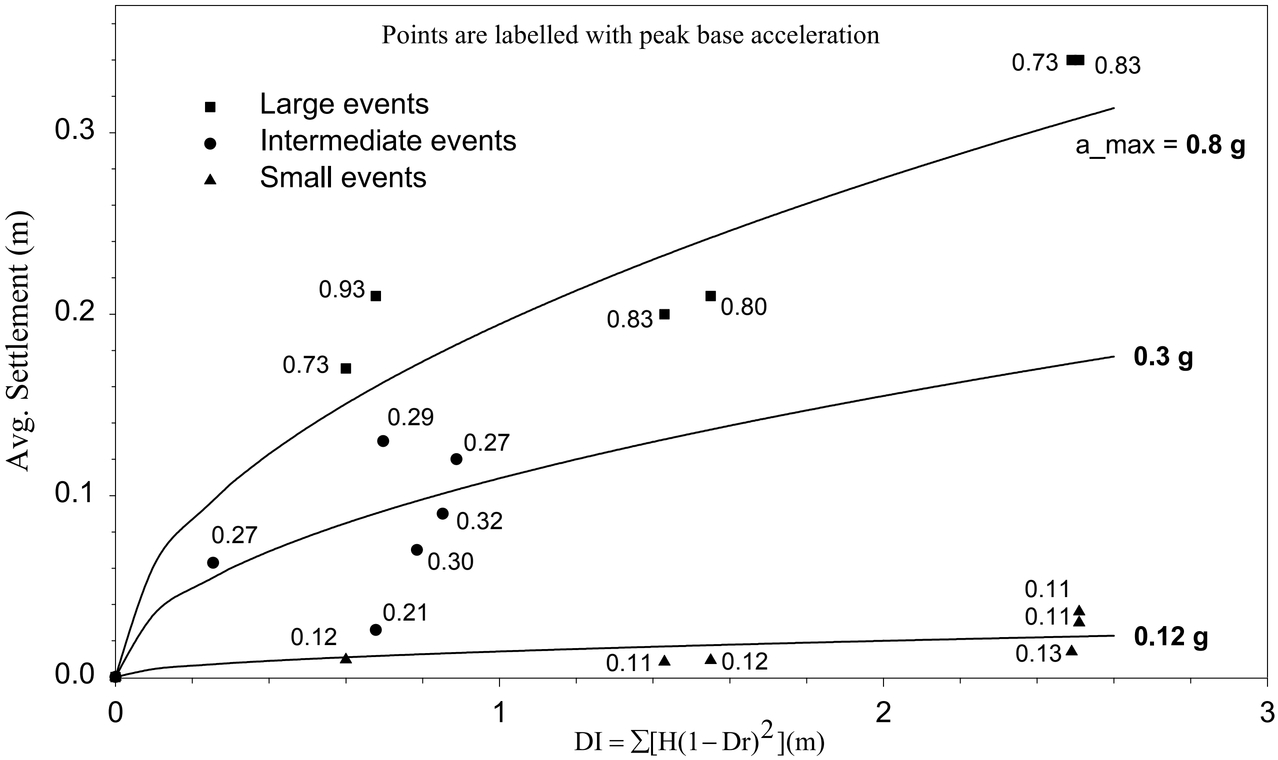

(a)

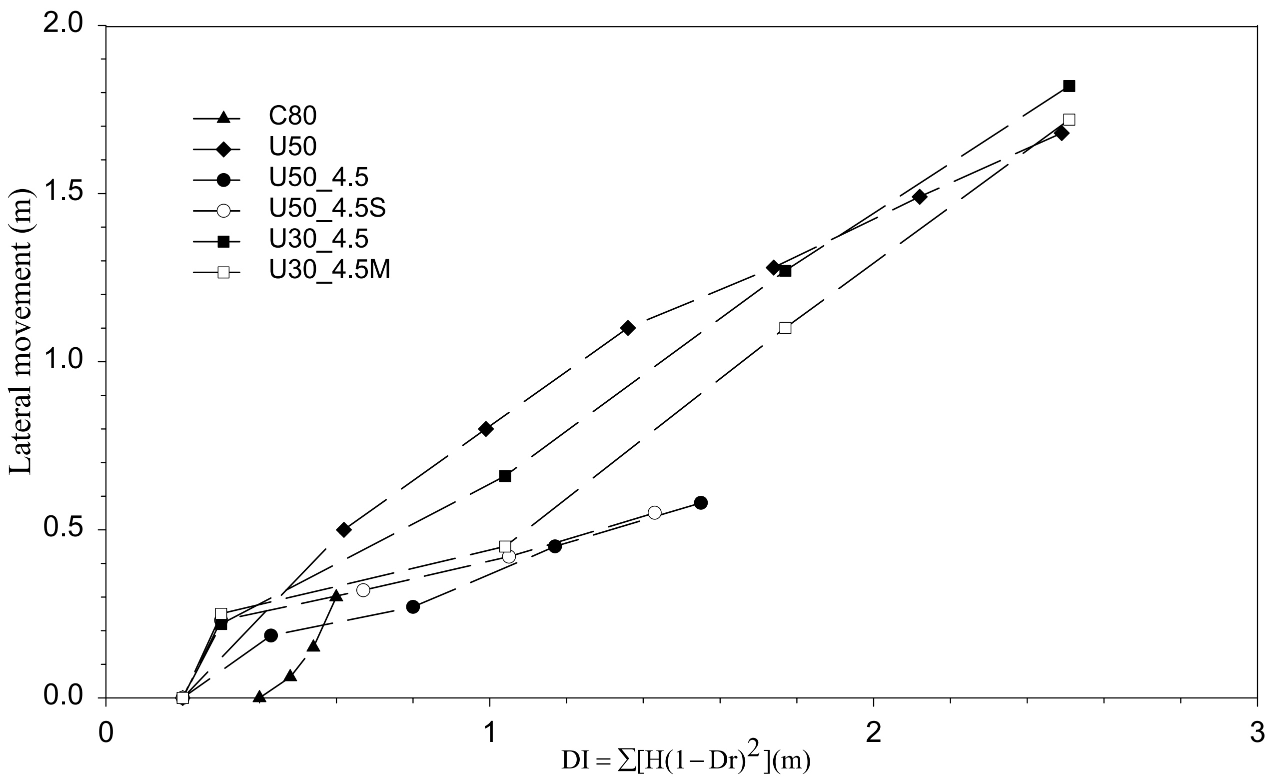

(b)

Fig. 3.4.1 Effect of density and thickness (Deformation Index) on
(a) average settlement over cross section in each event and
(b) cumulative (5 or 6 events) lateral movement of south-central portion

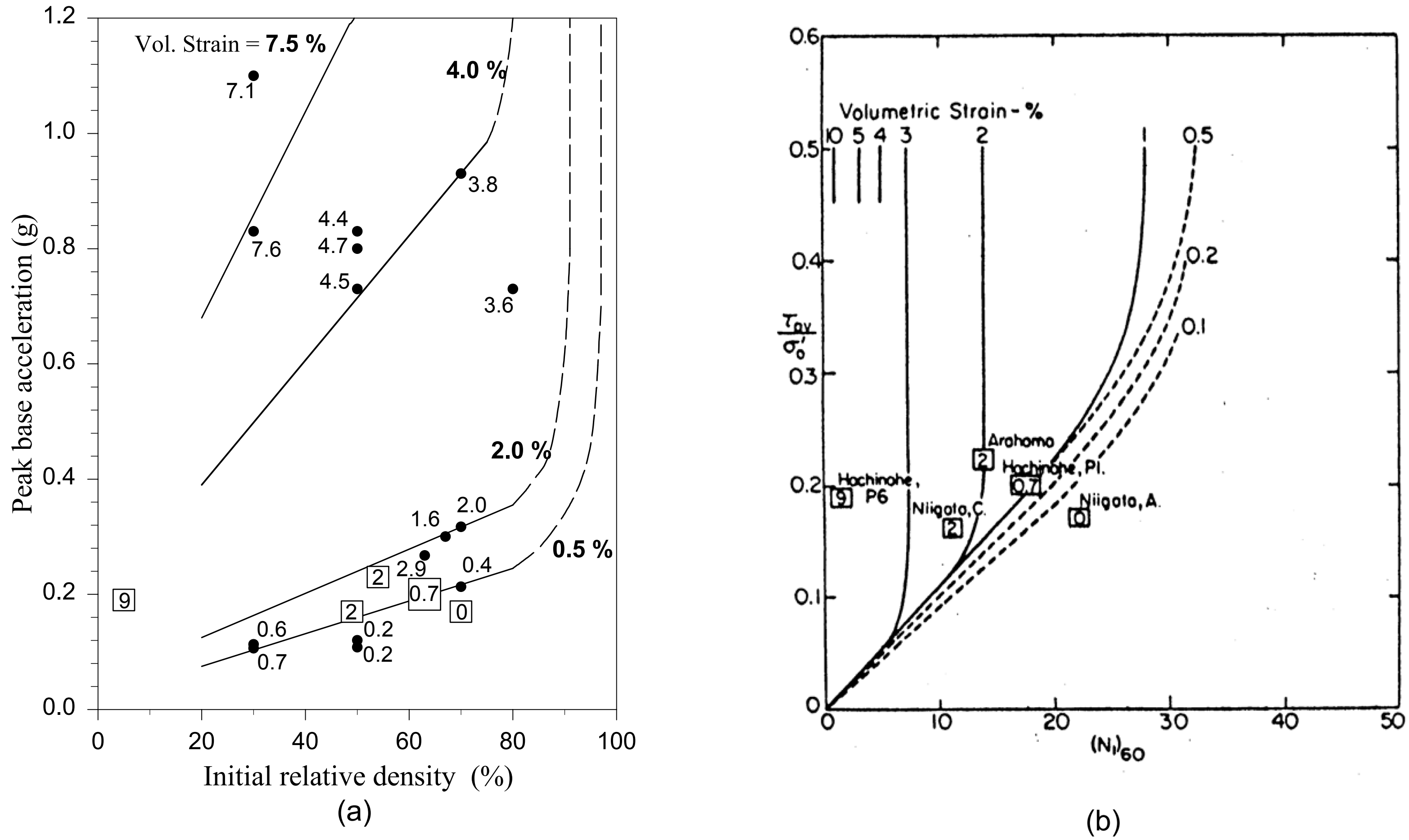

Fig. 3.4.2 Variation of volumetric strains: (a) average permanent strains (points are marked with volumetric strains) and (b) contours proposed by Tokimatsu and Seed (1987)

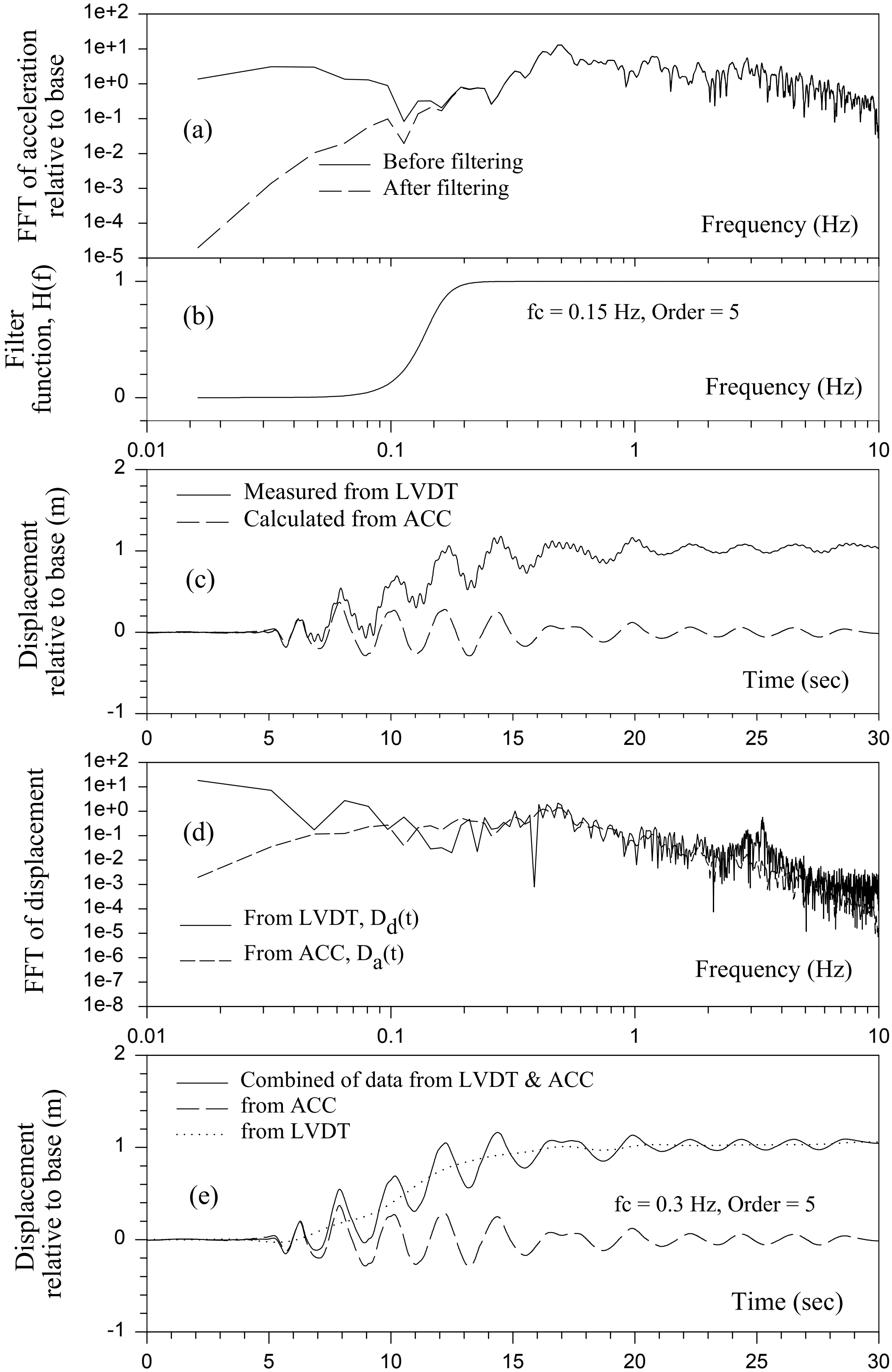

Fig. 3.5.1 Processing and combining acceleration and displacement data

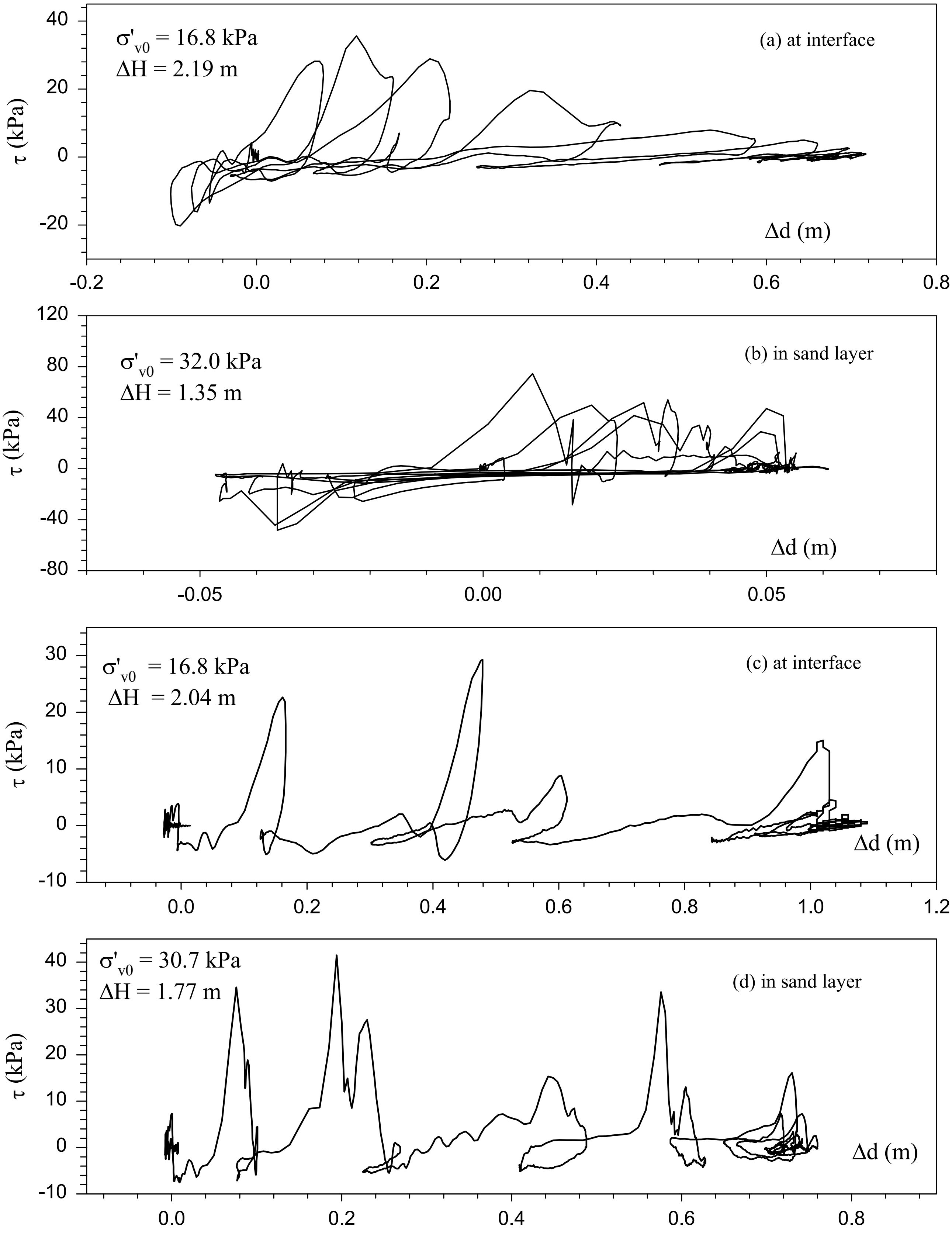

Fig. 3.5.2 Shear stress-displacement loops for large Kobe events in (a), (b) C80 and (c), (d) U50

4 Finite Element Analyses

Finite element analyses were carried out to test their capability to simulate the results of centrifuge model tests. The finite element codes that were used in these analyses are SUMDES (Sites Under Multi Directional Earthquake Shaking) [Li et al., 1992] and Multi-yield models (in OpenSEES) [Yang, 2000]. In both cases, a 1-D small strain finite element analysis was done by considering a column of soil in the south central portion of the models as indicated in Figure 4.0.1. OpenSEES models are capable of 3-D analysis, but we have only performed 1-D analyses to facilitate comparisons with the SUMDES analyses.

Several assumptions and simplifications were made in the analyses of the centrifuge models using a 1-D finite element simulation. Although the south sides of the models consist of a 2-D configuration, the soil response could be influenced by the 3-D effects of the bridge abutment on the north side. The slopes of the clay surface and sand surface are different in the south sides of the models and hence could more accurately be represented by a 2-D configuration. And, the slope of the free surface could also affect the lateral displacement of the adjacent soil. However, since the surface clay layer was thin and the portion considered in this analysis was farther away from the free surface, the portion of the soil sample on the south side could be analyzed using a 1-D simulation by neglecting the 2-D and 3-D above-mentioned effects. In the analyses, soil layers are assumed to extend infinitely in the horizontal direction, but the soil-model container system in dynamic centrifuge experiments represents a 3-D system. Since the model containers used in these tests are the flexible shear beam containers, which were designed to minimize the container effects during dynamic tests, the 1-D approximation is considered to be a reasonable first step in the development of the analysis procedure. The 1-D small strain simulations cannot capture the effect of the changing geometry as large deformations occur. From Figures 3.3.1 and 3.3.2, it is apparent that there is a significant change in geometry in the experiment.

4.1 SUMDES

The finite element program SUMDES was developed by Li et al. [1992] to analyze a horizontally layered site excited by an earthquake loading. The formulation is based on the nonlinear effective stress principle fully coupled with pore water pressure generation and dissipation. The finite element formulation was derived using the equilibrium, continuity, and generalized Darcy equation [Darcy, 1856] and the complete Biot equation [Biot, 1941, 1957, and 1972] for porous media. The two-phase Biot theory was implemented in a u-p formulation, where u is the displacement of the soil skeleton and p is the pore fluid pressure. Although SUMDES is a 1-D code, it is capable of predicting three-dimensional motions and pore water pressure within a soil deposit.

Sloping ground often undergoes permanent lateral deformation during strong earthquakes. The amount of permanent displacement mainly depends on the magnitude of shaking, the layering conditions or soil types, and the slope of the ground. Therefore, in order to analyze 1-D lateral spreading problems, SUMDES was modified to include the effect of sloping ground [Balakrishnan, 2000].

A sloping layer can be approximated as a horizontal layer with the static lateral body force acting in the direction of slope. Therefore the geometry of the problem is still 1-D with a stack of elements normal to the ground surface. Since the lateral body forces depend on the slope, density, and depth in the soil deposit, the initial shear stresses were calculated based on the above factors and applied at the center of each element. The inclusion of the lateral body forces in the SUMDES program is detailed in Balakrishnan [2000].

4.1.1 Constitutive Models and Model Parameters

The SUMDES program [Li et al., 1992] includes implementations of five different constitutive models to simulate the behavior of different soil types under different loading conditions. Table 4.1.1.1 lists all the model types and the number of model parameters associated with each model. Details of these models are described in Li et al. [1992]. The models that are available in SUMDES (Table 4.1.1.1) cover a wide

Table 4.1.1.1 Constitutive models available in SUMDES (Li et al. 1992)

Model Type	Model Name	Number of Parameters
1	Elastic model (pressure sensitive)	2
2	Bounding surface hypoplasticity sand model	20
3	Bounding surface elastoplastic clay model	Either 17 or 19
4	Reduced order bounding surface hypoplasticity model	10
5	Isotropic linear elastic model	2

Table 4.1.1.2 Model parameters for (a) Nevada sand and (b) Bay mud in SUMDES analysis

(a)

Model Parameters	Value
ϕ	32
G_0	265
κ_0	0.004
h_{r1}	1.02
h_{r2}	1.05
d: Dr = 50%	2.0
d: Dr = 80%	9.8
k_{r1}	1.56
k_{r2}	1.62
b	2.0
e_{Γ}	0.84
λ_c	0.007
ζ	0.75
m	1.5
n	0.75

(b)

Model Parameters	Value
ϕ	30
G_0	300
λ	0.016
κ	0.0032
H_r	1.34
d	100
R_p / R_f	1.0
K_r	2.0
b	2.0
H_p	35

range of behavior including elastic, elastoplastic, and hypoplastic, and have the capability to simulate a variety of loading conditions including rotational shear loading. The elastic models (model types 1 and 5) can be used for elastic analysis by using only the elastic moduli as model parameters. The bounding surface hypoplasticity sand model (model type 2) developed by Wang et al. [1990] has the capability to simulate the rotational shear loading in addition to other conventional loading conditions using 20 model parameters. The bounding surface elastoplasticity model (model type 3) was developed by Hermann et al. [1983] to simulate the behavior of clayey soils. The reduced order bounding surface hypoplasticity model (model type 4), which has only 10 model parameters, is a computationally efficient version of the hypoplasticity model (model type 2).

In most of the available constitutive models, different sets of model parameters are required to capture the soil behavior under different densities and confining pressures. To resolve this deficiency, new models were proposed by Manzari and Dafalias [1997] and Li et al. [1999] that have the capability to use the same set of model parameters to simulate the soil behavior for a range of densities and confining pressures. The reduced order bounding surface model in SUMDES (model type 4) was modified by Balakrishnan [2000] according to Li et al. [1999] so that it can be used to simulate the critical state behavior of sand in the centrifuge testing. This new constitutive model was incorporated in SUMDESb as model type 6 with 14 model parameters. The modifications and the details of this new model are described in Balakrishnan [2000].

The new model (model type 6) was used for the Nevada Sand and the reduced order bounding surface hypoplasticity model (model type 4) was used for the Bay Mud in the analysis of centrifuge models. The calibration procedures for model types 4 and 6 are very similar except that some additional parameters are included in model type 6. Detailed descriptions of the calibration procedures of these models were given by Li et al. [1992] and Balakrishnan [2000]. Table 4.1.1.2 shows the model parameters used in the SUMDES analysis.

In order to estimate the appropriate permeability value of the clay to be used in the analysis, a parametric study was conducted. From the parametric study, it was found that if the permeability of the clay was set significantly lower than that of the sand, the trapped water under the clay led to an instability in the calculations and the clay layer would slide away without bound. This is partly attributable to an error in approximating a

2-D problem using a 1-D code. Although the clay layer acts as a less permeable layer, during shaking the developed excess pore water pressure in the sand layer can dissipate two or three dimensionally; for example, laterally toward the river channel or through cracks in the clay. Therefore, finally the permeability of the clay layer was set equal to the permeability of the sand in the SUMDES analyses. Yang and Elgamal analyzed the effect of permeability of a low permeable layer using a fully coupled finite element program called "CYCLIC" [Yang and Elgamal, 2002]. Their findings also show that the effective permeability of the low permeable layer significantly influences the lateral deformation of sloping soil layers.

4.2 ANALYSIS USING OpenSEES

OpenSEES (Open System for Earthquake Engineering Simulation) is a finite element platform developed by PEER (Pacific Earthquake Engineering Research Center). It has a number of constitutive models for different types of analyses including the dynamic analyses of structures and soils. Details of the available analysis types and the executable programs can be obtained via the Internet at **http://opensees.berkeley.edu**.

4.2.1 Constitutive Models and Model Parameters

The constitutive models used in this analysis are PressureDependMultiYield (for sands), PressureIndependMultiYield (for clays), and FluidSolidPorousMaterial (for saturated soils under undrained loading). These models were developed by Yang and Elgamal [Yang, 2000] at UCSD and are currently available in OpenSEES. These models are based on the framework of multi-yield surface plasticity. It is assumed that the material elasticity is linear and isotropic and that the nonlinearity and anisotropy result from plasticity. A non-associated flow rule is employed to define the direction of the increment of plastic strains. The yield function forms a conical surface in the stress space with its apex along the space diagonal.

The constitutive models are the modified version of the models developed by Parra [1996]. Modifications [Yang, 2000] were made to control the slip deformations under a wide range of arbitrary cyclic loading during liquefaction and to include

Table 4.2.1.1 Constitutive model parameters for OpenSEES simulation

Model Parameter	Yang (2000)			Used Values			
	Nevada Sand		Bay Mud	Nevada Sand			Bay Mud
	Dr = 40%	Dr = 80%		Dr = 30%	Dr = 50%	Dr = 80%	
Reference shear modulus (Mpa)	31.36	45.0	3.0	27.5	34.5	45	3.0
Reference mean pressure (kPa)	80.0	80.0	80.0	80.0	80.0	80.0	80.0
Pressure dependence coefficient	0.5	0.5	0.0	0.5	0.5	0.5	0.0
Friction angle (degrees)	32.3	38.0	30.0	30.8	33.7	38.0	30.0
Phase transformation angle (degrees)	26.5	28.0	30.0	27.1	25.8	24	30.0
Contraction parameter 1	0.17	0.07	0.0	0.195	0.145	0.07	0.0
Contraction parameter 2	-0.05	-0.03	0.0	-0.055	-0.045	-0.03	0.0
Dilation parameter 1	0.4	1.0	0.0	0.25	0.55	1.0	0.0
Dilation parameter 2	130.0	130.0	0.0	30.0	30.0	30.0	0.0
Liquefaction parameter 1 (kPa)	10.0	5.0	0.0	11.2	8.75	5.0	0.0
Liquefaction parameter 2 (%)	1.5	0.5	0.0	1.75	1.25	0.5	0.0
Liquefaction parameter 3	3.0	3.0	0.0	3.0	3.0	3.0	0.0
Liquefaction parameter 4	1.0	0.005	0.0	1.25	0.75	0.005	0.0

provisions for cavitation and development of steady state (constant volume). Many models, which were developed in stress-space (controlled by stress path), cannot predict the permanent shear deformations well, since for almost constant shear stresses, large deformations may occur during cyclic loading. The above constitutive models, which are available in OpenSEES, were developed to account for plastic deformations as well. More details of these models can be found in Yang [2000] and Parra [1996].

Yang [2000] analyzed one of the centrifuge models using the above constitutive models but in a different finite element program called "CYCLIC." Calibrated model parameters were used in their analysis for Nevada Sand and Bay Mud. For Nevada Sand, Yang [2000] provided calibrated model parameters for relative densities of Dr = 40% and Dr = 80%. Model parameters at other relative densities of Nevada Sand were obtained by assuming that the parameters vary linearly with the relative density. Table 4.2.2.1 shows the parameters provided by [Yang, 2000] and the values used in our analyses. More details of these model parameters and the calibration procedures are given in Yang [2000]. It should be noted that the value of Dilation Parameter 2 was reduced to 30 from 130, which is the value used by Yang [2000], to avoid the convergence difficulties in the numerical procedures in the OpenSEES analyses.

4.3 COMPARISONS WITH EXPERIMENTAL RESULTS

4.3.1 SUMDES

Figures 4.3.1.1 to 4.3.1.8 show the comparisons of the computed results using SUMDES with the experimentally observed results for tests C80, U50, and U50_4.5 during the large Kobe event for acceleration, pore water pressure, settlement, and lateral movement. Figure 4.3.1.1 shows the computed and measured spectral accelerations in test C80 during the large Kobe event. Computed spectral accelerations are smaller than the experimental ones (especially at higher frequencies). Computed acceleration spikes (Figs. 4.3.1.2 and 4.3.1.3) are shorter and in some cases wider than the experimentally observed acceleration spikes. In the top sand layer, computed acceleration spikes occur before those of the experiments. When a site undergoes a substantial earthquake loading, like the large Kobe event, the soil response can be greatly influenced by rapid pore pressure generation and nonlinear stress-strain behavior. The constitutive model used in this simulation does not follow exactly the stress-strain behavior of sandy soils after liquefaction [Balakrishnan, 2000]. Kutter and Wilson [1999] describe a mechanism of shock wave development due to dilatancy as soils liquefy. This dilative behavior and the shape of the stress-strain loops can influence the wave propagation in soils. The shock wave formation may not be accurately modeled by the chosen parameters [Balakrishnan, 2000].

SUMDES results for pore water pressures (Figs. 4.3.1.4 and 4.3.1.5) seem to show a good agreement with the experimental results. In test U50, although the computed results show a slow rate of development of the excess pore water pressure at the beginning of the shaking, the many negative pore water pressure spikes are similar to those in the experimental results. However, in test C80, the computed results do not show as many negative spikes as the experimental. The difference in this test may be attributed to the dissipation of the pore water pressures at the deep layers. The rate of computed pore water pressure dissipation in deeper soil layers is less than that of experimentally observed dissipation rate. This might be because of the occurrence of sand boils and hence higher pore pressure dissipation rates in the experiments. The occurrence of sand boils and boiling conditions could not be simulated directly in this analysis, and these two results could have been matched if the value of the permeability of the sand layer was adjusted to account for the boiling conditions.

Figure 4.3.1.6 shows the computed and measured lateral movements and settlements at the ground surface in tests C80 and U50 during the large Kobe events. The computed lateral movements show good agreement with the measured lateral movements. However, in the simulation, the clay surface experienced lateral movement even after strong shaking ended; in contrast, lateral movement became constant in the experiments. This might be because of the constant lateral driving forces used in the simulation. In the experiments, the clay surface moved northward, reducing the net slope; hence the southward driving forces were less at the end of shaking than at the beginning. Since the lateral driving forces were constant in the simulation, the ground surface seemed to experience lateral deformation until pore water pressure dissipated or the soil gained some strength to resist the lateral movement.

The settlements at the ground surface computed by SUMDES analysis are much smaller than that of the experiments. In the experiments, a larger portion of the soil reached the liquefaction condition and therefore the rate of water flow might be increased by the increase of permeability associated with boiling conditions. On the other hand, in the SUMDES analysis, a constant permeability value was used throughout the shaking period. This constant permeability constrains the rate of water flow throughout the event and hence the computed settlement rate is much smaller than that observed in the experiments. During the process of liquefaction, soil permeability values change significantly [Schofield, 1981, and Arulanandan and Sybico, 1992]. An artificial increase in the value of soil permeability for the periods of greater pore pressure ratios increases the calculated settlement [Manzari and Arulanandan, 1993]. To properly account for the effect of sand boiling in a numerical analysis, the soil permeability could be considered as a function of excess pore pressure ratio [Balakrishnan 2000].

Figure 4.3.1.8 shows the comparisons of computed accelerations, pore water pressures, settlement and lateral movement with the experimentally measured records all in a single plot for test U50_4.5.

Figure 4.3.1.7 shows the shear stress-shear displacement loops computed from the SUMDES analysis for tests C80 and U50 at interface and in the sand layer for the large Kobe events. The shapes of the stress-displacement loops of SUMDES simulation are somewhat different from that of centrifuge experimental results (Fig. 3.5.2). The experimental results show at least a smaller shear resistance for a large range of shear displacements. In test U50, the shear stresses from the experiment were mostly positive, whereas in the simulation they were both positive and negative. Both measured and computed results show an increase in shear displacement at the later part of the event. The peak shear stresses obtained from the SUMDES simulation were lower than the measured peak shear resistance in the experiments.

4.3.2 OpenSEES

Figures 4.3.2.1 to 4.3.2.9 show the comparisons of the computed results with the experimental results for the large Kobe and large Santa Cruz events for acceleration, pore water pressure, settlement, lateral movement, and shear stress-shear strain loops. Figure

4.3.2.1 shows the computed and measured spectral accelerations in test C80 during the large Kobe event. Similar to SUMDES analysis, computed spectral accelerations in OpenSEES analysis are smaller than those measured in the experiments. The computed accelerations (Figs 4.3.2.2 and 4.3.2.3) for tests C80 and U50 at lower sand region (A41) compare well with the measured accelerations. When it comes close to the interface and in clay layer, the computed peak accelerations are smaller than that of the experiments. The finite element simulations do not actually show the large negative spikes in the acceleration time history, which were caused by the dilative behavior of sands during undrained cyclic loading.

Comparisons of computed and measured pore water pressure time histories (Figs. 4.3.2.4 and 4.3.2.5) show that the finite element simulations both underpredict the negative pore pressure spikes caused by the dilatancy of the sand and consistently show smaller pore water pressures than that of the experiment at all locations for tests C80 and U50. The high excess pore water pressures observed in the experiments might have been caused by the increase in the water table due to liquefaction and the increase in the depth of the pore pressure transducers due to the settlement of sand. Computed pore water pressures from OpenSEES remain constant even after the end of strong shaking, because the dissipation of pore water pressures were not simulated in the finite element analysis. Since the OpenSEES formulation did not allow the pore water pressures to dissipate, they predicted almost zero vertical settlements at the ground surface (Fig. 4.3.2.6). The small settlements shown are associated with the lateral deformation downslope. It should be noted that SUMDES does allow drainage, but also underpredicts the settlements. The current formulation of OpenSEES allows for modeling coupled solid-fluid situations. These coupled models are relevant to the conducted work but were not available when the research was being conducted.

Measured and calculated settlement and lateral movement time histories of the clay layer are shown in Figure 4.3.2.6. The prediction of lateral movement of clay in test U50 compares fairly well with the experimentally observed movement. However for C80, the computed lateral movement of the clay is smaller than that observed in the experiments. This might be because of the underlying dense sand (Dr = 80%) in model C80. In experiments, all the models showed almost the same amount of lateral movement of clay regardless of the density and thickness of the underlying sand layer. In contrast, the finite element analysis results for the lateral movement of clay seems to be dependent on the density of the underlying sand layer.

Figure 4.3.2.8 shows the comparisons of computed accelerations, pore water pressures, settlement, and lateral movement with the experimentally measured records all in a single plot for test U50_4.5. Simulation of test U50_4.5 shows more negative pore water pressure spikes compared to the simulations of tests C80 and U50.

Figure 4.3.2.7 shows the shear stress-shear strain loops at the interface and in the sand layer for tests C80 and U50. They all show similar shapes: at the beginning of shaking, they show closed loops of shear stresses with very low shear strains, but during the strong shaking, shear strain increases and shear strength decreases. Shear stresses obtained by the finite element simulation are constantly smaller than those of the experiments in all cases. The experimental results show the regain in shear strengths at larger shear displacements; in contrast the computed results show a gradual reduction in shear strength as shear strain increases. This observation and the computed results of acceleration and pore water pressure time histories show that the dilative behavior of sands and the rapid increase in shear strength are not simulated very accurately in the finite element analysis. The experiments also show a large cyclic straining superimposed on the lateral movement. The calculations show a gradual increase of lateral movement without the large cyclic straining.

Figure 4.3.2.9 illustrates the comparison of the computed lateral movements of sand at different depths with the experimental results during large events in all six model tests. The experimental lateral movements were obtained by measuring the lateral movements of sand at different depths after tests and then by distributing them to each individual event in proportion to the measured lateral movement of the clay layer in each event. Lateral movements of the clay layer are not included in these plots, because, as mentioned in section 3.3, lateral movements of clay were not sensitive to the thickness and density of the underlying sand, and almost the same amount of movement was observed in all tests except test U50_4.5S, where the slope of the clay layer was changed. In general, the computed lateral movements of sand agree reasonably well with the experimental results. In models U30_4.5 and U30_4.5M, the computed lateral movements of Dr = 80% sand (below 4.5 m depth) show good agreement with the measured values. However, in the top loose sand layer (Dr = 30%), the computed movements are larger than the experimental results although the movements at the top of the ground surface are very close to the measured values. In the analysis, the top loose sand layer seemed to move as a whole to a constant value, resulting in very small shear strains in the loose sand layer but larger shear strains at the loose sand-dense sand interface. The experimental results show almost a uniform shear strain distribution in the loose sand layer. In tests U50_4.5 and U50_4.5S, the computed movements of the top of the medium dense sand layer (Dr = 50%) are about 40% larger than the experimental movements. Computed and experimental results compare well for test C80. The top 2 m of Dr = 80% sand seemed to move more than what the deeper layers did. On the other hand, experimental results show a gradual decrease in lateral movements as the depth increases. The finite element simulation underpredicts the movement of the top Dr = 50% sand layer in test U50. By comparing the results of U50, U50_4.5, and U50_4.5S, it can be said that finite element simulation gives almost the same amount of movement in a Dr = 50% sand layer regardless of the thickness of the layer. The reason for the larger movements observed in experiment U50 is the increased thickness of the Dr = 50% sand layer (from 4.5 m to 9.0 m).

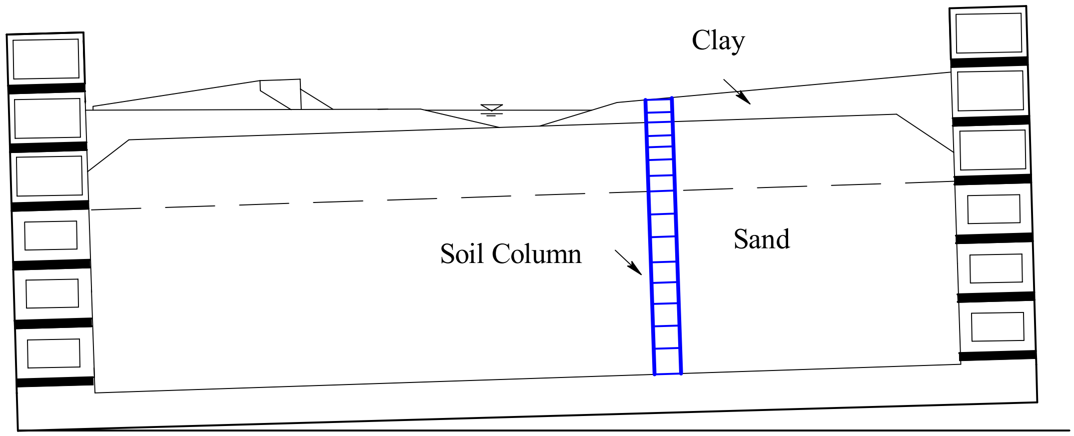

ELEVATION OF THE MIDDLE SECTION

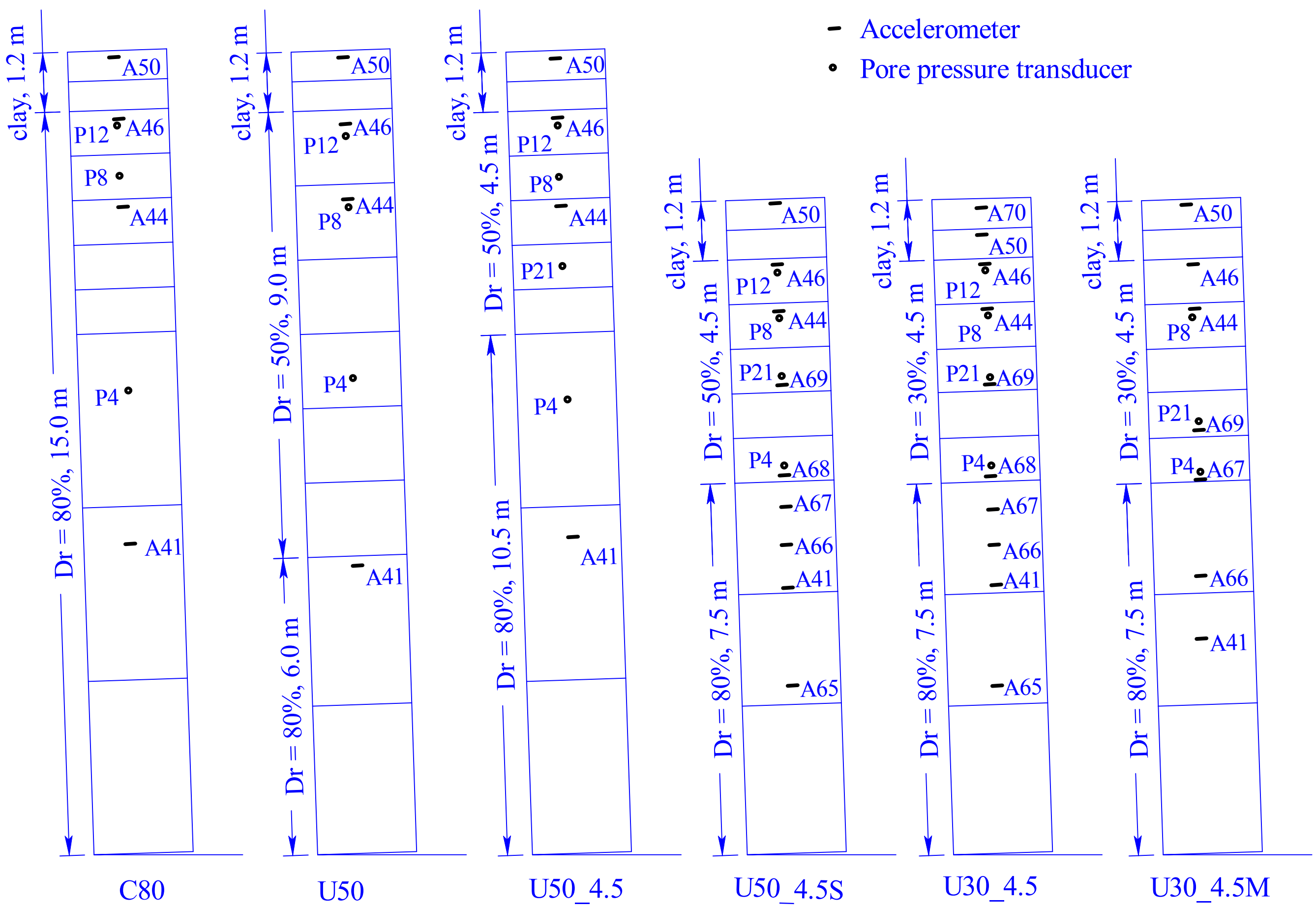

Fig. 4.0.1 Soil elements and sensor locations used in the finite element analyses

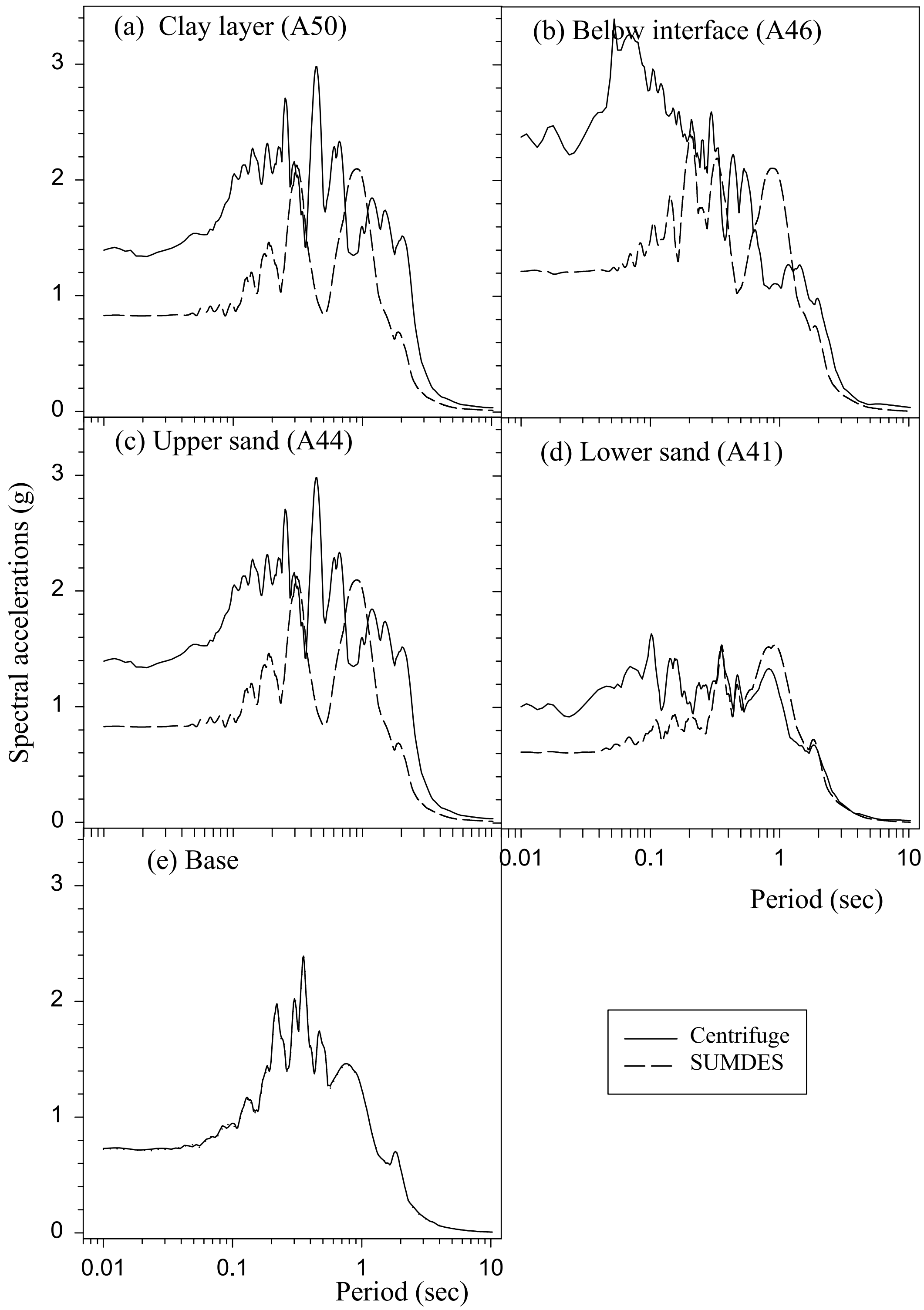

Fig. 4.3.1.1 Measured and calculated (SUMDES) acceleration response spectra for the large Kobe event in C80

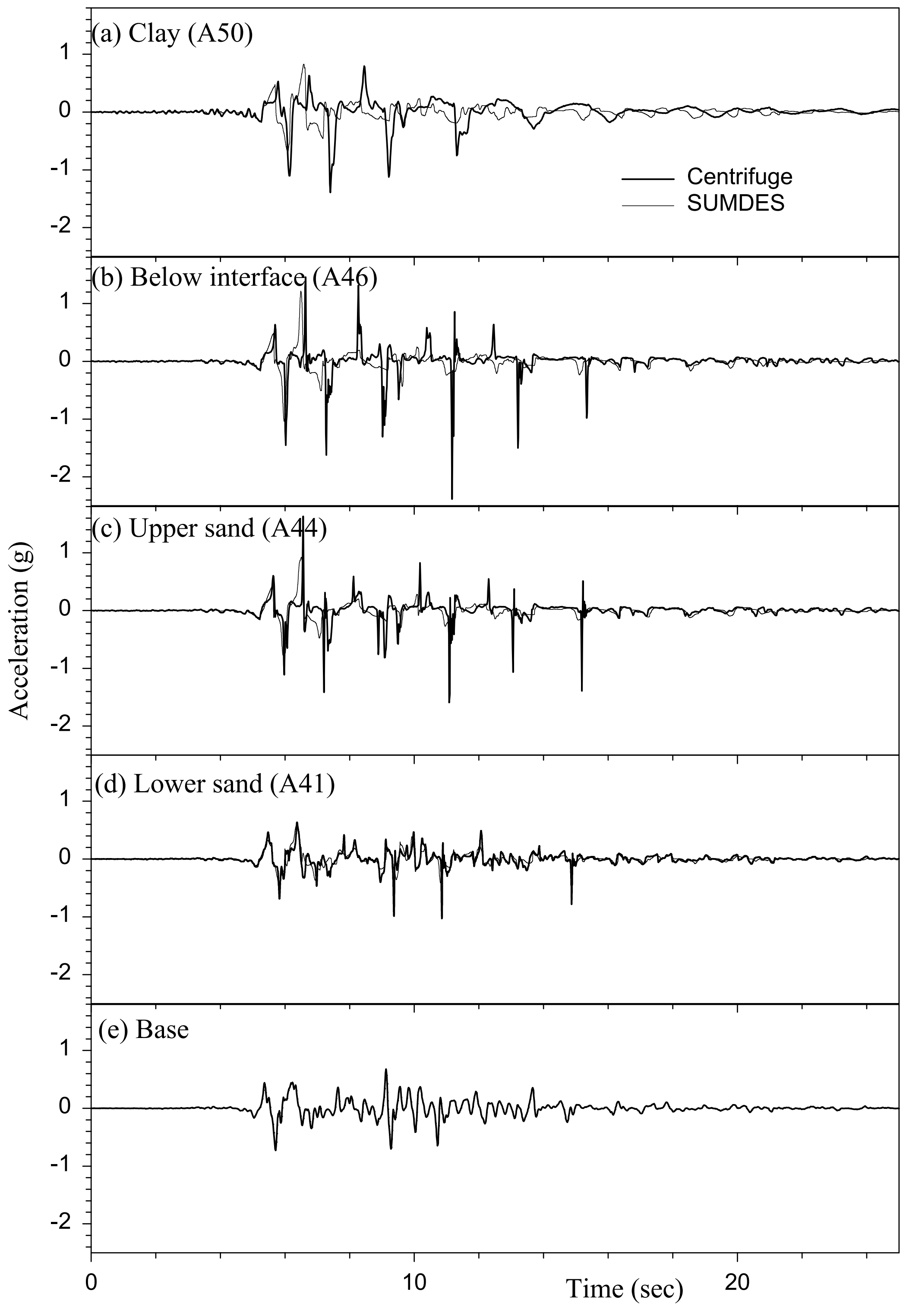

Fig. 4.3.1.2 Measured and calculated (SUMDES) acceleration time histories for the large Kobe event in C80

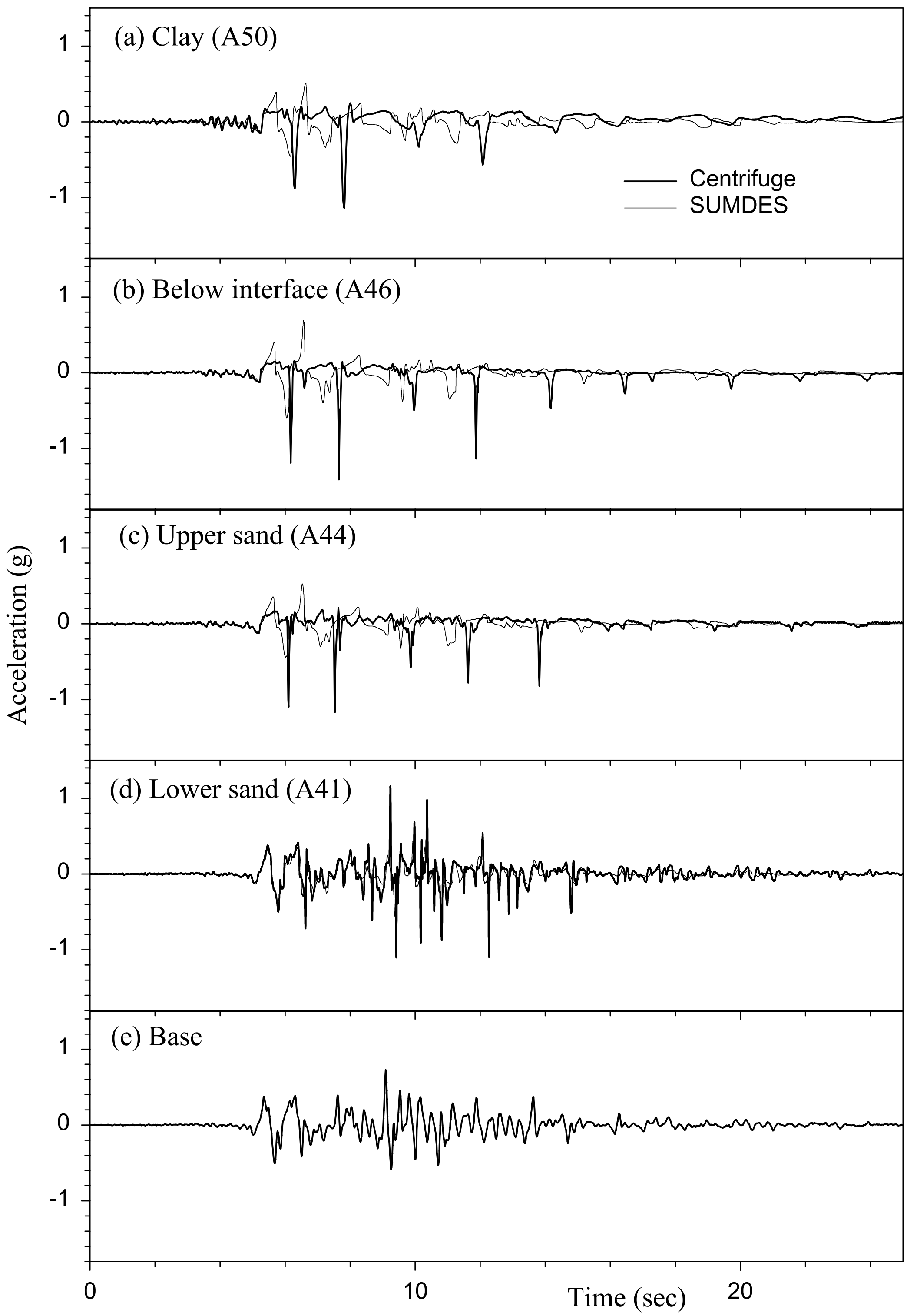

Fig. 4.3.1.3 Measured and calculated (SUMDES) acceleration time histories for the large Kobe event in U50

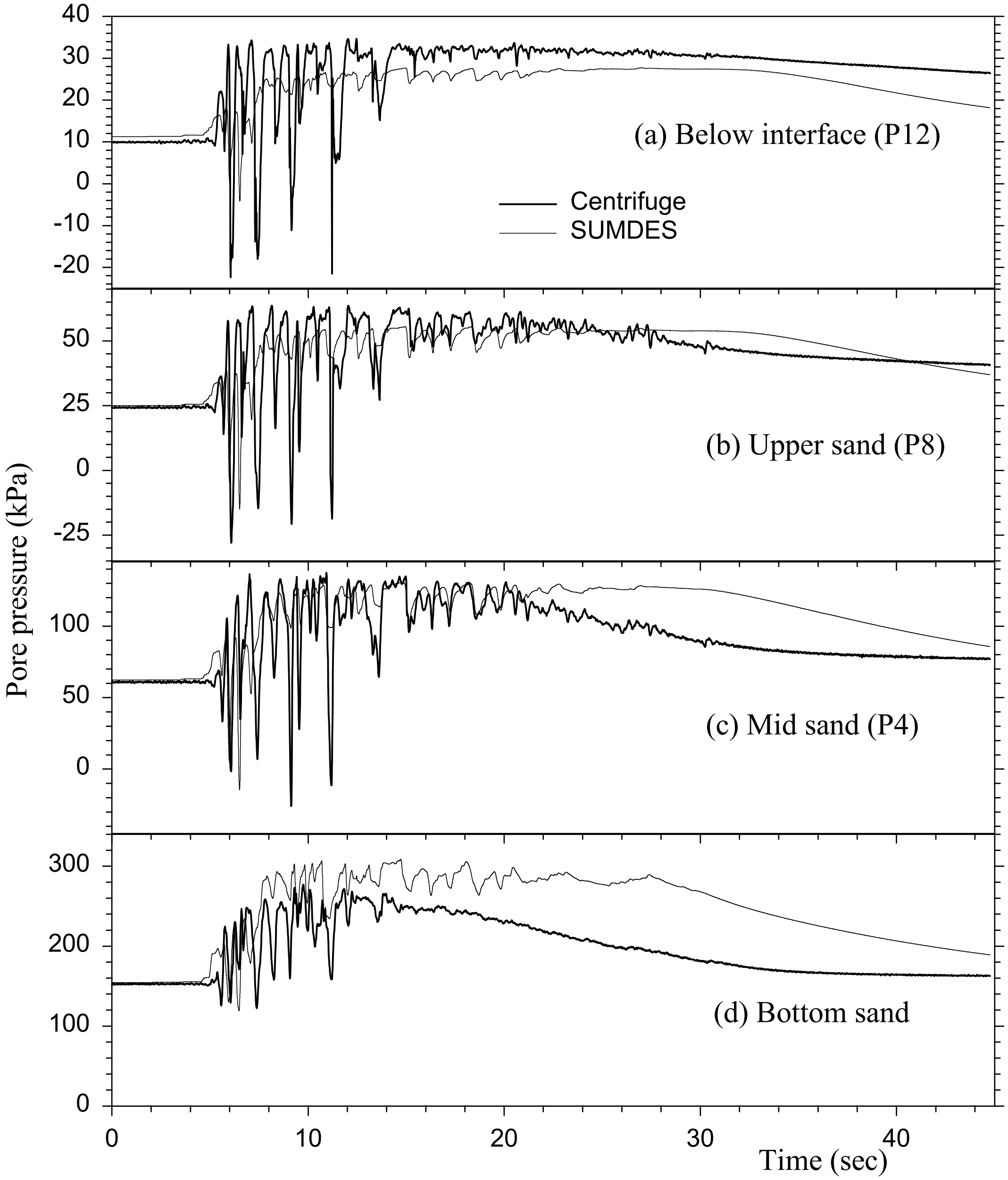

Fig. 4.3.1.4 Measured and calculated (SUMDES) pore pressure time histories for the large Kobe event in C80

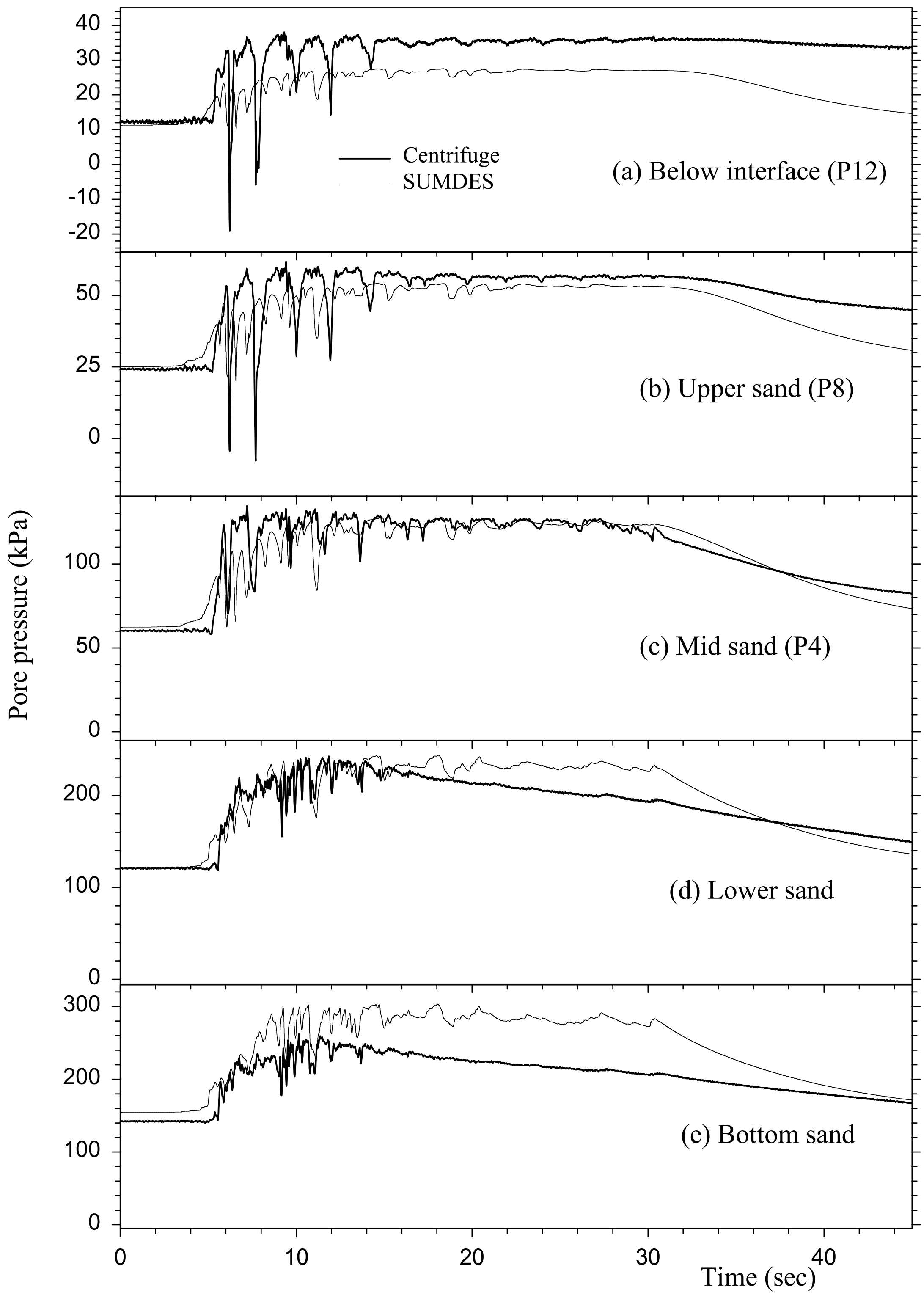

Fig. 4.3.1.5 Measured and calculated (SUMDES) pore pressure time histories for the large Kobe event in U50

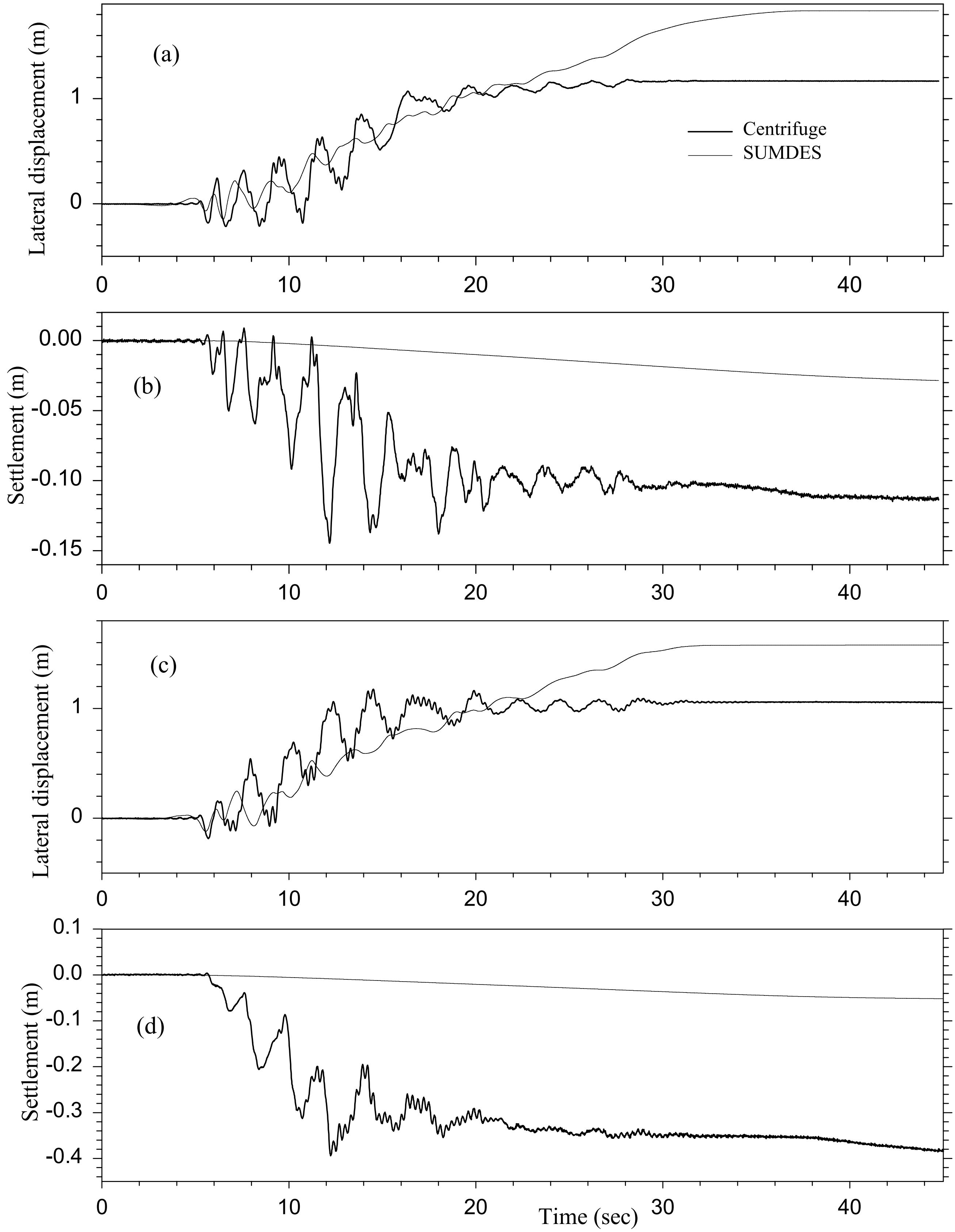

Fig. 4.3.1.6 Measured and calculated (SUMDES) displacement time histories at ground surface for (a), (b) C80 and (c), (d) U50

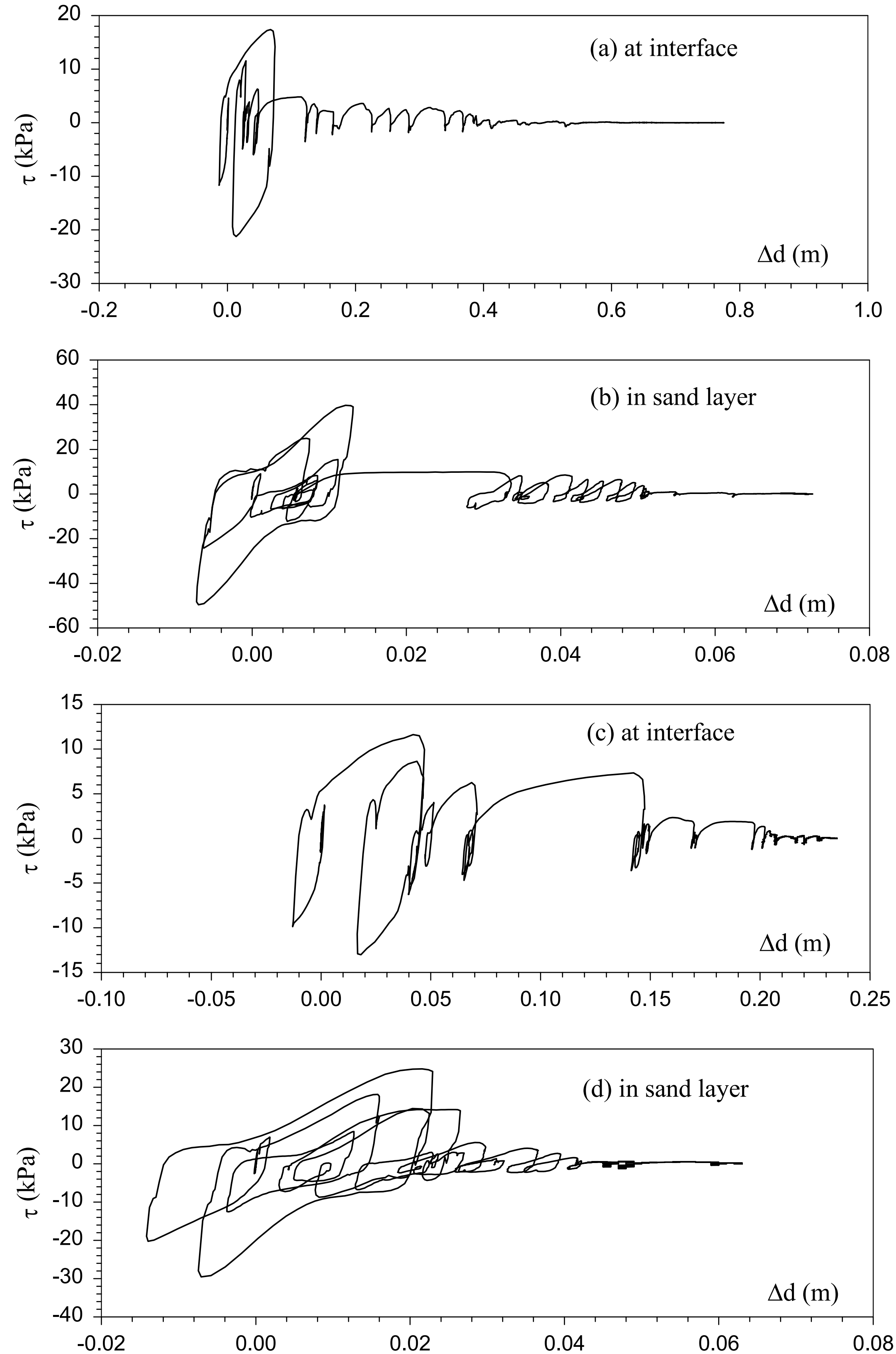

Fig. 4.3.1.7 Shear stress-displacement loops from SUMDES simulation for large Kobe event in (a), (b) C80 and (c), (d) U50

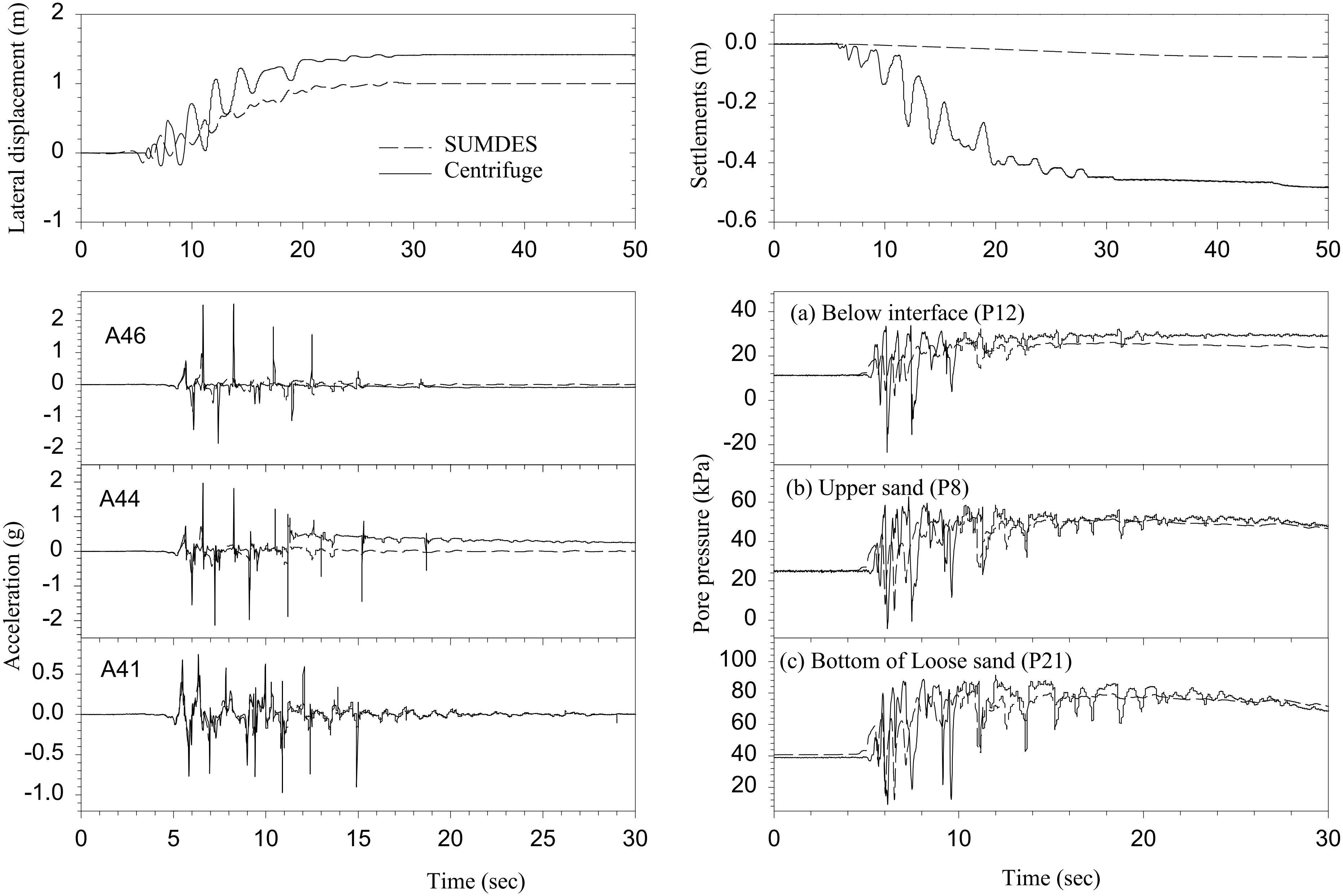

Fig. 4.3.1.8 Comparison of centrifuge results of test U50_4.5 with predictions from SUMDES

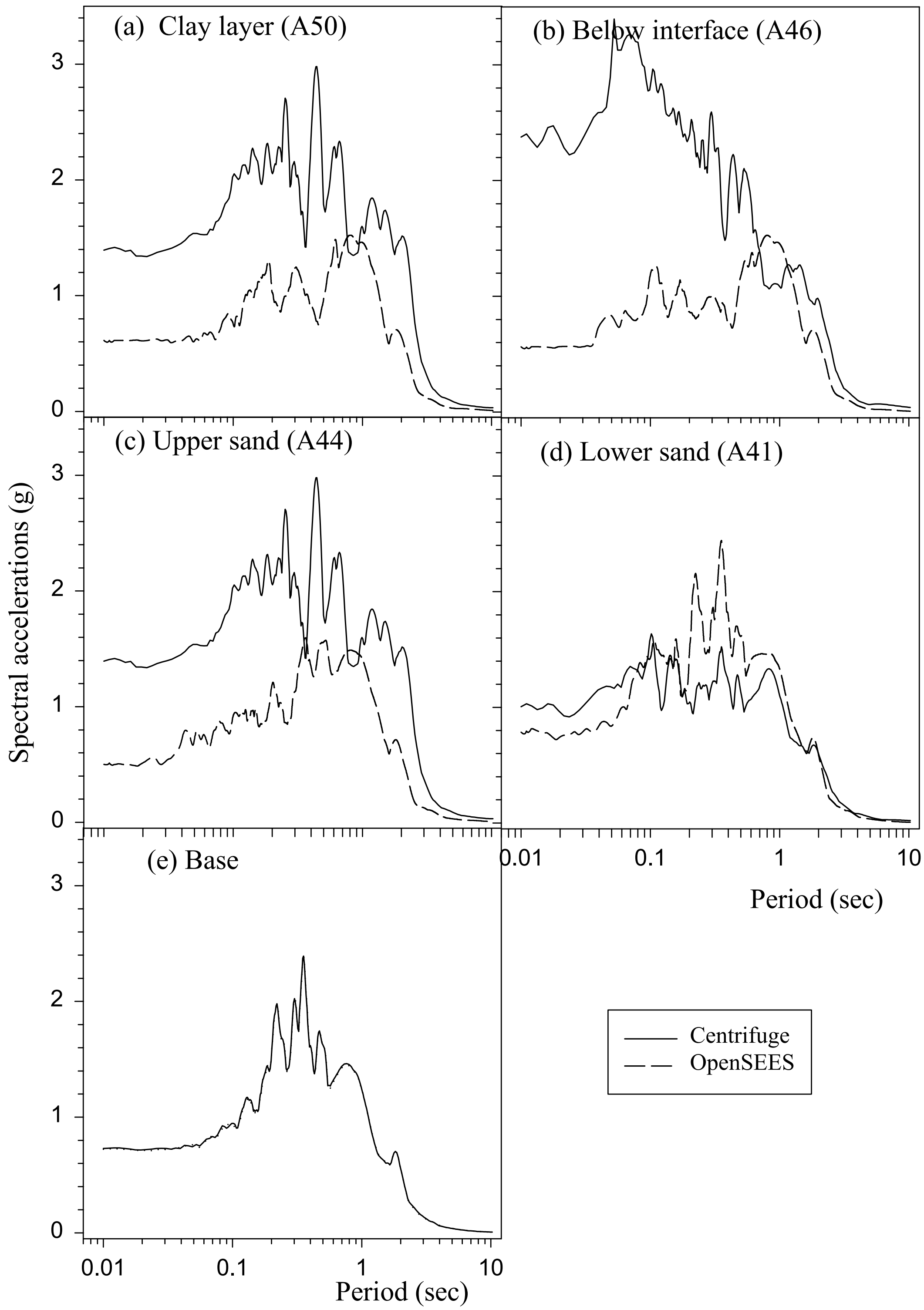

Fig. 4.3.2.1 Measured and calculated (OpenSEES) acceleration response spectra for the large Kobe event in C80

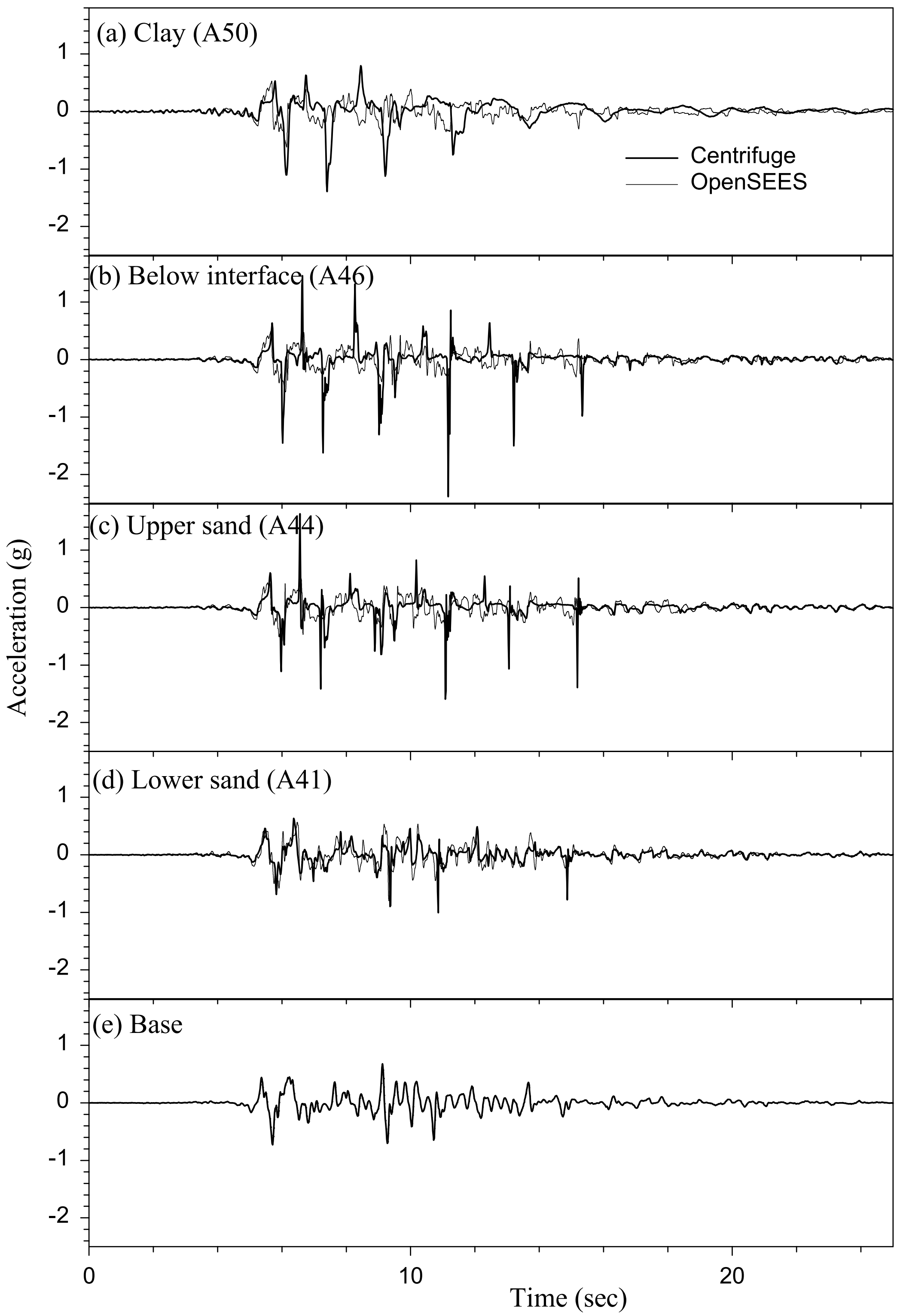

Fig. 4.3.2.2 Measured and calculated (OpenSEES) acceleration time histories for the large Kobe event in C80

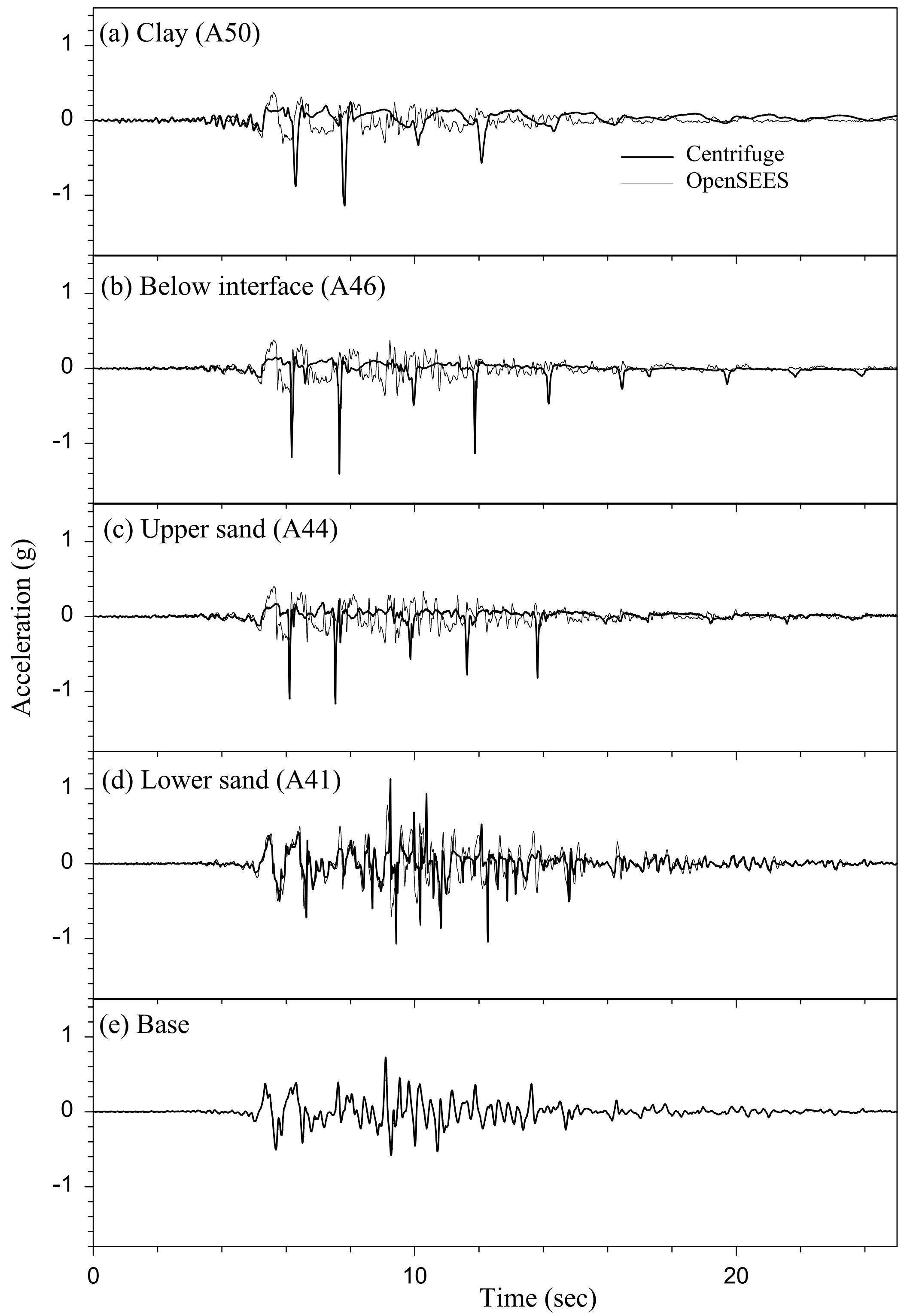

Fig. 4.3.2.3 Measured and calculated (OpenSEES) acceleration time histories for the large Kobe event in U50

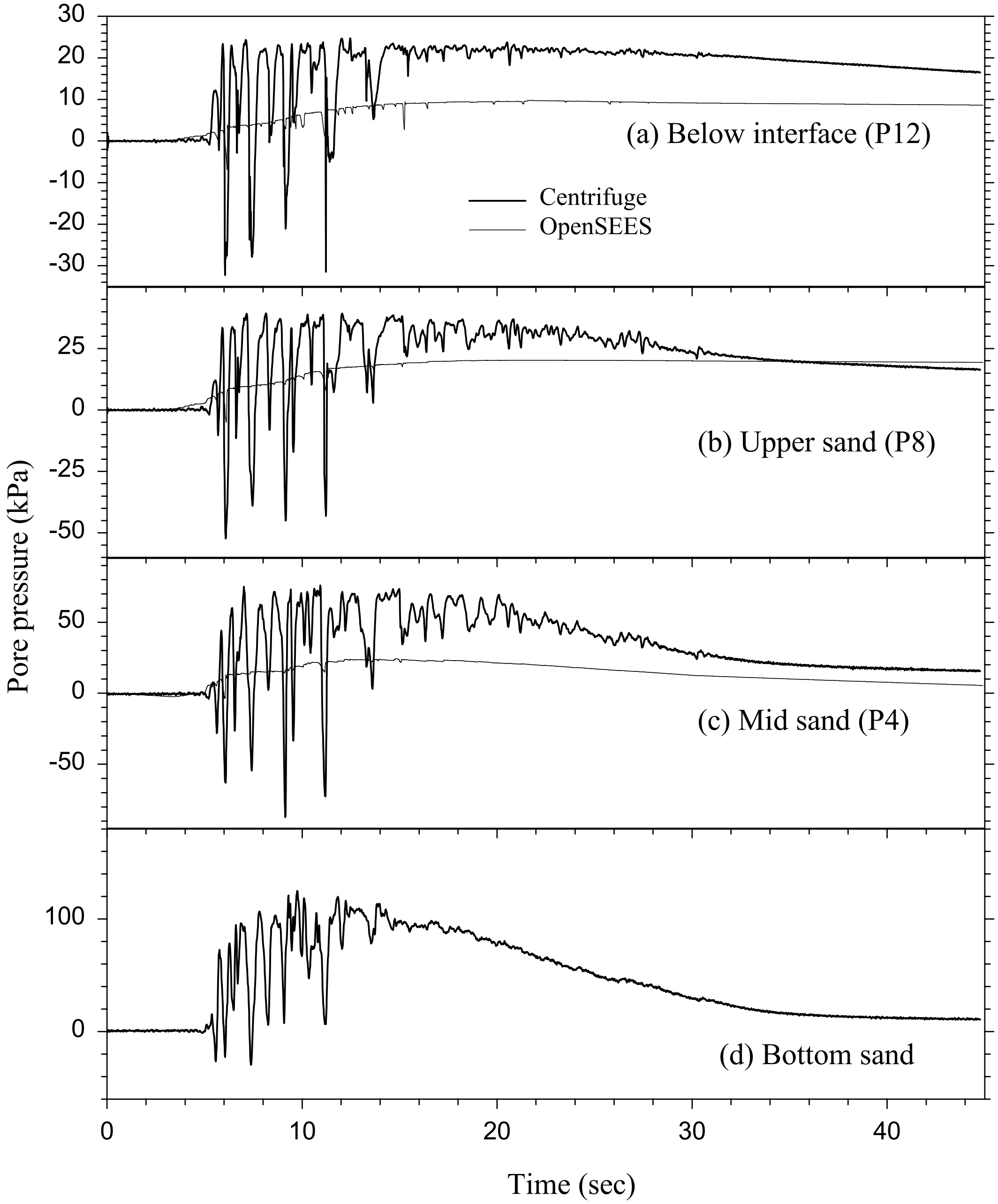

Fig. 4.3.2.4 Measured and calculated (OpenSEES) excess pore pressure time histories for the large Kobe event in C80

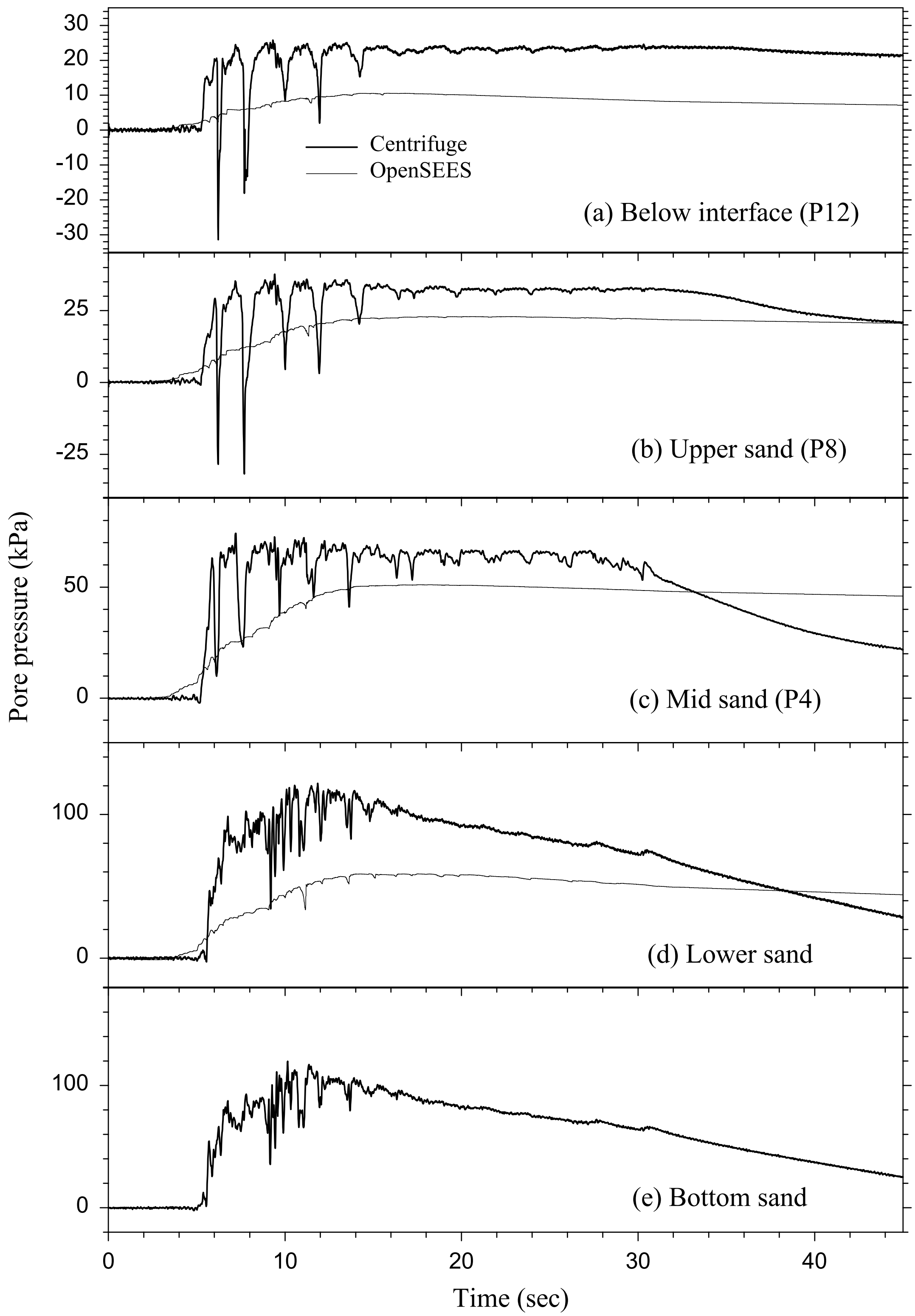

Fig. 4.3.2.5 Measured and calculated (OpenSEES) excess pore pressure time histories for the large Kobe event in U50

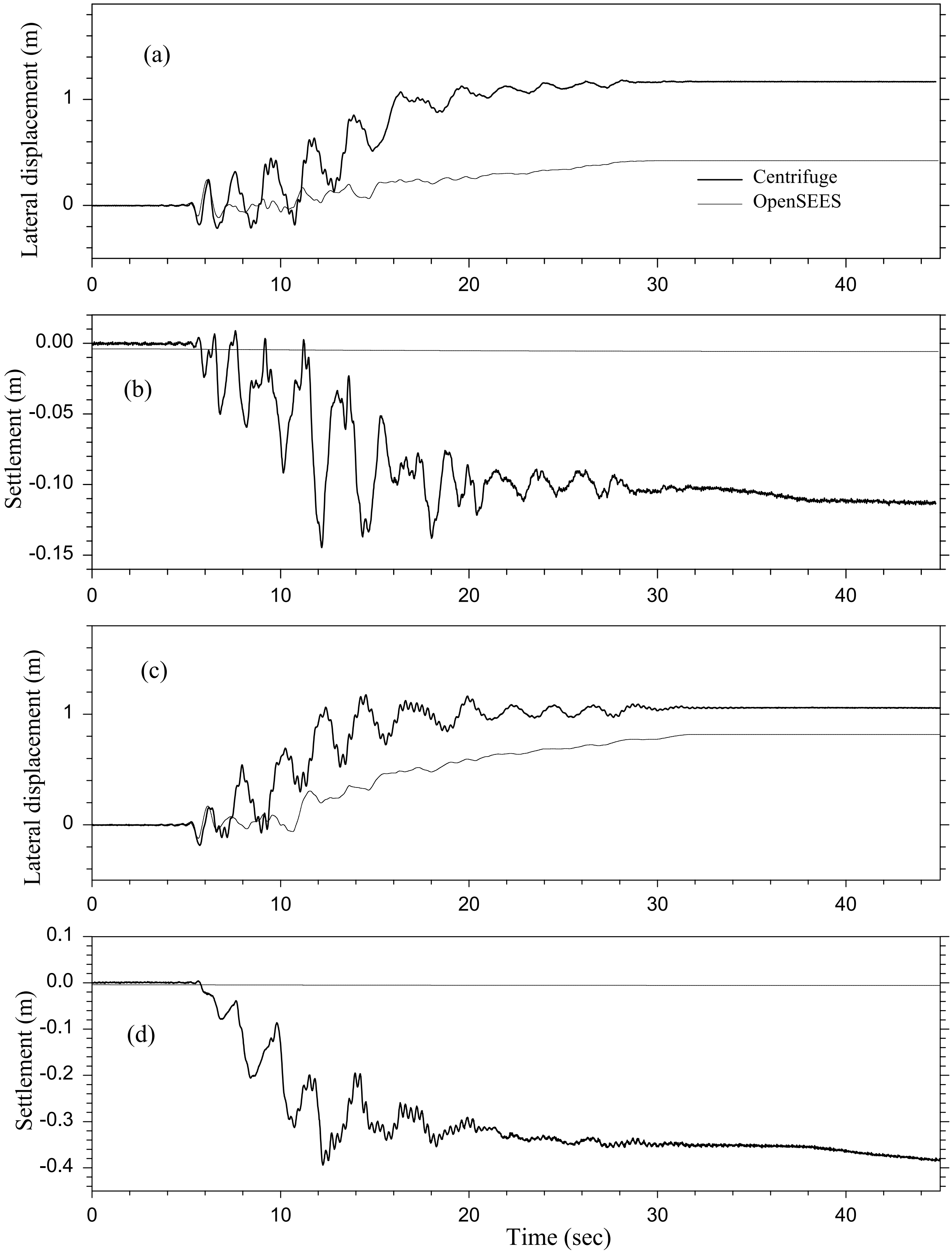

Fig. 4.3.2.6 Measured and calculated (OpenSEES) displacement time histories at ground surface (clay) for (a), (b) C80 and (c), (d) U50

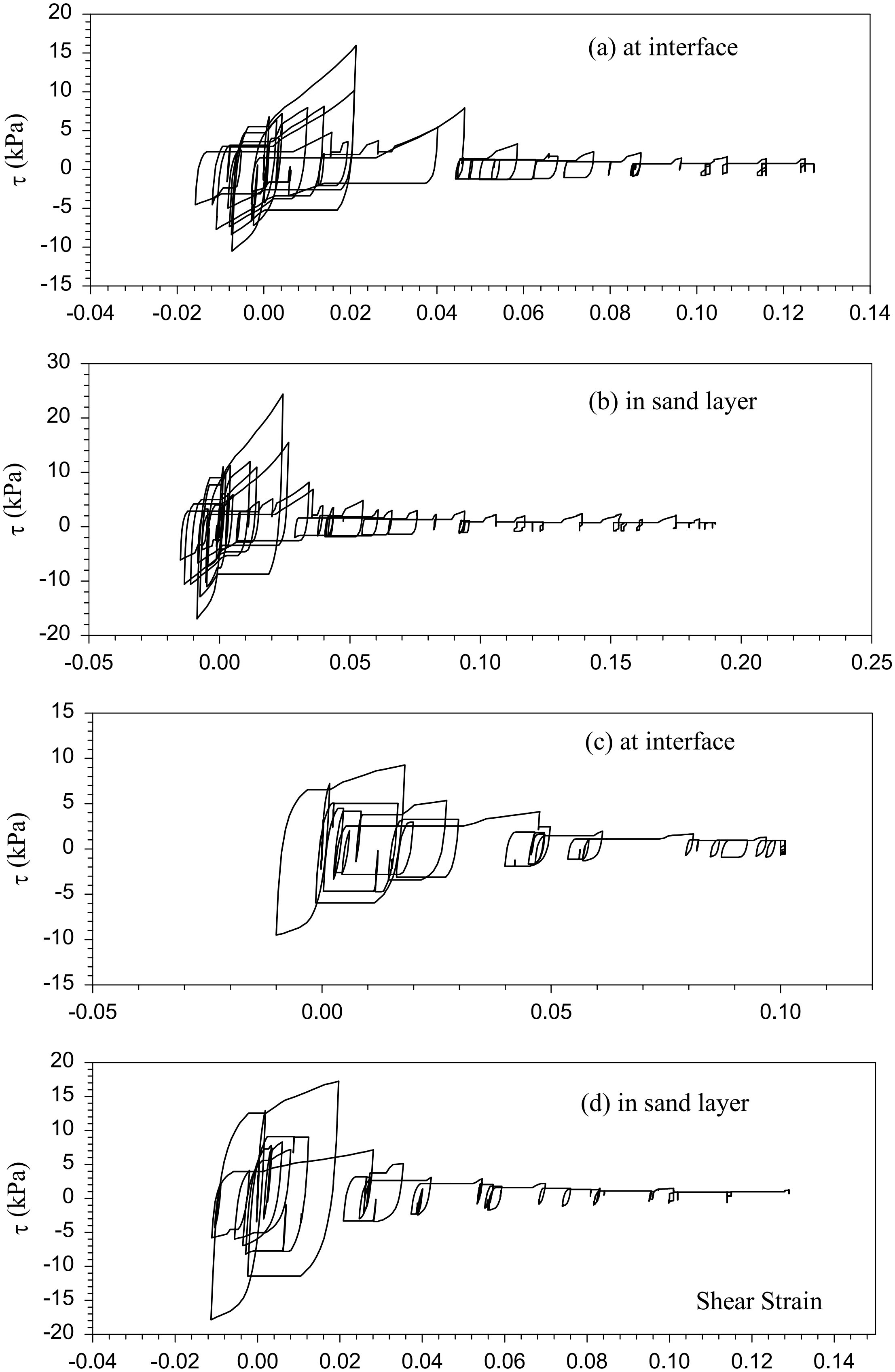

Fig. 4.3.2.7 Shear stress-strain loops from OpenSEES simulation for large Kobe event in (a), (b) C80 and (c), (d) U50

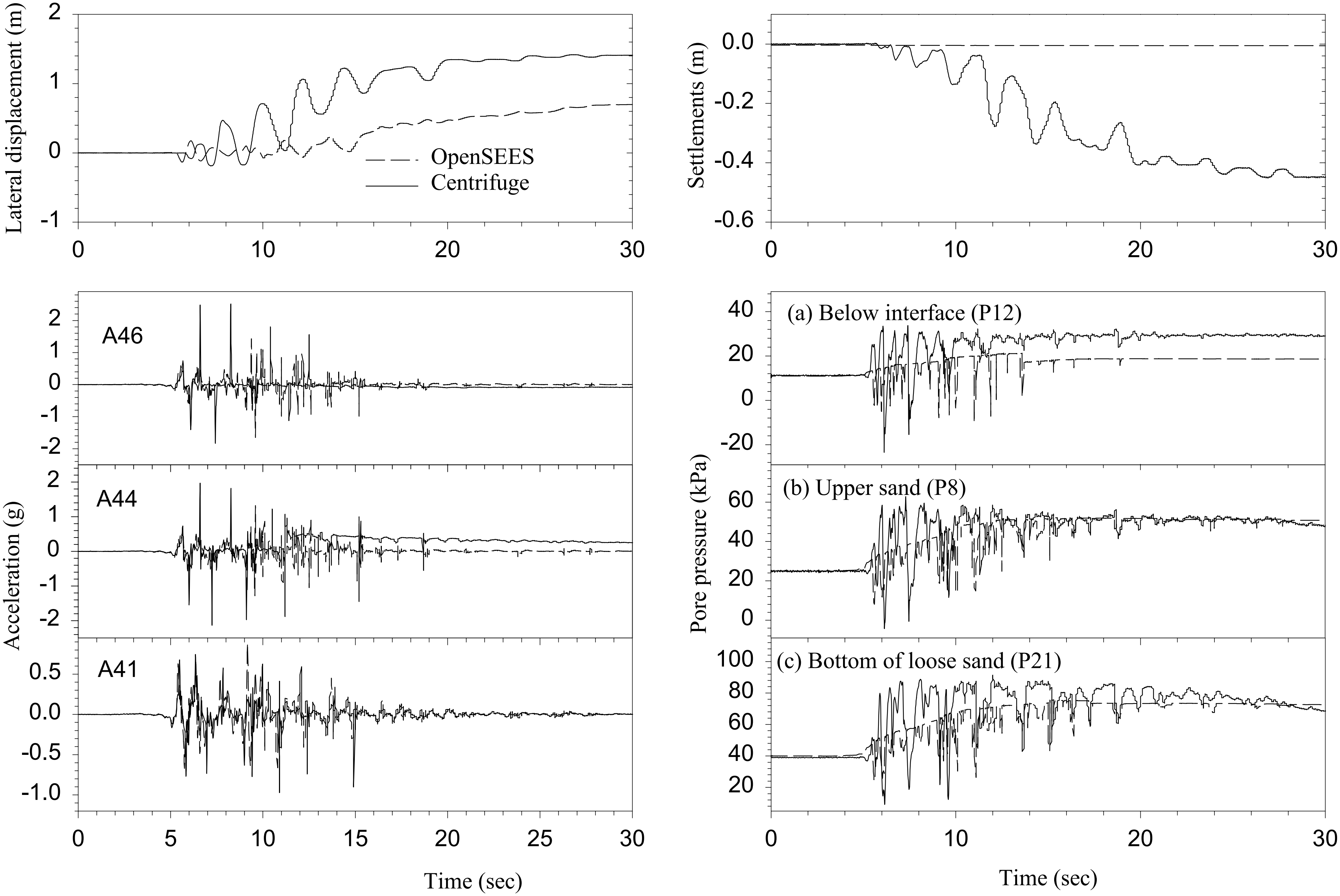

Fig. 4.3.2.8 Comparison of Centrifuge results of test U50_4.5 with predictions from OpenSEES

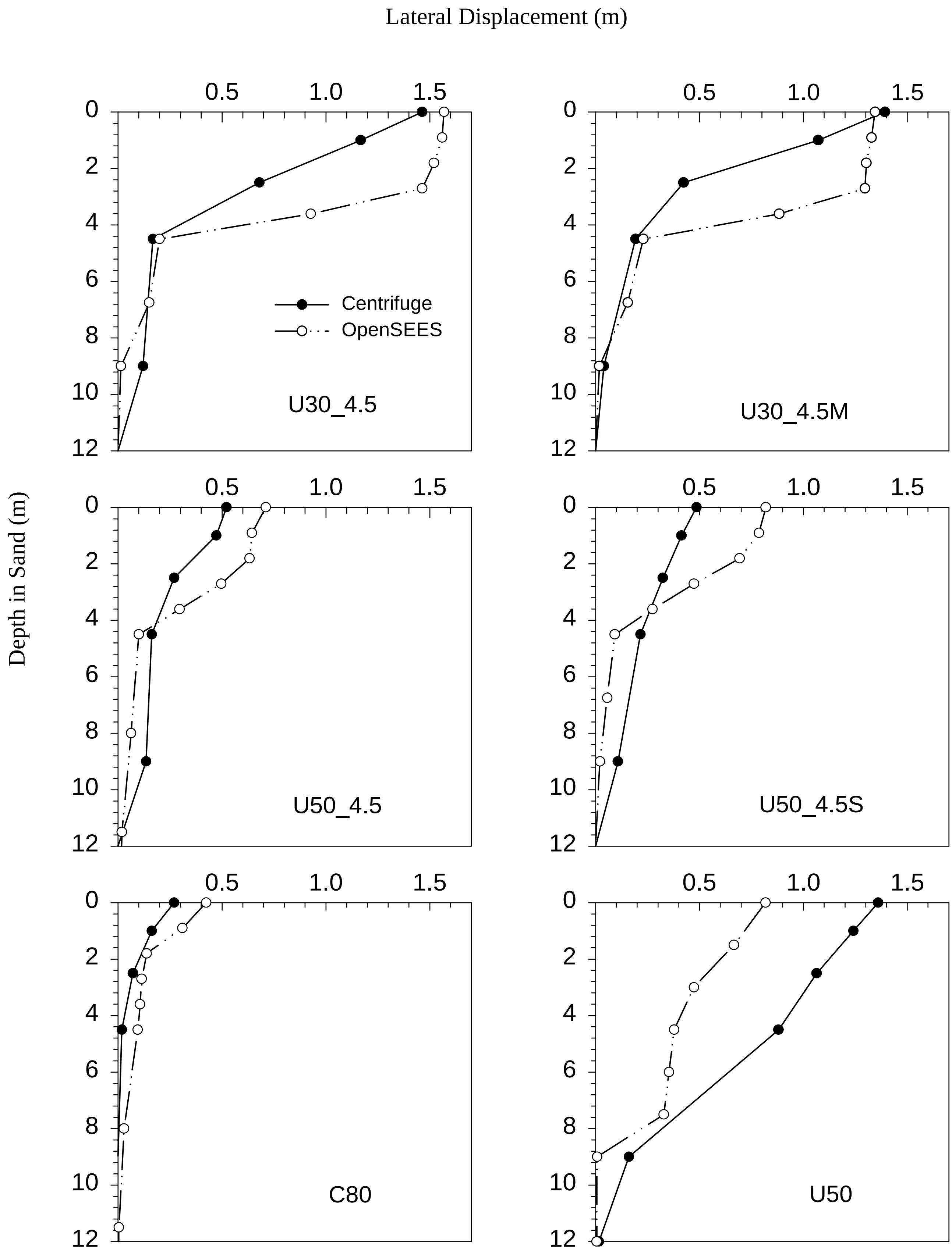

Fig. 4.3.2.9 Experimental and computed (OpenSEES) lateral movements of sand at the south-central portion of the models for large events

5 Summary and Conclusions

This report summarizes the results of six large-scale centrifuge model tests and compares the experimental results with the predictions obtained from the finite element analyses. A hypothetical bridge site consisting of sand layers overlain by a thin clay layer was used as the base model in this study. The clay layer had different slopes on each side with a river channel in the middle and a surcharge load in the form of a bridge abutment on one floodplain. The models were prepared to study the effects of the thickness and density of the soil layers on the amount of settlement and lateral movement of soil during dynamic loadings. Models were prepared with different densities and thickness of sand layers, and were subjected to different scaled versions of the recorded earthquake acceleration time histories. Each of these experiments can be considered to be a well-documented case history. Data reports that include model configurations, applied base motions, and all the sensor recordings are available for download at **http://cgm.engr.ucdavis.edu**. Finite element analyses were carried out for the centrifuge model tests using SUMDES and multi-yield surface models (OpenSEES), and the simulated results were compared with the experimental behavior of soils. The following are the important findings of the experimental and analytical studies.

5.1 TESTING PROCEDURE

All the models were prepared using similar model preparation procedures and tested in the large geotechnical centrifuge at UC Davis. Required relative densities were obtained within a tolerance of 5% using calibrated sand pluviators. The vacuum consolidation method worked well to make an overconsolidated clay layer with different slopes. In order to improve the degree of saturation, the clay layer was consolidated before the saturation of the sand layer. The degree of saturation, estimated based upon the P-wave velocity measurements between two accelerometers placed inside the sand layer indicated that the degree of saturation was above 99% in all the models.

The use of flexible shear beam containers as model containers allowed the soil layers to deform dynamically and reduced the boundary effects on the soil. The dynamic displacements calculated from the recorded accelerations of the soil and the container are similar, indicating that the container performed well. About 70 sensors, including accelerometers, pore pressure transducers, and LVDTs were used to record the electronic data for each of the shaking events. Placement of sensors in similar locations in all the models simplified the comparisons and interpretations of different test results. In addition to the electronic instruments, many black sand columns and spaghetti noodles were installed in the models to study the deformation pattern of the soil layers. The black sand columns enabled the measurements of settlement and lateral movements of soil at different depths within an accuracy of about 1.0 mm (model scale).

Each of these models was subjected to three or four significant shaking events (different scaled versions of Kobe and Santa Cruz motions) at 30 g centrifugal acceleration. Spectral accelerations and displacements of applied base motions (Kobe event) look very similar in all five tests, indicating that the centrifuge tests were repeatable and the input motions were reasonably uniform from the shaking equipment to the base of the model container. The large Kobe motion had a much larger spectral displacement than the large Santa Cruz motion, but the Santa Cruz event had a higher frequency content and a larger peak acceleration.

5.2 EXPERIMENTAL RESULTS

Processing techniques were developed to extract better results from the recorded data using FFT and non-causal filters. The high-frequency displacements calculated from the acceleration data were combined with the low-frequency displacement data obtained from the displacement transducer to produce reliable static and dynamic displacement records. For a given base acceleration, the Santa Cruz motion produced similar settlements due to volumetric strain as the Kobe motion, but produced smaller lateral displacements in the sand layers. Very little settlement and lateral deformation occurred after shaking ceased. More than 80% of the total settlement and lateral movement occurred due to the large Kobe event. The cumulative lateral displacements of a non-liquefying clay "crust" in the south floodplain were observed to depend on the surface slope of the clay crust, but were surprisingly insensitive to the thickness and density of the underlying sand layers. The combined effects of isolation, boundary effects (limited river channel width), and trapping of high pore pressure beneath the impermeable crust could explain why the clay displacement is insensitive to the densities of underlying sand.

The pore pressure records indicate that zero effective stress (liquefaction) was produced in the large, intermediate, and, sometimes, small events. But liquefaction was spatially more pervasive and temporally more persistent for the more intense shaking events. As the degree of improvement (density of the soil profile) increases the soil dilatancy increases, and more acceleration spikes are transmitted to the top of the sand layer associated with the negative pore pressure spikes and pore pressures show early dissipation. A new term "deliquefaction" has been defined by Kutter and Wilson [1999]. The deliquefaction spikes in acceleration and pore pressure records were more pronounced for the Kobe motion than for the Santa Cruz motion, indicating that the deliquefaction phenomena is closely associated with the displacement spectrum of the base motion. The shear stress-displacement loops, calculated using a system identification procedure similar to that of [Elgamal et al., 1995] with modifications show that large shear displacements occurred at low effective stress levels with low soil stiffness. Soil stiffness rapidly increases as the shear displacement increases, indicating the dilative behavior of the sand. Larger shear resistance including many dilative shear stress pulses were seen in dense sand (Dr = 80%) than in intermediately dense sand (Dr = 50%).

5.3 NUMERICAL PROCEDURES AND RESULTS

Two different finite element analyses were carried out using (1) multi-yield models available in OpenSEES and (2) a 1-D effective stress based on the finite element code SUMDES. As part of the present study, the finite element code SUMDES was modified to simulate the lateral deformation problems associated with mildly sloping ground, and the modified code was used in the analysis. In both cases, a 1-D geometry of a section of the model was analyzed. In general, both numerical methods worked reasonably well, with some exceptions.

One exception is in regard to the simulation of pore water flow. For SUMDES, a 1-D code, the permeability of the clay was set equal to the permeability of the underlying sand layer. If this was not done, the calculations would go unstable after water was trapped under the clay. The increased 1-D permeability of the clay was physically "justified" by considering that water could escape laterally to the river channel and vertically through surface cracks in the experiments. This input permeability value had a significant effect on the computed lateral movement and the shear resistant at the clay-sand interface, because in the experiments, the shear resistant of the interface was controlled by the accumulation of water underneath the clay layer.

The other exception is in regard to the simulation of pore pressure dissipation in OpenSEES analyses. Since the version of the OpenSEES finite element formulation used in this analysis was uncoupled (pore pressure dissipation and dynamic response cannot be modeled simultaneously) at the time the work in the report was being conducted, OpenSEES could only perform either fully drained or fully undrained analyses. Thus, OpenSEES could not predict the settlements associated with the drainage following liquefaction. However, the latest version of OpenSEES allows for modeling coupled solid-fluid situations and it would be valuable to reanalyze this data using the coupled solid-fluid formulation.

Though SUMDES is a 1-D code, it is capable of predicting three-dimensional motions and pore water pressure within a soil deposit. SUMDES does use a fully coupled formulation, but settlements computed using SUMDES are much lower than those obtained in the centrifuge experiments. Since the rate of settlement is proportional to the rate of water outflow, the inability of simulating the additional drainage paths such as surface cracks and sand boils in the finite element analysis contributed to the differences between the measured and computed settlements. In order to account for these additional drainage paths and to get the reasonable estimation of settlements, permeability of the soil could, in the future, be specified as a function of pore pressure ratio in the finite element simulation.

OpenSEES is an excellent promising finite element platform, which has the capability to support various constitutive models for three-dimensional finite element analysis. The computed results using the constitutive models available in the OpenSEES finite element simulation for accelerations seem to be in good agreement with the recorded accelerations in the centrifuge experiments. The simulated pore water pressures are a little bit lower than the measured pore water pressures in all the cases. The increase in the water table and the settlement of the sand might be the reasons for the high pore water pressures observed in the centrifuge experiments. The computed (OpenSEES) and measured lateral movements of sand compare reasonably well for all the experiments. However, the computed lateral movements of clay are somewhat lower than the movements observed in the experiments.

The constitutive models used in the analyses include the effects of contractancy and dilatancy on soil stiffness. The shape of the stress-strain curves can have a pronounced effect on site response. The computed stress-strain curves were compared to the results obtained by system identification of the centrifuge test data. While the comparisons are qualitatively good in many respects, there are noticeable discrepancies in the details.

5.4 IMPLICATIONS FOR PERFORMANCE-BASED DESIGN

The results of six tests reported herein present a consistent pattern showing that the effects of liquefaction are sensitive to both the density and thickness of the liquefying sand layers. A new deformation index (DI) seems to account for the combined effects of thickness, depth, and density on liquefaction-induced settlements and lateral movements. Contrary to some common practices, the data indicate that thick layers of medium dense soils may cause more severe liquefaction effects than thin layers of loose soils.

An attempt was made to correlate the deformation index with peak base acceleration and average settlement in one chart. By using this tentative chart, the performance of a site with known value of deformation index can be evaluated for different levels of earthquake demand. Volumetric strain contours plotted in peak base acceleration with initial relative density space were compared with the volumetric strain plots proposed by Tokimatsu and Seed [1997]. For comparably smaller ground motions

(a_{max} < 0.3 g), both findings compare well, but for larger motions, our results show larger settlements than those predicted by Tokimatsu and Seed's correlation.

The same DI was also correlated with lateral movements. Effects of ground slope and shaking intensities were not considered in the correlation with lateral movements. The correlation shows a consistent relationship between lateral movements and deformation index for a particular ground slope and shaking intensity. The empirical procedure proposed by Youd et al. [1999] to estimate the lateral movements considers the thickness of the soil layer but not the combined effect of thickness and the relative density of the soil layers. Youd's correlation considers only the thickness of soil layers that have $(N_{1,60}) < 15$; but our results show that soil layers with $(N_{1,60}) > 15$ can also produce lateral movement, if the thickness of the layers are comparably large.

The correlations between the newly defined deformation index and the measured deformations are empirical and appear to be useful. However, additional studies should be undertaken to determine the applicability of these correlations to a wider range of parameters (soil grain size, permeability, ground slope, and ground motion characteristics).

Continued efforts directed toward the verification of numerical procedures, such as the new constitutive models in OpenSEES, with the centrifuge "case histories" are critical to reliable performance evaluation of liquefiable deposits.

REFERENCES

Arulanandan, K., and Scott. R. F. (1993). "Verification of numerical procedures for the analysis of soil liquefaction problems." *Proc., Intl. Conf. VELACS*, Univ. of California, Davis, Calif., Vol. 1 & 2.

Arulanandan, K., and Sybico, J. Jr. (1992). "Post liquefaction settlement of sand." *Proc. of the Wroth Memorial Symp*., Oxford University, England.

Arulmoli, K., Muraleetharan, K. K., Hossain, M. M., and Fruth, L. S. (1991). "VELACS laboratory testing program." *Preliminary Data Rep. to National Science Foundation*, Earth Technology Corporation, Irvine, Calif.

Balakrishnan, A. (2000). "Liquefaction remediation at a bridge site." Ph.D. thesis, University of California, Davis, Calif.

Balakrishnan, A., and Kutter, B.L. (1999). "Settlement, sliding and liquefaction remediation of layered soil." *J. Geotech. Engrg*., ASCE, 125(11).

Bartlett, S. F., and Youd, T. L. (1992). "Empirical analysis of horizontal ground displacement generated by liquefaction induced lateral spread." *National Center for Earthquake Engineering Research Technical Report*., NCEER-92-0021., 114p.

Chen, Y. R. (1995). "*Behavior of fine sand in triaxial, torsional and rotational shear tests*." Ph.D. thesis, University of California, Davis, Calif.

Dobry, R., Taboada, V., and Liu, L. (1995). "Centrifuge modeling of liquefaction effects during earthquakes." *Proc., 1st Intl. Conf. Earthquake Geotech. Engrg.*, Balkema, Rotterdam, The Netherlands, Vol. 3, 129–1324.

Elgamal, A. W., Zeghal, M., Taboada, B., and Dobry, R. (1996). "Analysis of site liquefaction and lateral spreading using centrifuge testing records." *Soils and Found*., Tokyo, 36(2), 111–121.

Fiegel, G. L., and Kutter, B. L. (1994). "Liquefaction mechanism for layered soils*." J. Geotech. Engrg*., ASCE, 120(4), 737–755

Hermann, L. R., de Natale, J. S., and Dafalias, Y. F. (1993). "Numerical implementation of cohesive soil bounding surface plasticity model (Vol. 1)." Civil Engineering Laboratory, Nevada Construction Battalion Center, Report CR 83.010.

Ishihara, K., and Yoshimine, M. (1992). "Evaluation of settlements in sand deposits following liquefaction during earthquakes." *Soils and Found.*, Tokyo, 32(1), 173–188

Kutter, B. L. (1995). "Recent advances in centrifuge modeling of seismic shaking." *Proc., 3rd Int. Conf. on Recent Advances in Geotech. Earthquake Engrg. and Soil Dyn.*, University of Missouri — Rolla, Mo., Vol. 2, 927–942

Kutter, B. L., and Balakrishnan, A. (1998). "Dynamic model test data from electronics to knowledge." *Proc., Int. Conf. Centrifuge '98*, Balkema, Rotterdam, The Netherlands, Vol. 2.

Kutter, B. L. et al. (1994). "Design of a large earthquake simulator at UC Davis." *Proc., Int. Conf. Centrifuge '94*, Balkema, Rotterdam, The Netherlands, 169–175.

Kutter, B. L., and Wilson, D. W. (1999). "De-liquefaction shock waves." *Proc., Seventh U.S.-Japan Workshop on Earthquake Resistant Design of Lifeline Facilities and Countermeasures Against Soil Liquefaction*. Seattle, Washington., 295–310.

Li, X. S., Wang, X. L., and Shen, C. K. (1992). "SUMDES, a nonlinear procedure for response analysis of horizontally layered sites subjected to multi-directional earthquake shaking." *Report to the Department of Civil Engineering*, University of California, Davis, Calif.

Li, X. S. (1993). "Numerical prediction for Model No. 1." *VELACS, Verification of numerical procedures for the analysis of soil liquefaction problems*, Arulanandan and Scott (eds.), Balkema, Rotterdam, 169–178.

Manda, K. K. (2000). "Effects of layer thickness and density on liquefaction phenomena." M.S. thesis, University of California, Davis.

Manzari, M. T., and Dafalias, Y. F. (1997). "A critical state two-surface plasticity model for sands." *Geotechnique*, Vol. 47, No. 2, 255–272.

Schofield, A. N. (1981). "Dynamic and earthquake centrifuge geotechnical modeling." *Proc., Int. Conf. on Recent Advances in Geotech. Earthquake Engrg. and Soil Dyn.*, University of Missouri—Rolla, Mo., Vol. 3, 1081–1100.

Taboada, V. M., and Dobry, R. (1998). "Centrifuge modeling of earthquake-induced lateral spreading in sand." J. Geotech., ASCE, 124(12), 1195–1206.

Tokimatsu, K., and Seed, H. B. (1987). "Evaluation of settlements in sands due to earthquake shaking." *J. Geotech. Engrg.*, ASCE, 113(8), 861–878.

Wang, Z. L., Dafalias, Y. F., and Shen, C. K. (1990). "Bounding surface hypo plasticity model for sand." *J. of Engineering Mechanics*, ASCE, Vol. 116, No. 5, 983–1001.

Wilson, D. W., Boulanger, R. W., Kutter, B. L., and Abghari, A. (1997). "Aspects of dynamic centrifuge testing of soil-pile-superstructure interaction." *Observation and modeling in numerical analysis and model tests in dynamic soil-structure interaction problems, Spec. Publ. No. 64*, ASCE, Reston, Va., 47–63.

Yang, Z. (2000). "Numerical modeling of earthquake site response including dilation and liquefaction." Ph.D. thesis, Columbia University.

Yang, Z., and Elgamal, A. (2002). "Influence of permeability on liquefaction-induced shear deformation." *J. of Engineering Mechanics*, ASCE, Vol. 128, No. 7, 720–729.

Youd, T. L., and Bartlett, S. F. (1991). "Case histories of lateral spreads from the 1964 Alaska earthquake." *Proc., 3rd Japan-US Workshop on Earthquake Resistance Des. of Lifeline Fac. and Countermeasures for Soil Liquefaction*, National Center for Earthquake Engineering Research, Buffalo, N.Y., 175–189.

Youd, T. L., Hansen, C. M., and Bartlett, S. B. (1999). "Revised MRL equations for predicting lateral spread displacement." *Proc., 7th U.S.-Japan Workshop on Earthquake Resistance Des. of Lifeline Fac. and Countermeasures against Soil Liquefaction*, Seattle, Washington., 99–114.

PEER REPORTS

PEER reports are available from the National Information Service for Earthquake Engineering (NISEE). To order PEER reports, please contact the Pacific Earthquake Engineering Research Center, 1301 South 46th Street, Richmond, California 94804-4698. Tel.: (510) 231-9468; Fax: (510) 231-9461.

PEER 2002/13 *Probabilistic Models and Fragility Estimates for Bridge Components and Systems.* Paolo Gardoni, Armen Der Kiureghian, and Khalid M. Mosalam. June 2002.

PEER 2002/12 *Effects of Fault Dip and Slip Rake on Near-Source Ground Motions: Why Chi-Chi Was a Relatively Mild M7.6 Earthquake.* Brad T. Aagaard, John F. Hall, and Thomas H. Heaton. December 2002.

PEER 2002/11 *Analytical and Experimental Study of Fiber-Reinforced Strip Isolators*. James M. Kelly and Shakhzod M. Takhirov. September 2002.

PEER 2002/10 *Centrifuge Modeling of Settlement and Lateral Spreading with Comparisons ot Numerical Analyses***.** Sivapalan Gajan and Bruce L. Kutter. January 2003.

PEER 2002/09 *Documentation and Analysis of Field Case Histories of Seismic Compression during the 1994 Northridge, California, Earthquake.* Jonathan P. Stewart, Patrick M. Smith, Daniel H. Whang, and Jonathan D. Bray. October 2002.

PEER 2002/08 *Component Testing, Stability Analysis and Characterization of Buckling-Restrained Unbonded Braces™.* Cameron Black, Nicos Makris, and Ian Aiken. September 2002.

PEER 2002/07 *Seismic Performance of Pile-Wharf Connections.* Charles W. Roeder, Robert Graff, Jennifer Soderstrom, and Jun Han Yoo. December 2001.

PEER 2002/06 *The Use of Benefit-Cost Analysis for Evaluation of Performance-Based Earthquake Engineering Decisions*. Richard O. Zerbe and Anthony Falit-Baiamonte. September 2001.

PEER 2002/05 *Guidelines, Specifications, and Seismic Performance Characterization of Nonstructural Building Components and Equipment*. André Filiatrault, Constantin Christopoulos, and Christopher Stearns. September 2001.

PEER 2002/03 *Investigation of Sensitivity of Building Loss Estimates to Major Uncertain Variables for the Van Nuys Testbed.* Keith A. Porter, James L. Beck, and Rustem V. Shaikhutdinov. August 2002.

PEER 2002/02 *The Third U.S.-Japan Workshop on Performance-Based Earthquake Engineering Methodology for Reinforced Concrete Building Structures*. July 2002.

PEER 2002/01 *Nonstructural Loss Estimation: The UC Berkeley Case Study. Mary C. Comerio and John C. Stallmeyer.* December 2001.

PEER 2001/16 *Statistics of SDF-System Estimate of Roof Displacement for Pushover Analysis of Buildings.* Anil K. Chopra, Rakesh K. Goel, and Chatpan Chintanapakdee. December 2001.

PEER 2001/15 *Damage to Bridges during the 2001 Nisqually Earthquake.* R. Tyler Ranf, Marc O. Eberhard, and Michael P. Berry. November 2001.

PEER 2001/14 *Rocking Response of Equipment Anchored to a Base Foundation.* Nicos Makris and Cameron J. Black. September 2001.

PEER 2001/13 *Modeling Soil Liquefaction Hazards for Performance-Based Earthquake Engineering.* Steven L. Kramer and Ahmed-W. Elgamal. February 2001.

PEER 2001/12 *Development of Geotechnical Capabilities in OpenSees.* Boris Jeremic. September 2001.

PEER 2001/11 *Analytical and Experimental Study of Fiber-Reinforced Elastomeric Isolators*. James M. Kelly and Shakhzod M. Takhirov. September 2001.

PEER 2001/10 *Amplification Factors for Spectral Acceleration in Active Regions.* Jonathan P. Stewart, Andrew H. Liu, Yoojoong Choi, and Mehmet B. Baturay. December 2001.

PEER 2001/09 *Ground Motion Evaluation Procedures for Performance-Based Design.* Jonathan P. Stewart, Shyh-Jeng Chiou, Jonathan D. Bray, Robert W. Graves, Paul G. Somerville, and Norman A. Abrahamson. September 2001.

PEER 2001/08 *Experimental and Computational Evaluation of Reinforced Concrete Bridge Beam-Column Connections for Seismic Performance*. Clay J. Naito, Jack P. Moehle, and Khalid M. Mosalam. November 2001.

PEER 2001/07 *The Rocking Spectrum and the Shortcomings of Design Guidelines.* Nicos Makris and Dimitrios Konstantinidis. August 2001.

PEER 2001/06 *Development of an Electrical Substation Equipment Performance Database for Evaluation of Equipment Fragilities*. Thalia Agnanos. April 1999.

PEER 2001/05 *Stiffness Analysis of Fiber-Reinforced Elastomeric Isolators.* Hsiang-Chuan Tsai and James M. Kelly. May 2001.

PEER 2001/04 *Organizational and Societal Considerations for Performance-Based Earthquake Engineering.* Peter J. May. April 2001.

PEER 2001/03 *A Modal Pushover Analysis Procedure to Estimate Seismic Demands for Buildings: Theory and Preliminary Evaluation.* Anil K. Chopra and Rakesh K. Goel. January 2001.

PEER 2001/02 *Seismic Response Analysis of Highway Overcrossings Including Soil-Structure Interaction.* Jian Zhang and Nicos Makris. March 2001.

PEER 2001/01 *Experimental Study of Large Seismic Steel Beam-to-Column Connections.* Egor P. Popov and Shakhzod M. Takhirov. November 2000.

PEER 2000/10 *The Second U.S.-Japan Workshop on Performance-Based Earthquake Engineering Methodology for Reinforced Concrete Building Structures.* March 2000.

PEER 2000/09 *Structural Engineering Reconnaissance of the August 17, 1999 Earthquake: Kocaeli (Izmit), Turkey.* Halil Sezen, Kenneth J. Elwood, Andrew S. Whittaker, Khalid Mosalam, John J. Wallace, and John F. Stanton. December 2000.

PEER 2000/08 *Behavior of Reinforced Concrete Bridge Columns Having Varying Aspect Ratios and Varying Lengths of Confinement.* Anthony J. Calderone, Dawn E. Lehman, and Jack P. Moehle. January 2001.

PEER 2000/07 *Cover-Plate and Flange-Plate Reinforced Steel Moment-Resisting Connections.* Taejin Kim, Andrew S. Whittaker, Amir S. Gilani, Vitelmo V. Bertero, and Shakhzod M. Takhirov. September 2000.

PEER 2000/06 *Seismic Evaluation and Analysis of 230-kV Disconnect Switches.* Amir S. J. Gilani, Andrew S. Whittaker, Gregory L. Fenves, Chun-Hao Chen, Henry Ho, and Eric Fujisaki. July 2000.

PEER 2000/05 *Performance-Based Evaluation of Exterior Reinforced Concrete Building Joints for Seismic Excitation.* Chandra Clyde, Chris P. Pantelides, and Lawrence D. Reaveley. July 2000.

PEER 2000/04 *An Evaluation of Seismic Energy Demand: An Attenuation Approach.* Chung-Che Chou and Chia-Ming Uang. July 1999.

PEER 2000/03 *Framing Earthquake Retrofitting Decisions: The Case of Hillside Homes in Los Angeles.* Detlof von Winterfeldt, Nels Roselund, and Alicia Kitsuse. March 2000.

PEER 2000/02 *U.S.-Japan Workshop on the Effects of Near-Field Earthquake Shaking.* Andrew Whittaker, ed. July 2000.

PEER 2000/01 *Further Studies on Seismic Interaction in Interconnected Electrical Substation Equipment.* Armen Der Kiureghian, Kee-Jeung Hong, and Jerome L. Sackman. November 1999.

PEER 1999/14 *Seismic Evaluation and Retrofit of 230-kV Porcelain Transformer Bushings*. Amir S. Gilani, Andrew S. Whittaker, Gregory L. Fenves, and Eric Fujisaki. December 1999.

PEER 1999/13 *Building Vulnerability Studies: Modeling and Evaluation of Tilt-up and Steel Reinforced Concrete Buildings.* John W. Wallace, Jonathan P. Stewart, and Andrew S. Whittaker, editors. December 1999.

PEER 1999/12 *Rehabilitation of Nonductile RC Frame Building Using Encasement Plates and Energy-Dissipating Devices.* Mehrdad Sasani, Vitelmo V. Bertero, James C. Anderson. December 1999.

PEER 1999/11 *Performance Evaluation Database for Concrete Bridge Components and Systems under Simulated Seismic Loads.* Yael D. Hose and Frieder Seible. November 1999.

PEER 1999/10 *U.S.-Japan Workshop on Performance-Based Earthquake Engineering Methodology for Reinforced Concrete Building Structures.* December 1999.

PEER 1999/09 *Performance Improvement of Long Period Building Structures Subjected to Severe Pulse-Type Ground Motions*. James C. Anderson, Vitelmo V. Bertero, and Raul Bertero. October 1999.

PEER 1999/08 *Envelopes for Seismic Response Vectors.* Charles Menun and Armen Der Kiureghian. July 1999.

PEER 1999/07 *Documentation of Strengths and Weaknesses of Current Computer Analysis Methods for Seismic Performance of Reinforced Concrete Members.* William F. Cofer. November 1999.

PEER 1999/06 *Rocking Response and Overturning of Anchored Equipment under Seismic Excitations.* Nicos Makris and Jian Zhang. November 1999.

PEER 1999/05 *Seismic Evaluation of 550 kV Porcelain Transformer Bushings.* Amir S. Gilani, Andrew S. Whittaker, Gregory L. Fenves, and Eric Fujisaki. October 1999.

PEER 1999/04 *Adoption and Enforcement of Earthquake Risk-Reduction Measures.* Peter J. May, Raymond J. Burby, T. Jens Feeley, and Robert Wood.

PEER 1999/03 *Task 3 Characterization of Site Response General Site Categories*. Adrian Rodriguez-Marek, Jonathan D. Bray, and Norman Abrahamson. February 1999.

PEER 1999/02 *Capacity-Demand-Diagram Methods for Estimating Seismic Deformation of Inelastic Structures: SDF Systems*. Anil K. Chopra and Rakesh Goel. April 1999.

PEER 1999/01 *Interaction in Interconnected Electrical Substation Equipment Subjected to Earthquake Ground Motions.* Armen Der Kiureghian, Jerome L. Sackman, and Kee-Jeung Hong. February 1999.

PEER 1998/08 *Behavior and Failure Analysis of a Multiple-Frame Highway Bridge in the 1994 Northridge Earthquake.* Gregory L. Fenves and Michael Ellery. December 1998.

PEER 1998/07 *Empirical Evaluation of Inertial Soil-Structure Interaction Effects.* Jonathan P. Stewart, Raymond B. Seed, and Gregory L. Fenves. November 1998.

PEER 1998/06 *Effect of Damping Mechanisms on the Response of Seismic Isolated Structures.* Nicos Makris and Shih-Po Chang. November 1998.

PEER 1998/05 *Rocking Response and Overturning of Equipment under Horizontal Pulse-Type Motions.* Nicos Makris and Yiannis Roussos. October 1998.

PEER 1998/04 *Pacific Earthquake Engineering Research Invitational Workshop Proceedings, May 14–15, 1998: Defining the Links between Planning, Policy Analysis, Economics and Earthquake Engineering.* Mary Comerio and Peter Gordon. September 1998.

PEER 1998/03 *Repair/Upgrade Procedures for Welded Beam to Column Connections.* James C. Anderson and Xiaojing Duan. May 1998.

PEER 1998/02 *Seismic Evaluation of 196 kV Porcelain Transformer Bushings.* Amir S. Gilani, Juan W. Chavez, Gregory L. Fenves, and Andrew S. Whittaker. May 1998.

PEER 1998/01 *Seismic Performance of Well-Confined Concrete Bridge Columns.* Dawn E. Lehman and Jack P. Moehle. December 2000.